

# **Coordination Polymers for High Index of Refraction and Ammonia Sensing Applications**

by

**David Guan**

B.Sc., University of British Columbia, 2017

Thesis Submitted in Partial Fulfillment of the  
Requirements for the Degree of  
Master of Science

in the  
Department of Chemistry  
Faculty of Science

**© David Guan 2021**

**SIMON FRASER UNIVERSITY**

**Summer 2021**

Copyright in this work rests with the author. Please ensure that any reproduction or re-use is done in accordance with the relevant national copyright legislation.

## Declaration of Committee

**Name:** David Guan

**Degree:** Master of Science (Chemistry)

**Thesis title:** Coordination Polymers for High Index of Refraction and Ammonia Sensing Applications

**Committee:**

**Chair: Robert A. Britton**  
Professor, Chemistry

**Daniel B. Leznoff**  
Supervisor  
Professor, Chemistry

**Zuo-Guang Ye**  
Committee Member  
Professor, Chemistry

**Gary W. Leach**  
Committee Member  
Associate Professor, Chemistry

**Byron Gates**  
Examiner  
Professor, Chemistry

## Abstract

Coordination polymers, which are solid-state systems with nodes and linkers, have been used to study countless material properties. The modularity in the choosing of components to make coordination polymers and the tunability of the properties of the resulting product from this choice has led to the production of many functional materials as well as studies into structure-property relationships. This thesis focuses on two material properties of the refractive index (CH 2) and luminescence-based sensing of ammonia (CH 3). The refractive index is seldom studied using this platform; through extension of design criteria used to make high index materials to coordination polymers, it was found that high indices (from 1.8-2.25) could be achieved using a sample ligand set. In CH 3, systems of the form  $\text{Ph}_4\text{AsMX}[\text{Au}(\text{CN})_2]_2$  (MX: ZnCl, CdCl, CdBr) and  $\text{Ph}_4\text{AsMX}_2[\text{Au}(\text{CN})_2]$  (MX<sub>2</sub>: ZnBr<sub>2</sub>, ZnI<sub>2</sub>) exhibited strong luminescence response towards ammonia vapours so they were assessed for their sensing capabilities. Unfortunately, the materials are limited in that they only respond to concentrations of ammonia far exceeding biological relevance.

**Keywords:** refractive index; optical materials; coordination polymers; sensors; ammonia sensing; functional material design

## Dedication

*Dedicated to all those that have helped me along the way.*

*More adventures to come.*

## Acknowledgements

There are many individuals I would like to thank in helping me get to the finish line for this degree. I am eternally grateful for the wonderful supporting cast within the Leznoff group. The first person I would like to mention is Dr. John Thompson. Although we spent just a few weeks together, John provided invaluable guidance at the start of this journey in introducing me to the projects on refraction and in helping me get trained in the lab. To Bryton Varju, thanks for training me on the fluorimeter and being a welcoming bench mate in my first year. To Declan McKearney, I thank for helping me understand crystallography and for checking my structures. To Dr. Ryan Roberts, Dr. Wen Zhou and Jefferson Pells, I thank you both for the countless talks we had about science but more importantly about life. To Yumeela Ganga-sah and Dr. Ania Sergeenko, I thank you both for providing emotional support and for editing my documents throughout my studies. In addition, I would like to thank Carson Zellman and Prof. Vance Williams for their support in the work presented in Chapter 2 as well as Fabian Ortiz and Jefferson Pells for Chapter 3. A lot of the work in this thesis required elemental analysis for which I thank Mr. Paul Mulyk and Dr. Wen Zhou for carrying out.

Finally, I would like to thank Prof. Daniel Leznoff and my examining committee, Prof. Gary Leach and Prof. Zuo-Guang Ye for their invaluable support and understanding in helping me get to the end of my studies. Prof. Daniel Leznoff has provided me lots of advice and support in academics but also personally and for that I will be eternally grateful. Finally, my journey through this degree was a little unconventional so I must thank the SFU Chemistry Department for allowing me the flexibility to finish my studies.

# Table of Contents

<b>Dedication of Committee.....</b>	<b>ii</b>
<b>Abstract.....</b>	<b>iii</b>
<b>Dedication .....</b>	<b>iv</b>
<b>Acknowledgements .....</b>	<b>v</b>
<b>Table of Contents .....</b>	<b>vi</b>
<b>List of Tables .....</b>	<b>ix</b>
<b>List of Figures.....</b>	<b>x</b>
<b>List of Acronyms .....</b>	<b>xii</b>
<b><i>Chapter 1 Introduction .....</i></b>	<b><i>1</i></b>
<b>1.1 Coordination Polymers .....</b>	<b>1</b>
1.1.1 Research Objectives.....	3
1.1.2 Refraction and Considerations in the Development of Refractive Coordination Polymers .....	3
1.1.3 Considerations in the Development of Chemical Sensors .....	4
1.1.4 History of Coordination Polymer Sensors .....	9
1.1.5 Harnessing the Power of Auropilicity in Designing Coordination Polymer Sensors ...	11
<b>1.2 Synthetic Techniques .....</b>	<b>14</b>
1.2.1 General Synthetic and Crystallization Methods.....	14
1.2.2 Solvothermal Synthesis and Crystallization .....	17
<b>1.3 Characterization Techniques .....</b>	<b>18</b>
1.3.1 General Characterization Techniques .....	18
1.3.2 Fluorescence Spectroscopy .....	19
1.3.3 Measurement of Refractive Index.....	21
<b><i>Chapter 2 Refractive Coordination Polymers.....</i></b>	<b><i>23</i></b>
<b>2.1 Introduction.....</b>	<b>24</b>
<b>2.2 Design Criteria for High Index Materials .....</b>	<b>30</b>

<b>2.3 The Current Landscape of High Index Materials .....</b>	<b>31</b>
2.3.1 Intrinsic High Refractive Index Polymers .....	31
2.3.2 High Refractive Index Polymer Nanocomposites .....	35
<b>2.4 A Survey Into Tungstates, Molybdates, and Polyoxometallates .....</b>	<b>37</b>
2.4.1 Background and Motivations .....	37
2.4.2 Aqueous Synthesis of Metal Molybdates and Tungstates .....	38
2.4.3 An Attempt to Improve Processability Characteristics of Metal Tungstates and Molybdates Using Organic Linkers .....	39
2.4.4 Incorporation of Large Anionic POM Clusters .....	40
2.4.5 Conclusions .....	42
<b>2.5 Extending Design Criteria to Coordination Polymers .....</b>	<b>43</b>
2.5.1 Selection of Building Blocks .....	44
2.5.2 Structure and Characterization of 1,5-naphthalenedisulfonate CPs.....	45
2.5.3 Structure and Characterization of 5-Mercapto-3-phenyl-1,3,4-thiadiazole-2(3H)-thione CPs .....	47
2.5.4 Structure and Characterization of 1,3,4-Thiadiazole-2,5-dithiol CPs.....	50
2.5.5 Discussion .....	52
2.5.5 Attempts to Make CPs Using Other Building Blocks .....	56
2.5.6 Conclusions .....	57
<b>2.6 A Brief Adventure Into the World of Birefringence.....</b>	<b>59</b>
2.6.1 Background and Motivations .....	59
2.6.2 Synthesis and Characterization of 2,2';6'2'-terpyridine and 2,6-bis(benzimidazol-2- yl)pyridine Compounds and Polymers .....	60
<b>2.7 Experimental .....</b>	<b>67</b>
2.7.1 Synthetic Procedures .....	68
<b><i>Chapter 3 Luminescent Response of Group 12 Dicyanoaurate Coordination Polymers To Ammonia .....</i></b>	<b><i>77</i></b>
<b>3.1 Introduction.....</b>	<b>77</b>
<b>3.2 Group 12 metal dicyanoaurate coordination polymers for sensing of         ammonia.....</b>	<b>79</b>
3.2.1 Synthesis, Structure, and Characterization of Coordination Polymers of the Form Ph <sub>4</sub> AsMX[Au(CN) <sub>2</sub> ] <sub>2</sub> .....	81

3.2.2 Synthesis, Structure, and Characterization of Coordination Polymers of the Form $\text{Ph}_4\text{AsMX}_2[\text{Au}(\text{CN})_2]$ .....	82
3.2.3 Luminescence Analysis of $\text{Ph}_4\text{AsMX}[\text{Au}(\text{CN})_2]_2$ and $\text{Ph}_4\text{AsMX}_2[\text{Au}(\text{CN})_2]$ .....	83
3.2.4 Ammoniation of the Native Materials and Characterization Attempts.....	86
3.2.5 Luminescence Analysis of $\text{Ph}_4\text{AsMX}[\text{Au}(\text{CN})_2]_2$ and $\text{Ph}_4\text{AsMX}_2[\text{Au}(\text{CN})_2]$ Ammoniated Materials.....	87
3.2.6 Quantum Yield Analysis .....	93
3.2.7 Reversibility, Limit of Detection, Thermogravimetric Analysis.....	93
3.2.8 Conclusions and Future Directions.....	99
<b>3.3 Experimental .....</b>	<b>99</b>
3.3.1 Synthetic Procedures .....	100
<b>Chapter 4 Global Conclusions and Future Directions .....</b>	<b>106</b>
<b>References .....</b>	<b>107</b>
<b>Appendix A. Crystallographic Data .....</b>	<b>120</b>
<b>Appendix B1. Selected Bond Lengths and Angles for Family <math>\text{Ph}_4\text{AsMX}[\text{Au}(\text{CN})_2]_2</math> (MX: ZnCl, CdCl, CdBr).....</b>	<b>121</b>
<b>Appendix B2. Selected Bond Lengths and Angles for Family <math>\text{Ph}_4\text{AsMX}_2[\text{Au}(\text{CN})_2]</math> (MX: ZnBr, ZnI).....</b>	<b>123</b>
<b>Appendix B3. Selected Bond Lengths and Angles for 1,5-nda based Refractive Materials .....</b>	<b>124</b>
<b>Appendix B4. Selected Bond Lengths and Angles for bismuthiol II based Refractive Materials .....</b>	<b>125</b>
<b>Appendix B5. Selected Bond Lengths and Angles for bismuthiol I-based Refractive Materials .....</b>	<b>126</b>
<b>Appendix C. High Birefringence Materials .....</b>	<b>127</b>
Attempted Synthesis and Characterization of Halogenated 2,6-bis(benzimidazol-2-yl)pyridine Coordination Polymers.....	127



## List of Tables

Table 2.1. Refractive Indices of Common Media <sup>80</sup> .....	25
Table 2.2. Refractive Indices of Tungstates and Molybdates .....	39
Table 2.3. Refractive Indices of Tungstosilicic & Phosphotungstic Acid POM-systems..	42
Table 2.4. Summary of Empirical and Predicted Indices .....	54
Table 2.5. Crystal Systems.....	60
Table 3.1. Summary of Luminescence Data at 298 K for [Ph <sub>4</sub> As] <sup>+</sup> compounds.....	89
Table 3.2. Summary of Luminescence Data at 298 K for [Ph <sub>4</sub> P] <sup>+</sup> compounds.....	89
Table 3.3. Qualitative Response of [TPA]CdCl[Au(CN) <sub>2</sub> ] <sub>2</sub> and [TPA]ZnBr <sub>2</sub> [Au(CN) <sub>2</sub> ] to Amine Vapours.....	94
Table 3.4. Qualitative Response of [TPA]CdCl[Au(CN) <sub>2</sub> ] <sub>2</sub> and [TPA]ZnBr <sub>2</sub> [Au(CN) <sub>2</sub> ] to Sulfur and Oxygen Donors .....	98

## List of Figures

Figure 1.1. Representation of coordination polymers.....	1
Figure 1.2. Example of 1D, 2D, & 3D coordination polymers .....	3
Figure 1.3. Jablonski diagrams for fluorescence & phosphorescence .....	5
Figure 1.4. Different types of luminescence-based chemical sensors.....	7
Figure 1.5. Response of optoelectronic nose to industrial chemicals .....	9
Figure 1.6. Bonding modes of dicyanoaurate. ....	12
Figure 1.7. Solvent layering crystallization.....	16
Figure 1.8. Vapour diffusion crystallization .....	16
Figure 1.9. Solvothermal reaction profile .....	17
Figure 1.10. Setup to assess limit of detection and reversibility .....	20
Figure 2.1. Refraction of light .....	25
Figure 2.2. Contributions to polarizability .....	26
Figure 2.3. Effect of angle of incidence on refraction and reflection .....	28
Figure 2.4. Polarizability per molar volume cartoon .....	31
Figure 2.5. Indices of polyimides with varying substituents .....	32
Figure 2.6. Coupling of tetravinylgermane and 1,2-ethanedithiol .....	33
Figure 2.7. Polyferrocene HRIPs.....	34
Figure 2.8. Attempted synthesis of metal tungstates and molybdates incorporating organic linkers .....	40
Figure 2.9. Ligand building blocks .....	45
Figure 2.10. Metal node selection.....	45
Figure 2.11. Extended structure of $\text{Na}_2(1,5\text{-nda})\text{H}_2\text{O}$ with 80% probability thermal ellipsoids. ....	46
Figure 2.12. Extended structure of $\text{Pb}(1,5\text{-nda})(\text{H}_2\text{O})_3$ with 80% probability thermal ellipsoids. ....	47
Figure 2.13. Extended structure of $\text{K}(\text{bismuthiol II})\text{H}_2\text{O}$ with 80% probability thermal ellipsoids. ....	48
Figure 2.14. Extended structure of $\text{Zn}(\text{bismuthiol II})_2$ with 80% probability thermal ellipsoids. ....	49
Figure 2.15. Extended structure of $\text{Pb}(\text{bismuthiol II})_2$ with 80% probability thermal ellipsoids. ....	50
Figure 2.16. Extended structure of $\text{K}_2(\text{bismuthiol I})$ with 80% probability thermal ellipsoids. ....	51
Figure 2.17. Extended structure of $\text{Zn}(\text{bismuthiol I}+\text{H})_2$ with 80% probability thermal ellipsoids. ....	52
Figure 2.18. Calibration relating $\alpha/V$ to the refractive index.....	55
Figure 2.19. Molecular structure of $\text{Hg}(\text{terpy})(\text{CN})_2$ and $\text{Hg}(\text{bbp})(\text{CN})_2$ with 50% probability thermal ellipsoids. ....	61

Figure 2.20. View normal to primary crystallographic face of $\text{Hg(terpy)(CN)}_2$ .....	62
Figure 2.21. View normal to the primary crystallographic face (010) of $\text{Hg(bbp)(CN)}_2$ ..	63
Figure 2.22. Extended network of $\text{Pb(terpy)Cl}_2[\text{Hg(CN)}_2]_{0.5}$ and $\text{Pb(terpy)Br}_2[\text{Hg(CN)}_2]_{0.5}$ . .....	64
Figure 2.23. View normal to the primary crystallographic face (101) of $\text{Pb(terpy)Cl}_2[\text{Hg(CN)}_2]_{0.5}$ .....	65
Figure 2.24. View normal to the primary crystallographic face (010) of $\text{Pb(terpy)Br}_2[\text{Hg(CN)}_2]_{0.5}$ . .....	66
Figure 3.1. Reaction scheme of Group 12 metal halides and $\text{Ph}_4\text{As[Au(CN)}_2]$ .....	80
Figure 3.2. Crystal structure of 2-D sheet motif, $\text{Ph}_4\text{As(Ph}_4\text{P)MX[Au(CN)}_2]_2$ .....	82
Figure 3.3. Crystal structure of 1-D chain motif, $\text{Ph}_4\text{As(Ph}_4\text{P)MX}_2[\text{Au(CN)}_2]$ . .....	83
Figure 3.4. Solid-state luminescence spectra of native $\text{Ph}_4\text{AsZnCl[Au(CN)}_2]_2$ and $\text{Ph}_4\text{AsCl}$ excited at 305 and 337 nm. ....	84
Figure 3.5. Solid-state luminescence spectra of native $\text{Ph}_4\text{AsZnBr}_2[\text{Au(CN)}_2]$ and $\text{Ph}_4\text{AsCl}$ excited at 299 and 331 nm. ....	85
Figure 3.6. Luminescence spectra of native $\text{Ph}_4\text{PCdBr[Au(CN)}_2]_2$ and $\text{Ph}_4\text{PBr}$ excited at 271 and 327 nm. ....	86
Figure 3.7. Solid-state luminescence spectra of $\text{Ph}_4\text{AsZnCl[Au(CN)}_2]_2$ post ammonia exposure. ....	90
Figure 3.8. Solid-state luminescence spectra of $\text{Ph}_4\text{AsZnBr}_2[\text{Au(CN)}_2]$ post ammonia exposure. ....	91
Figure 3.9. Solid-state luminescence spectra of $\text{Ph}_4\text{AsCdCl[Au(CN)}_2]_2$ post ammonia exposure. ....	92
Figure 3.10. TGA thermograms of $[\text{Ph}_4\text{As}]\text{CdCl[Au(CN)}_2]_2$ .....	95
Figure 3.11. TGA thermograms of $[\text{Ph}_4\text{As}]\text{ZnBr}_2[\text{Au(CN)}_2]$ . ....	96

## List of Acronyms and Abbreviations

1-D	one-dimensional
2-D	two-dimensional
3-D	three-dimensional
1,5-nda	1,5-napthalenedisulfonate
$\nu_{CN}$	cyanide stretching frequency
ATR	attenuated total reflection
CP	coordination polymer
EM	electromagnetic
FTIR	Fourier-transform infrared
IR	Infrared
POM	polyoxometalate
ppm	Parts per million
US-OSHA	US-Occupational Safety and Health Administration
TGA	Thermogravimetric analysis
TPA	tetraphenylarsonium cation
TPACl	tetraphenylarsonium chloride
TPP	tetraphenylphosphonium cation
TPPBr	tetraphenylphosphonium bromide
RI	refractive index
SC-XRD	single crystal X-ray diffraction
XRD	X-ray diffraction

# Chapter 1

## Introduction

### 1.1 Coordination Polymers

The first use of the term “coordination polymer” is attributed to J.C. Bailar, Jr (1964).<sup>1</sup> In this work, Bailar compared organic polymers with polymeric inorganic compounds and highlighted the requirements for the building and properties of a new species with metal ions and organic ligands. The interest in these materials rapidly increased in the following decades with the number of publications involving coordination polymers peaking in the early 2010s.<sup>2</sup>

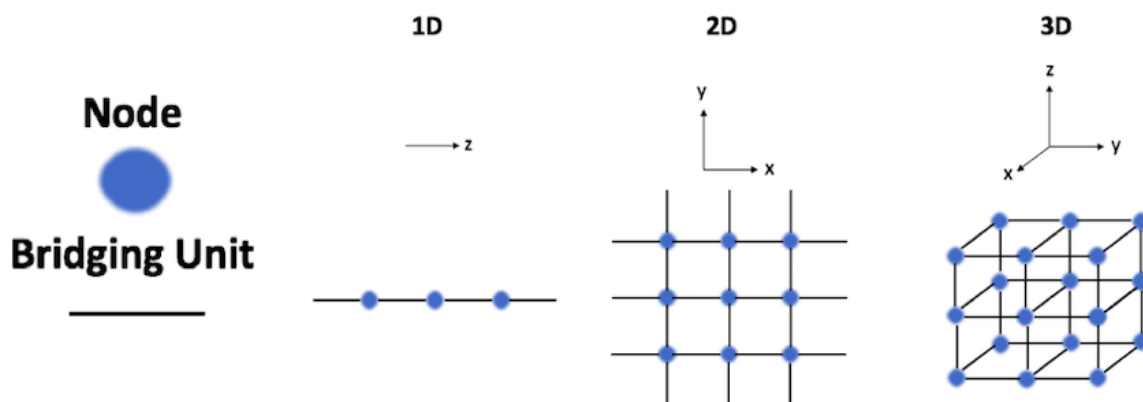


Figure 1.1. Representation of coordination polymers and their different dimensionalities

Coordination polymers (CPs) are inorganic polymeric materials consisting of two building blocks: nodes and linkers.<sup>3,4</sup> Nodes are generally Lewis acidic metal cations or clusters and linkers are the Lewis basic bridging ligands that coordinate to the nodes, creating a polymeric system that can extend in all three dimensions (Figure 1.1.). Representative coordination polymers with various dimensionalities are displayed in Figure 1.2. Coordination polymers are robust and possess many favourable properties, including high thermal stability and resistance toward solvents and aging which make them viable candidates for a plethora of material

property applications.<sup>5</sup> Many synthetic approaches can be taken to modify the resulting structure and dimensionality of the polymer. Firstly, consideration can be given to the type of linker used. In particular, the number of possible binding sites will greatly influence the connectivity in the product. For instance, a linker with two binding sites would be expected to bridge two metal nodes.<sup>6</sup> Terminal/capping ligands can also be used to reduce dimensionality and influence structure.<sup>7</sup> Choosing metal nodes with specific coordination numbers and geometries is another approach but has the caveat that metal coordination environments are often flexible.<sup>8–11</sup> Material functionalities can also be imparted into a coordination polymer through the selection of nodes and linkers that possess the targeted property. Incorporation of linkers that can act as fluorophores or paramagnetic metal nodes can produce polymers that are fluorescent or paramagnetic respectively.<sup>12,13</sup> By using this approach of selecting nodes and linkers towards specific characteristics, catalysis,<sup>14–17</sup> conductivity,<sup>18–20</sup> magnetism,<sup>21–23</sup> and porosity<sup>14,24–26</sup> are amongst some of the properties that have been targeted and studied using CPs.

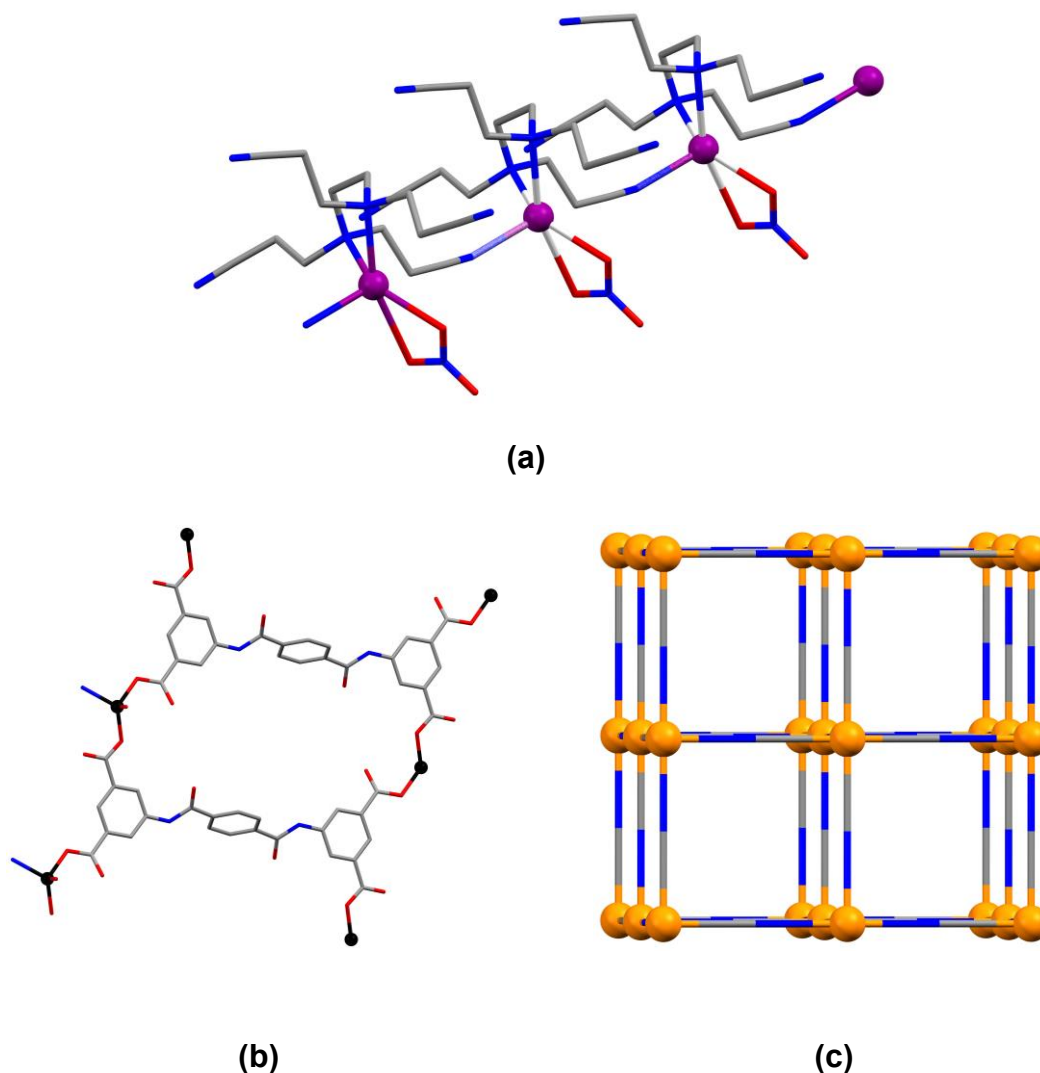


Figure 1.2. Representative examples of 1D (a), 2D (b), and 3D (c) coordination polymers. Nodes are presented as spheres and linkers as rods. Hydrogen atoms removed for clarity. (a) a linear chain of  $\text{Ag}(\text{C}_{14}\text{H}_{20}\text{N}_6)(\text{NO}_3)$ . Ag: purple, C: grey, N: blue, O: red. (b) a 2D grid of  $\text{Zn}_2(\text{bis}-(3,5\text{-dicarboxyphenyl})\text{terephthalamide})(4,4'\text{-bipyridine})$  Zn: black, C: grey, N: blue, O: red. Unbound water and DMF removed for clarity. (c) Prussian blue,  $(\text{Fe}_4[\text{Fe}(\text{CN})_6]_3)^{29,30}$ . Fe: orange, C: grey, N: blue.

### 1.1.1 Research Objectives

The objective of this thesis involves investigating coordination polymers for their potential use in two material applications: high refractive index optical components and luminescence-based sensing of ammonia. The second chapter explores using coordination polymers as a method to make high refractive index materials and the

third probes the intense luminescent response seen in a family of Au(I) containing polymers when exposed to gaseous ammonia.

### **1.1.2 Refraction and Considerations in the Development of Refractive Coordination Polymers**

Refraction is an optical property that involves the bending of light as it passes through interfaces and has implications in the design of devices. The ability of a material to refract light is quantified by the measure referred to as the refractive index.<sup>31</sup> This topic is expanded upon in Chapter 2 but it is established that the most highly refractive materials contain the largest amount of electronic polarizability per unit volume.<sup>31</sup> As such, an experimental study into different ligands and metal nodes with the view of tuning the two factors of polarizability and volume to see the effect on the refractive index of the coordination polymer was carried out. Other considerations that go into making good candidate materials for device fabrications were not considered.

### **1.1.3 Considerations in the Development of Chemical Sensors**

In its simplest definition, a chemical sensor is a material which exhibits a change in some property upon interaction with an analyte of interest. There are countless types of materials with sensing capabilities that have been characterized in the literature. Amongst these are materials that exhibit changes in their electrical properties upon interaction with gaseous species such as  $\text{NH}_3$  and  $\text{NO}_x$ .<sup>32–34</sup> The sensing basis involves modification of the electron and electron hole densities from adsorption and chemisorption interactions at the gas-solid interface. Another type of chemical sensor is luminescence based. Luminescence is a type of cold-body radiation involving the spontaneous emission of light that is not invoked through heating. Luminescent sensors incorporate fluorophores which are compounds that exhibit a fluorescent response. Examples of this type of sensor is a cyclometalated iridium coordination polymer with phosphorescence that is quenched when



exposed to oxygen and a lanthanide metal-organic framework with luminescence sensitive to fluoride and organic small molecules.<sup>35,36</sup>

When electrons in a molecule absorb energy from light, there are a variety of ways that this energy can be dissipated, some of which can result in the emission of light. This is often illustrated using Jablonski diagrams, which are schematics developed by Polish academic Aleksander Jablonski to describe the different phenomena that may occur upon interaction of light with a molecule with respect to electronic energy state transitions (Figure 1.3.).<sup>37</sup>

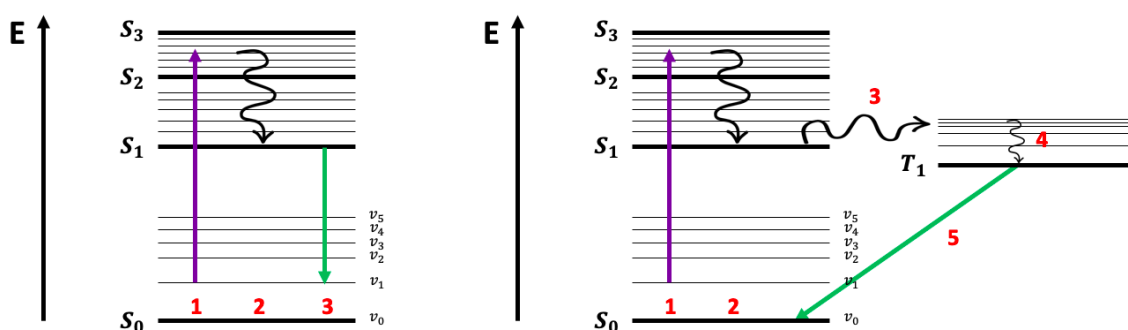


Figure 1.3. (Left) Jablonski diagram illustrating fluorescence and (Right) diagram illustrating phosphorescence.

Relaxation processes can be either *radiative*, resulting in the emission of light, or *non-radiative*, which do not. Curved arrows in Figure 1.3. represent non-radiative processes whereas the solid arrows represent the radiative ones. Fluorescence and phosphorescence are the two types of radiative processes. The difference in electronic energy levels becomes increasingly compressed at higher energies. This is why molecules such as alkanes with high energy absorptions do not typically emit since the similarities in energy between electronic, vibrational, and rotational energy states promotes non-radiative processes. The process begins with absorbance of a photon (Process 1) by the molecule. This absorbance excites an electron from a low energy ground state to a high energy excited state. Only certain wavelengths of light will be absorbed since energy states are quantized. Once in an excited state, there are a multitude of ways for energy to dissipate. One

way is through vibrational relaxation, which involves dropping from one vibrationally excited state of an electronic state to another in the same electronic level. The energy is fed into vibrational or rotational modes of the molecule and lost as kinetic energy. Mechanistically identical to vibrational relaxation is a process called internal conversion (Process 2), which occurs when electrons relax from a vibrational state of one electronic level to that of another electronic level. Once this happens, the electron can further relax to the ground vibrational level of the new electronic state through vibrational relaxation. Vibrational relaxation and internal conversion occur on the order of picoseconds to nanoseconds. However, due to the lack of energy overlap between the ground and first excited state for the electronic energy levels, other radiative processes have an opportunity to occur at the first electronically excited state.

Fluorescence (Process 3: Left) is one such radiative pathway. This involves relaxation of an electron from the vibrational ground state of the first excited state into the electronic ground state. A photon with energy matching this transition is emitted. Emission peaks are often broad because the electron can relax into the various vibrational states of the ground electronic level. The wavelength of light emitted is higher than that observed due to loss of energy to non-radiative processes prior to the fluorescence process. Fluorescence is a slower process occurring on the order of nanoseconds to microseconds but is a spin-allowed transition since the multiplicity is conserved.

Phosphorescence is another radiative pathway through which an excited electron can return to the ground electronic state. Prior to phosphorescence, intersystem crossing (Process 3: Right) occurs, which involves the excited electron changing spin from the excited singlet state to an excited triplet state. This is a very slow process since it violates electronic selection rules but by coupling in vibrational factors becomes weakly allowed and competitive with fluorescence time scales. After intersystem crossing, the electron can undergo vibrational relaxation (Process 4: Right) to the ground vibrational state of the excited triplet electronic state. Finally the radiative phosphorescence process can occur with the electron

relaxing back down to the ground state and emitting a photon of matching energy. This process is very slow, on the order of milliseconds to seconds, because of the violation of spin selection rules. Bold lines denote electronic energy states whereas thin lines represent the vibronic energy states. Vibronic states can be further divided into rotational states but for clarity of presentation, this has been omitted.

Fluorescence usually occurs from the first excited state. If the energy state is too high, this process cannot compete with nonradiative processes. Fluorescence usually occurs on the order of  $10^{-9}$  to  $10^{-6}$  seconds. This is much faster than the other radiative process of phosphorescence which occurs on the order of  $10^{-4}$  to  $10^{-1}$  seconds. Phosphorescence involves a change of electron spin multiplicity from a singlet state to an excited triplet state.

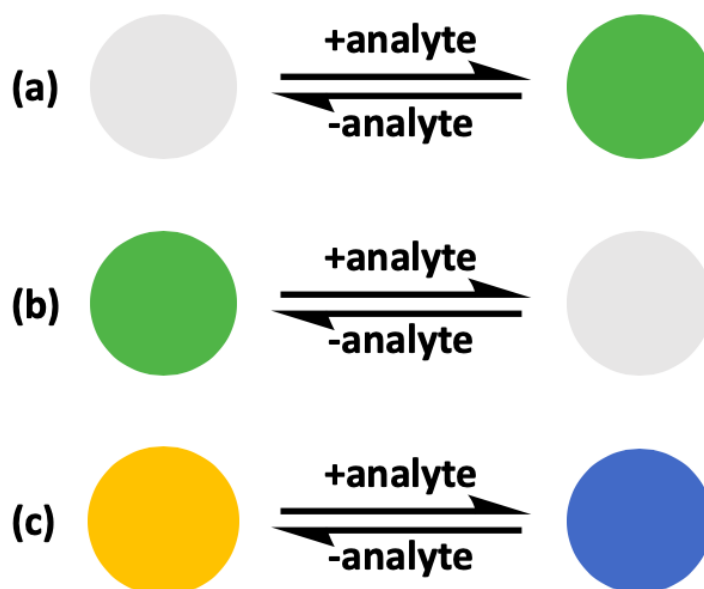


Figure 1.4. Three types of luminescence-based chemical sensors. (a) turn-on, (b) turn-off, and (c) sensor in which the emission profile changes upon exposure to analyte.

The radiative processes of fluorescence and phosphorescence can be used as a basis for sensing. Luminescent chemical sensors fall under three main classifications: turn-on, turn-off, and sensors which change emission profiles (Figure 1.4.).<sup>38,39</sup> As the names suggest, turn-on luminescent sensors are ones in

which a luminescence response is invoked upon exposure to analyte whereas turn-off sensors are ones in which an existing luminescence response is diminished or eliminated.<sup>40,41</sup> Another sensing mechanism involves changes in emission profile of the sensor upon exposure to analyte.<sup>42,43</sup> From a practicality standpoint, the turn-off luminescence sensor would be least desirable as it is the most difficult to discern small changes in output against a strong background.

It is important to consider the sensitivity towards an analyte when designing sensors. Sensitivity is quantified by the limit of detection (LOD) which is the smallest amount of an analyte that can be distinguished from the baseline noise in an analysis technique.<sup>44</sup> Usually, the benchmark to exceed in identifying a significant signal is three times the standard deviation of the noise.<sup>44</sup> The desired LOD would depend on the specific sensing application and would vary based on parameters such as toxicity of the analyte. Selectivity and reversibility are also considerations when designing chemical sensors.<sup>44</sup> Selectivity describes how specific the sensor is towards analytes. Generally, high selectivity is desirable to prevent interfering species from influencing the signal but there are methods to get around it. Optoelectronic noses contain arrays of cross-responsive sensors which as a whole unit has no selectivity to any particular analyte. However, volatile species will interact with the array invoking a characteristic response in each of the individual sensors. A library of “fingerprint” responses for different analytes are collected and from this identification and quantification of an unknown can be done. Suslick et al. demonstrated an array made of dyes printed on polyethylene terephthalate that can differentiate and quantify 19 toxic industrial chemicals (Figure 1.5.).<sup>45</sup>

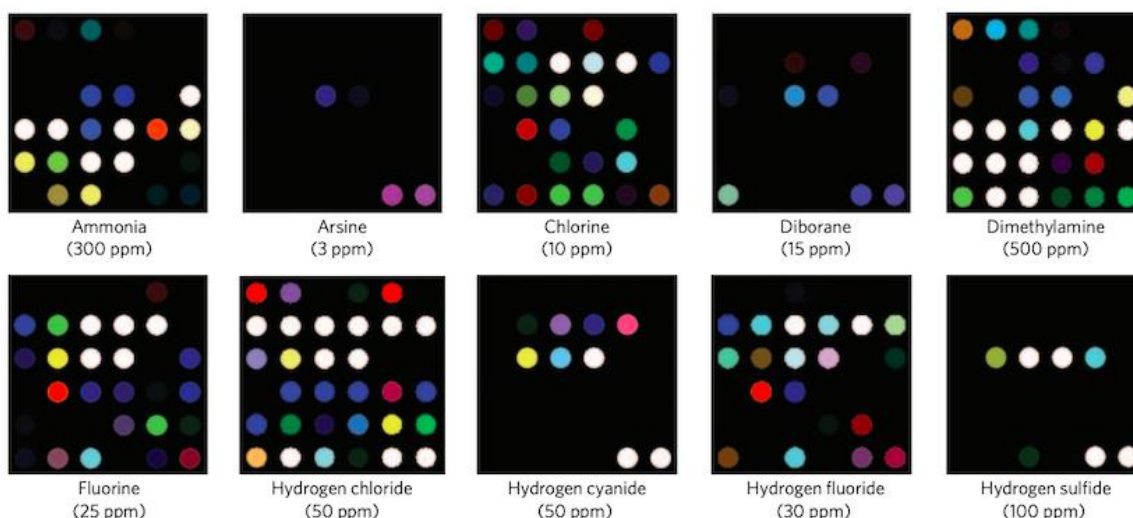


Figure 1.5. Distinct responses towards different toxic industrial chemicals for an optoelectronic nose.<sup>45</sup> Used with permission.

Reversibility describes whether the process that invokes a response from a sensor can be reversed to give the native material allowing it to be used in subsequent sensing events. Heating the exposed material, pumping it down under vacuum, or applying a voltage to it are ways that the analyte can be driven off restoring the native material. An ideal reversible sensor should be able to go through many cycles without degradation in performance. The strength of interaction between the analyte and the proposed sensor should be considered when trying to make it reversible. If the interaction is too strong, it may take too much energy to revert back to the native sensing material whereas if it is too weak, a response might not be invoked. The sensor should be stable under the conditions used to promote the driving off of analyte from the system. Sensors that irreversibly bind their target analyte can also find roles in key applications. An example of this is dosimeters. These devices can irreversibly bind an analyte and the sensor processed and read out after use.

#### 1.1.4 History of Coordination Polymer Sensors

A vast body of work has gone into exploring coordination polymers for their ability to sense chemical analytes. The flexibility seen of the solid-state structure of many

coordination polymers makes them interesting candidates for sensing applications since the interaction between the supramolecular network of the CP and an analyte can result in changes in some assessable metric that would indicate the presence of an analyte.<sup>46,47</sup>

For example, bimetallic systems containing zinc and iridium(ppy)<sub>3</sub> (ppy: 2-phenylpyridine) derivatives have been found to display reversible phosphorescent oxygen sensing capabilities. Cyclometalated complexes such as Ir(ppy)<sub>3</sub> can access facile intersystem crossing which populates the <sup>3</sup>MLCT states leading to phosphorescence which has been harnessed to study light-emitting devices.<sup>48,49</sup> It has been found that this phosphorescence can be quenched by analytes with the triplet ground electronic state so the authors extended its use towards the sensing of gaseous oxygen. This material is an example of a sensing platform that operates in the gaseous state, there are many examples of sensing materials that can detect analytes in the solution state.

In another example, [Zn<sub>2</sub>(L)(bipy)(H<sub>2</sub>O)<sub>2</sub>](H<sub>2</sub>O)<sub>3</sub>(DMF)<sub>2</sub> (H<sub>4</sub>L = bis-(3,5-dicarboxyphenyl)terephthalamide, DMF = N,N'-dimethylmethanamide, bipy = 4,4'-bipyridine) has been demonstrated to be capable of selectively detecting nitrobenzene in the solution state.<sup>50</sup> A redox fluorescence quenching mechanism described by the authors as a donor-acceptor electron-transfer mechanism has been attributed for the sensing behaviour. The emission profile of the CP is predominantly ligand (L<sup>4-</sup>) based with the electronic states being highly localized. The aromatic rings of the L<sup>4-</sup> ligand contain the electron withdrawing groups of carboxyls and amidos which are weaker than that of the nitro group of nitrobenzene resulting in an enhanced energy of the LUMO of the CP compared to the analyte. The excited electrons of the CP transfer to the LUMO of nitrobenzene instead of the ligand-based counterpart leading to a quenching of the emission. The authors describe this sensor material as being selective towards nitrobenzene but did not screen against other benzene derivatives containing electron withdrawing groups such as benzenesulfonic acid.

These examples of coordination polymers involve assessing a change in emissive behaviour to quantify the presence of an analyte. However, there are other parameters to consider such as color in colorimetric sensors. One interesting example of this involves the material  $[\text{Fe}(\text{4-(2'-hydroxyethyl)-1,2,4-triazole})_3]_2 \cdot (\text{H}_2\text{O})$  which is sensitive to contact pressures and displays a persistent color change.<sup>51</sup>  $\text{Cu}[\text{AuX}_2(\text{CN})_2]_2$  ( $\text{X} = \text{Cl}, \text{Br}$ ) displays characteristic Raman  $\nu_{\text{CN}}$  stretches, allowing for identification, when exposed to a group of volatile organic compounds.<sup>52</sup> Changes in conductivity upon exposure to an analyte is also indicative of a sensing event.<sup>53–55</sup>  $[\text{Cd}(\text{H}_2\text{L})_2] \cdot 3\text{H}_2\text{O} \cdot 3\text{DMF}$  where L is an electroactive anthracene based ligand has shown selective chemiresistive sensing behaviour towards volatile amines.<sup>56</sup>

The following section will discuss the sensing properties of dicyanoaurate,  $[\text{Au}(\text{CN})_2]^-$ , containing coordination polymers and in particular how a property specific to gold(I) called aurophilicity can be harnessed as a sensing platform.

### **1.1.5 Harnessing the Power of Aurophilicity in Designing Coordination Polymer Sensors**

Gold(I) dicyanoaurate,  $[\text{Au}(\text{CN})_2]^-$ , can adopt a variety of different bonding modes in coordination polymers (Figure 1.6.).

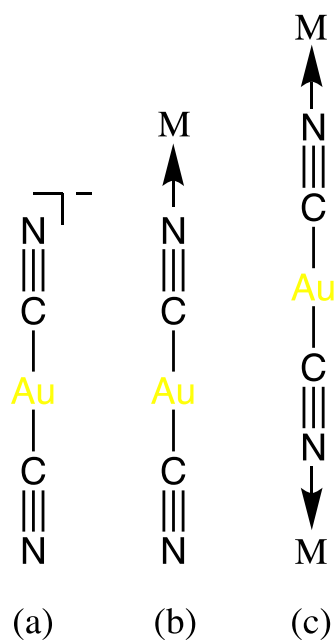


Figure 1.6. Different bonding modes of dicyanoaurate in coordination polymers: (a) as a free anion, (b) monodentate terminal, (c) bridging mode between two metal nodes.

Au(I)-containing materials can exhibit a property called *aurophilicity* which describes an attractive interaction between Au(I) atoms.<sup>57–59</sup> This interaction is a type of  $d^{10}$  closed shell interaction and has been observed in other closed shell ( $d^{10}$ ) systems and is more commonly referred to as *metallophilic* interactions. One of the first observations for gold-gold interactions was in  $\text{Au}(\text{DMG})_2^+ \text{AuCl}_2^-$  (HDMG = dimethylglyoxime) where the Au-Au contacts were 3.26 Å. However, this system involves Au(I) and Au(III)-containing cations and anions meaning the attractive interaction is at least partially Coulombic in nature.<sup>60</sup> One of the first systems that showed gold-gold interactions not assisted by Coulombic interactions was  $\text{Cl}_3\text{PAuCl}$ .<sup>61</sup> Interest in the study of *aurophilicity* grew as computers that revolutionized the modeling of X-ray diffraction data became more accessible and powerful.<sup>62</sup>

The observation that closed shell metal ions with the same charge form attractive interactions was immediately viewed as counterintuitive and spurred a debate in the literature. One of the first rationales for this attractive interaction involved the



suggestion that interactions between closed-shell metals arise due to hybridization between the filled  $nd$  and empty  $(n+1)s$  and  $(n+1)p$  orbitals.<sup>63,64</sup> This view was contradicted by studies which predicted no attractive force between closed shell metals at the Hartree-Fock level but did predict an attraction at the Møller-Plesset level.<sup>65,66</sup> In summary, these studies concluded that aurophilic interactions are caused by correlation effects and strengthened by relativistic effects. The most accepted view today is that London dispersion forces are the main driver behind the formation of these contacts.<sup>58,67</sup>

The attractive interaction can also be rationalized using a simplified molecular orbital approach. This interaction can be modeled as the case of two Au(I) atoms with the  $z$ -axis defined as the internuclear axis between the atoms. The filled  $5d_{z^2}$  atomic orbitals split in energy generating higher energy  $\sigma^*$  and lower energy  $\sigma$  molecular orbitals respectively with the former being the HOMO. The empty  $6p_z$  atomic orbitals also experience splitting into a higher energy  $\sigma^*$  and lower energy  $\sigma$  molecular orbitals respectively with the latter being the LUMO. As such, the bond order is zero and the interaction is formally non-bonding in the ground state. However, upon excitation (for instance, from the absorbance of UV light), one of the electrons in the antibonding molecular orbital of the  $5d_{z^2}$  atomic orbitals is promoted into the bonding molecular orbital of the  $6p_z$  atomic orbitals. This leads to a strengthening of the Au...Au contact for a formal bond order of one. Subsequently, luminescence occurs to allow the system to relax back to the ground state. The emission profile is related to the Au...Au contact distance and in most cases a shortening of these contacts leads to a red-shift since the HOMO-LUMO energy gap decreases. Contact distances can be perturbed by such factors including interaction with an analyte, temperature, pressure, and differing polymorphs.

Au-Au interactions are defined by gold-contact distances of less than 3.60 Å with strengths around 5-15 kcal mol<sup>-1</sup> which is comparable to a hydrogen bond.<sup>68</sup> These interactions when of the distance 2.6-3.4 Å, have been found to be emissive with the emission profile dependent on the length of the Au-Au contacts.<sup>68-70</sup> The

application of aurophilic interactions for chemical sensing purposes can also be understood more deeply by considering the molecular orbitals involved. The antibonding HOMO is destabilized while the bonding LUMO is stabilized as the Au $\cdots$ Au distance is decreased.<sup>71</sup> This decrease in the HOMO-LUMO energy gap makes it sensitive to even slight perturbations in the contact distance brought about by analyte-driven structural changes. Even small distortions that change the Au-Au contact distance by 0.1 Å have been shown to result in observable changes in luminescence.<sup>72,73</sup> A red shift in emission profile is expected on shortening of gold-gold contact distances.

Cu(Me<sub>2</sub>S)[Au(CN)<sub>2</sub>], a white-light emitter combining the individual blue, green/yellow, and red emissions of Cu-NC, Au $\cdots$ Au, and Cu-SR<sub>2</sub> respectively, and Ln[Au(CN)<sub>2</sub>]<sub>3</sub>·3H<sub>2</sub>O (Ln = La, Gd and several others) are examples of materials that display Au-Au based emissions.<sup>74,75</sup>

## 1.2 Synthetic Techniques

### 1.2.1 General Synthetic and Crystallization Methods

The synthetic approaches utilized for this thesis were by and large straightforward. The nodes and linkers are dissolved in an appropriate solvent after which the linker is added to the node. At this stage, two outcomes can occur (assuming a product forms). The coordination polymer, which generally has low solubility, can either (1) precipitate out immediately or (2) the two components may remain in the solvent at which point the mixture can be concentrated to get the product out. Rapid precipitation in the case of 1 leads to powders which are specimens with large numbers of randomly oriented crystallites. This contrasts with single crystals which are solid materials defined by a three-dimensional assembly of atoms in an ordered array. Powders are amenable to the study of the properties of interest in this thesis but there are applications such as ferroelectricity, birefringence, and second harmonic generation where the desired property is enhanced in a single crystal sample. Additionally, structural determination from single crystals is a much

more powerful and facile approach when compared to powder XRD methods which require fitting a calculated profile with many approximations of free variables to the experimental data. One of the main principles to increase the likelihood of obtaining single crystals is to decrease the rate at which the two components are introduced to one another. Generally, high quality crystals are ones that grow slowly out of reaction mixtures with a small number of nucleation sites.

A variety of bench top techniques were used to produce single crystals of quality amenable toward structural determination. The simplest of these techniques is slow evaporation of the synthetic mixture that results from the mixing of dilute solutions of node and linker. As the solvent evaporates, the concentrations of node and linker gradually increases until a saturation point is reached at which point nucleation of the mixture occurs and crystal growth begins. Evaporating samples were sealed with parafilm (with the number of holes adjustable to the desired evaporation rate) and left in a sand bath to limit vibrations from the environment which could induce additional undesired nucleation. Diffusion based crystallization methods such as solvent layering and vapor diffusion were employed in cases where the coordination polymer precipitated out rapidly regardless of dilution or were too soluble in a particular solvent respectively.

Solvent layering exploits density differences between solvents (Figure 1.7.). Either the node or linker can be dissolved in the denser of the two solvents and carefully dispensed to the bottom of a test tube or vial. A solvent that is miscible with the first and also less dense can then be dispensed to form a buffer region on top of which the remaining component dissolved in either this same solvent or another less dense, miscible solvent is added. The containment vessel can then be sealed and over time the two components will slowly diffuse into the buffer region. The size of the buffer region and the use of mixed buffer systems to further slow diffusion was modified as necessary.

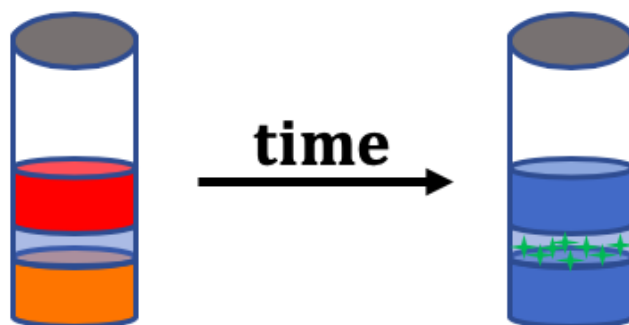


Figure 1.7. Typical solvent layering setup. The two components (red and orange) diffuse into the buffer region over time producing green crystals.

Vapor diffusion is a method that exploits the difference in vapor pressure between a solvent and antisolvent (Figure 1.8.). A sample of the reaction mixture with the solvated polymer is transferred to a 1-dram vial and placed into a 4-dram vial. An antisolvent (solvent in which the polymer is not soluble in) with higher vapor pressure and is miscible with the solvent is selected and dispensed into the 4-dram vial and the system sealed. Overtime, the antisolvent will diffuse into the solvent in the 1-dram vial, hopefully crystallizing the coordination polymer. There are many other crystallization techniques that have not been mentioned but regardless of the particular technique employed, they all revolve around the principles of keeping local concentrations low and reducing the number of nucleation sites.

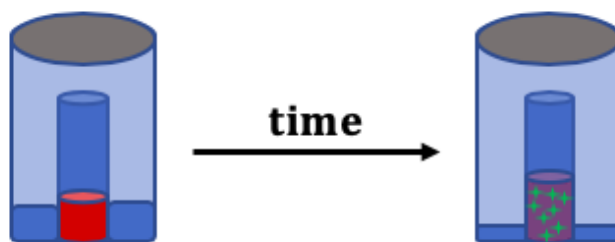


Figure 1.8. Typical vapor diffusion setup. The highly soluble coordination polymer (red) sits in the inner vial as anti-solvent diffuses in over time producing green crystals.

### 1.2.2 Solvothermal Synthesis and Crystallization

Solvothermal methods were used to synthesize and crystallize materials that proved to be difficult to crystallize using the techniques mentioned in 1.2.1. Solvothermal synthesis involves the sealing of starting materials into reaction vials able to withstand high temperature and pressure. The synthesis in this work was done using Biotage Microwave Reaction Vials and caps held in a bolted metal tray in a Yamato forced convection oven. Temperatures higher than the normal boiling point of solvent can be obtained using solvothermal setups. The high temperature and pressure environments of these reactions promote increased solubility, which circumvents the low solubility of coordination polymers and or starting materials. Three-stage temperature profiles were used with an initial heating phase, a plateau period, and a long cool down period (Figure 1.9.).

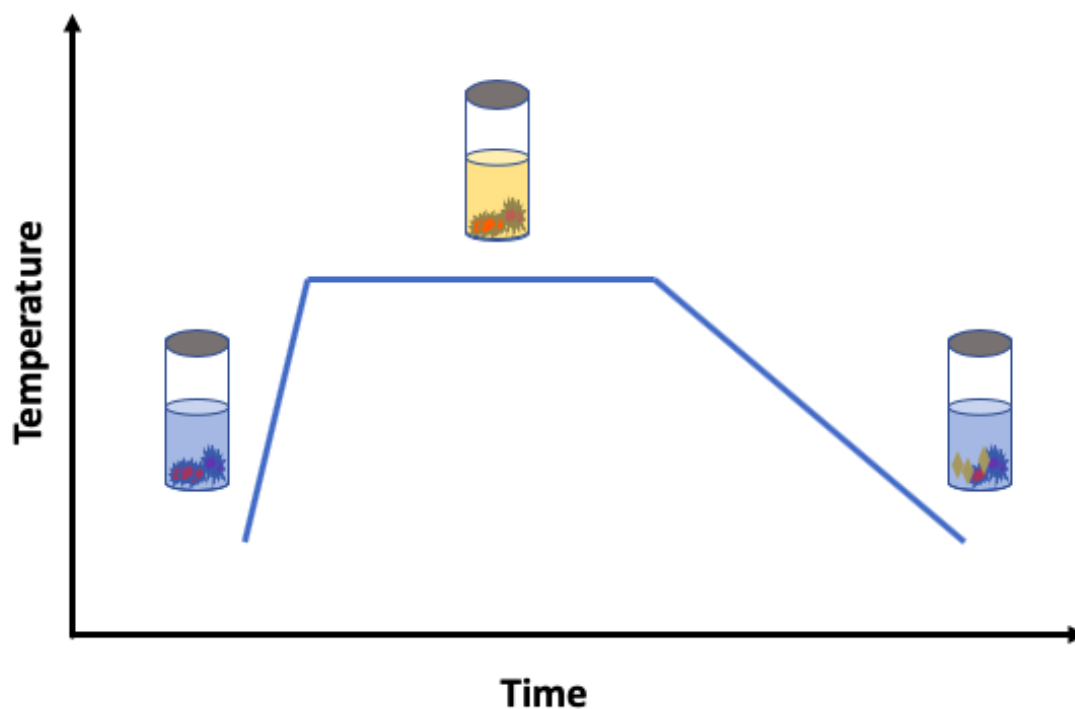


Figure 1.9. Typical solvothermal reaction profile. The temperature profile consists of an initial heating phase followed by a plateau period and a long cool down phase. The figure illustrates some of the starting materials solubilizing at higher temperatures producing a yellow product, which crystallizes upon cooling.

The rationale behind this method is that a small amount of the normally insoluble polymer can be solubilized and thus (hopefully) form crystals during the prolonged cooling period. Main drawbacks of this method involve side-reactions occurring under the harsh conditions leading to multiple products and decomposition of the starting materials or product. Solvothermal synthesis is ideal for producing a single crystal for structural determination but the powder samples produced by the more mild methods of 1.2.1. tended to result in a cleaner sample.

## **1.3 Characterization Techniques**

### **1.3.1 General Characterization Techniques**

The solid-state structures of the materials in this thesis were elucidated through single crystal X-ray diffraction (SC-XRD). However, the composition of the crystal structure does not always relate to the bulk composition of a sample. For instance, the crystal can be a minor product of a reaction. Combustion analysis (or elemental analysis (EA)) is a technique that is widely employed to affirm the bulk composition of a sample. Carbon, hydrogen, nitrogen, and sulfur are converted into their oxidized forms of  $\text{CO}_2$ ,  $\text{H}_2\text{O}$ ,  $\text{NO}$  or  $\text{NO}_2$ , and  $\text{SO}_2$  respectively, separated by a gas chromatograph and quantified using a thermal conductivity detector. Comparison of the mass percentages of C, H, N, and S in a sample with those of the empirical formula of a proposed product allows for the determination as to whether that product has been obtained. Additionally, it can allow for the detection of impurities such as unreacted starting materials or disordered solvent which may be hard to resolve crystallographically especially in the case of a poor quality X-ray dataset.

The vibrational structure of the materials covered in this thesis were studied using two techniques: Fourier-transform infrared (FT-IR) spectroscopy and Raman spectroscopy. These methods allow for the probing of vibrational modes that involve changes in the dipole moment and polarizability respectively. FT-IR provides details on the structural components (e.g. incorporated ligands or solvation) in a material and can also offer clues as to whether a reaction has

occurred by comparing against the vibrational fingerprint of starting materials. The materials in Chapter 3 all incorporate dicyanoaurate, which exhibits strong  $\nu_{CN}$  bands in the IR whose frequency gives insight into the binding modes of the linker. Additionally, it is expected that there will be shifts in the  $\nu_{CN}$  in an analyte sensitive cyanometallate coordination polymer if the analyte invokes a structural rearrangement. These shifts allow a quick determination as to whether the material is reacting with the analyte and a qualitative assessment as to the degree of conversion. Shifts in  $\nu_{CN}$  can be used as a basis for sensing itself due to the high resolution of IR and Raman instruments. As these devices become less expensive and more miniaturized, their use in sensing applications may increase, considering minute changes in vibrational fine structure can more easily be resolved than similar magnitude changes in a fluorescence-based sensor.

X-ray diffraction allows the determination of atomic positions within a crystal. The crystal is subjected to a collimated beam of X-rays producing a diffraction pattern from which the location of atoms can be mapped. This technique allows the absolute determination of the structure without the aid of other characterization techniques if large, high quality crystals can be grown. Crystals in this thesis were mounted on a 150  $\mu\text{m}$  MiTeGen Dual-Thickness MicroMount using paraffin oil and data collection performed either at room temperature or 150 K. All crystallographic data was collected on a Bruker SMART APEX II Duo CCD diffractometer with TRUIMPH graphite-monochromated Mo  $K\alpha$  radiation ( $\lambda = 0.71073 \text{ \AA}$ ) or a Cu  $K\alpha$  ( $\lambda = 1.54178 \text{ \AA}$ ) Incoatec microsource. All structures were solved with intrinsic phasing method<sup>76</sup> and subsequent refinements performed using SHELXle.<sup>77</sup> All non-hydrogen atoms were refined anisotropically. Diagrams were prepared using ORTEP-3<sup>78</sup> and POV-RAY.<sup>79</sup>

### 1.3.2 Fluorescence Spectroscopy

Fluorimetry was used to characterize the sensor materials discussed in Chapter 3 which exhibit luminescent responses to ammonia exposure. This method can be used to characterize both the excitation and emission profiles of a sample. The

excitation maxima are determined by performing a wavelength sweep of monochromated incident light applied to a sample and monitoring the emission at a specific wavelength. On the contrary, the emission maxima are determined by fixing the wavelength of the incident light and sweeping the emitted light over a wavelength range.

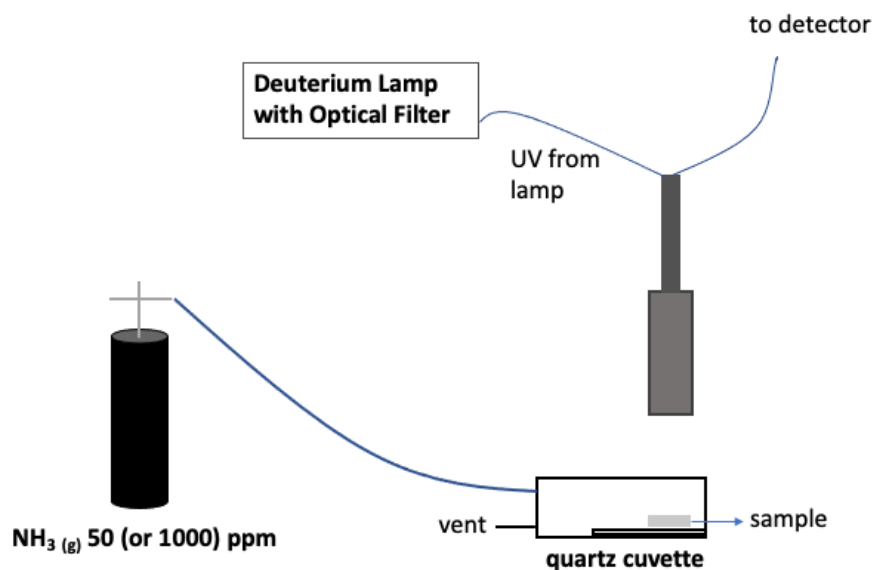


Figure 1.10. Setup used to assess the limit of detection and reversibility.

Another method of monitoring the luminescence of a sample was used to assess the sensitivity and reversibility of potential sensor materials (Figure 1.10.). This involved dynamic monitoring of the entire UV-visible range at once. A short-pass filter is used to restrict the incident light to the UV-range where the materials in this thesis have excitation bands. All light at wavelengths longer than the cut-off range of the filter that is detected is presumed to be luminescence from the sample. Emission analysis can be done rapidly with this method; only a few seconds are needed per spectra especially if the luminescence is bright. The ammonia used in this setup was supplied from commercially purchased cylinders of either 50 or 1000 ppm ammonia balanced with air or nitrogen, respectively, and manufactured with an accuracy of  $\pm 5\%$ .



### 1.3.3 Measurement of Refractive Index

The following condition is satisfied when light passes from a high index medium into a lower index one where  $\theta_r$ ,  $\theta_i$ ,  $n_r$ , and  $n_i$  are the angle of refraction, angle of incidence, index of the medium of refraction, and index of the medium of incidence respectively.<sup>31,80</sup>

$$\sin \theta_r = \frac{n_i}{n_r} \sin \theta_i < 1$$

Light experiences total internal reflection back into the high index medium when the angle of incidence exceeds the critical angle which corresponds to  $\sin \theta_r = 1$ . The sample is contacted to a standardized reference prism and the critical angle and hence index is determined. Indices with precisions of  $10^{-5}$  in the visible and near-IR can be realized.<sup>81</sup> However, the method is severely sensitive to incomplete contact between the sample and prism which leads to uncertainty in the critical angle and as such the IR determination.<sup>82</sup>

The refractive index of the bulk powder samples was determined after confirmation of bulk purity through EA. The powders were hand grounded using a pestle and mortar to promote homogeneity in particle size and subsequently pressed into pellets using a hydraulic press and a commercially purchased 13 mm evacuable die set. A Metricon 2010/M refractometer using the prism coupling technique was used to determine the RI of the powder samples discussed in Chapter 2.

In this setup, pressed pellet is pressed against a standardized prism by a pneumatic piston creating a small air gap between the pellet and prism. A 1552 nm laser diode strikes the base of the prism, and while the photons are normally reflected onto a photodetector, there are discrete angles of incidence where the photons tunnel across the air gap into the pellet entering a guided propagation mode. This leads to a decrease in intensity at the detector at these angles with the approximation that the angular location of the first mode determining the index of the sample.<sup>83</sup> The refractometer used is capable of measuring refractive index values with accuracies of  $\pm 0.0005$ . However, the indices reported in this thesis

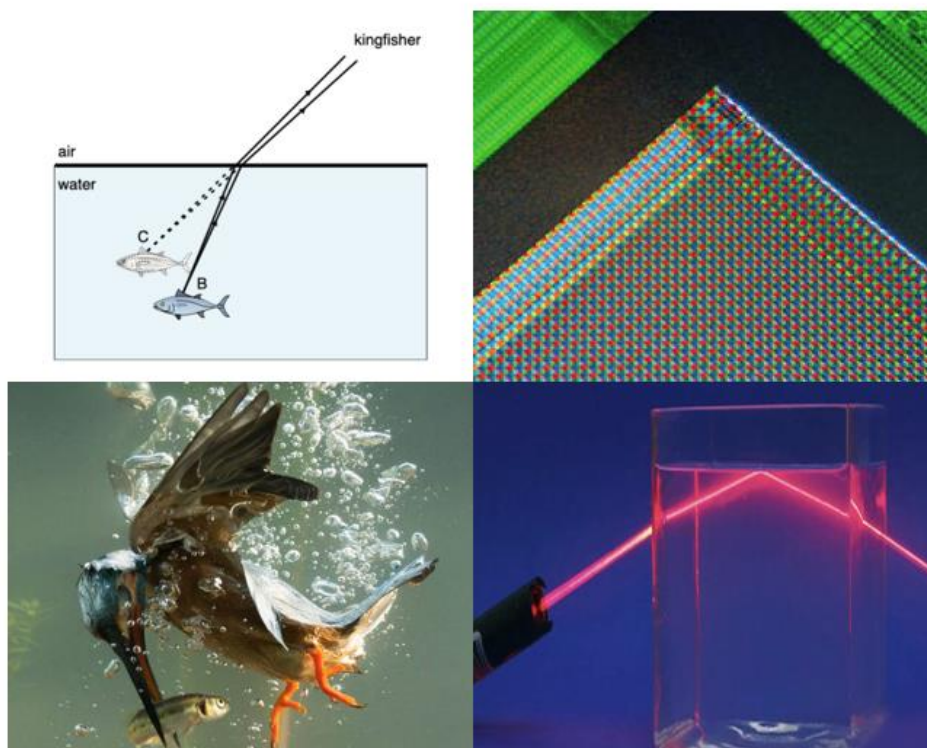
are reliable only to the second decimal place. The reason for this difference is that the determination of the angles discussed above has a significant influence on the uncertainty of the measurement since they are approximated using two intersecting lines to find the location where the intensity of light that reaches the detector reaches a minimum. Thickness of the pellets were approximated to be about 1 to 1.5 mm as produced from 2 to 4 milligrams of sample. Measurements were performed on each sample at least twice to assess the reproducibility of this method.

Other methods, that were not explored in this thesis, to determine the refractive index exist. The index of bulk crystals and glasses can be determined precisely using prisms cut out of these materials<sup>84–89</sup> using a Michelson-type interferometer<sup>90,91</sup> or by ellipsometer methods.<sup>92</sup> Immersion methods that compare indices of unknown materials to known liquid standards are often used for solid powders<sup>93,94</sup> whereas optical diffraction methods can be used for powders suspended in liquid media.<sup>95,96</sup>

A technique called the immersion method can be used to determine the index of polycrystalline materials and works on the basis of optical dissolution. Optical dissolution is an observation whereby a material becomes invisible in a medium with matching index. A wide range of calibrant medium with precisely known indices are desirable to match against samples with unknown index. These media are commercially available up to indices of approx. 2.1 and higher limits can be achieved by heating alloys of sulfur with selenium or thallium halides.<sup>97</sup>

## Chapter 2

### Refractive Coordination Polymers



**Top left:** Objects in water appear closer to the surface than they actually are because of light bending due to refraction. Due to the difference in the speed of light in water and air, light reflected from B appears to originate from C. **Bottom left:**<sup>98</sup> Kingfishers dive into water bodies to catch prey and must account for refraction by aiming below where they perceive the prey to be. **Top right:**<sup>99</sup> A microscope image of the photosensor array of a webcam. **Bottom right:**<sup>100</sup> As light passes from a medium of high index to one of low index, the transmitted component is refracted into a path lying close to the interface. As the angle of incidence increases, the transmitted component diminishes while the reflected component increases; at angles greater than the critical angle, transmission ceases leading to the occurrence of total internal reflection.

## 2.1 Introduction

The ability of a material to refract light is an important consideration in the design of optical devices. The absolute refractive index,  $n$ , is defined as follows and is a measure of the speed at which light propagates through a medium compared to in a vacuum.

$$n = \frac{c}{v}$$

$c$ : velocity of light in vacuum ( $299,792,458 \text{ m s}^{-1}$ );  $v$ : velocity of light in the medium

Refraction is the boundary phenomenon in which electromagnetic (EM) radiation is bent or refracted as it passes at an oblique angle through interfaces between medium of differing compositions with different refractive indices.<sup>31,101</sup> When EM radiation encounters a boundary, a portion of the wave is reflected back and a portion transmitted. It is this transmitted portion that undergoes refraction. To better understand this on the macroscopic scale, the two media at a boundary can be differentiated as being slow or fast in regards to the propagation speed of the light. In Figure 2.1. the left side (green), corresponding to a lower  $n$ , is the fast medium and the right side (red), corresponding to a higher  $n$ , the slow medium.

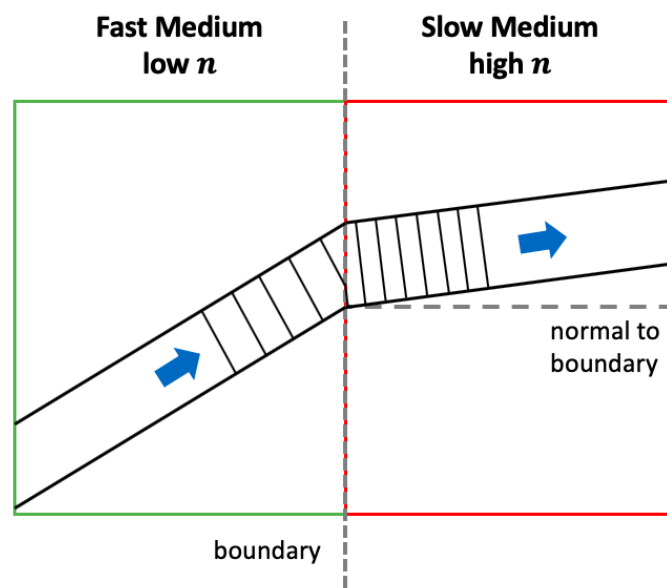


Figure 2.1. Refraction of light at a boundary separating two mediums of differing  $n$ .

The wavefront of light travelling at an oblique angle in the faster medium will reach the boundary between the two at a different time. The part of the wavefront that arrives first (bottom) will be slowed first promoting pivoting of the rest of the front towards the normal to the boundary leading to refraction. The boundary behaviour can be described by Snell's law, which illustrates that the ratio of the sines of the angle of incidence and refraction is equivalent to the ratio of phase velocities in the two media or the inverse of the ratio of refractive indices.

$$\frac{\sin\theta_1}{\sin\theta_2} = \frac{v_1}{v_2} = \frac{n_2}{n_1}$$

Since ( $v = f\lambda$ ;  $v$ : velocity,  $f$ : frequency,  $\lambda$ : wavelength) and the frequency, which is characteristic of the source, is conserved, there must be a concomitant decrease in the wavelength of light in higher index materials relative to a vacuum. The wavelength in a medium of  $n = 2$  would be half that seen in a medium of  $n = 1$ . The refractive index (RI) is a measure of the ability of a material to refract EM radiation. Table 2.1. highlights the refractive indices of an assortment of common materials.

Table 2.1. Refractive Indices of Common Media<sup>80</sup>

Material	Index <sup>a</sup>	Material	Index <sup>a</sup>
Vacuum	1.0	Crown glass	1.522
Dry air, 1 atm 15°C	1.00027	“extra light” flint glass <sup>c</sup>	1.543
Water	1.3324	flint glass <sup>c</sup>	1.607
CaTiO <sub>3</sub> (perovskite)	2.740	“dense” flint glass <sup>c</sup>	1.746
ZrO <sub>2</sub> (zirconia)	2.160 <sup>b</sup>	TiO <sub>2</sub> (rutile)	2.755 <sup>b</sup>

<sup>a</sup> At sodium D line, average wavelength 589.3 nm

<sup>b</sup> Birefringent materials; average value reported

<sup>c</sup> Varying mass% of PbO: extra light, 24; flint, 44; dense, 62.

In this work, refraction will be considered on the atomic or molecular level. The slowing down of light is a manifestation of the polarization of light from interaction with charged species that make up a material. It is found that the refractive index is intimately related to the magnitude of the relative permittivity, which is a measure of the ease of a material to become polarised when subject to an electric field. There are multiple contributors to the relative permittivity including: (1) permanent molecular dipoles, (2) charged ions, and (3) electrons.

$$n^2 = \epsilon_r$$

$n$ : refractive index,  $\epsilon_r$ : relative permittivity

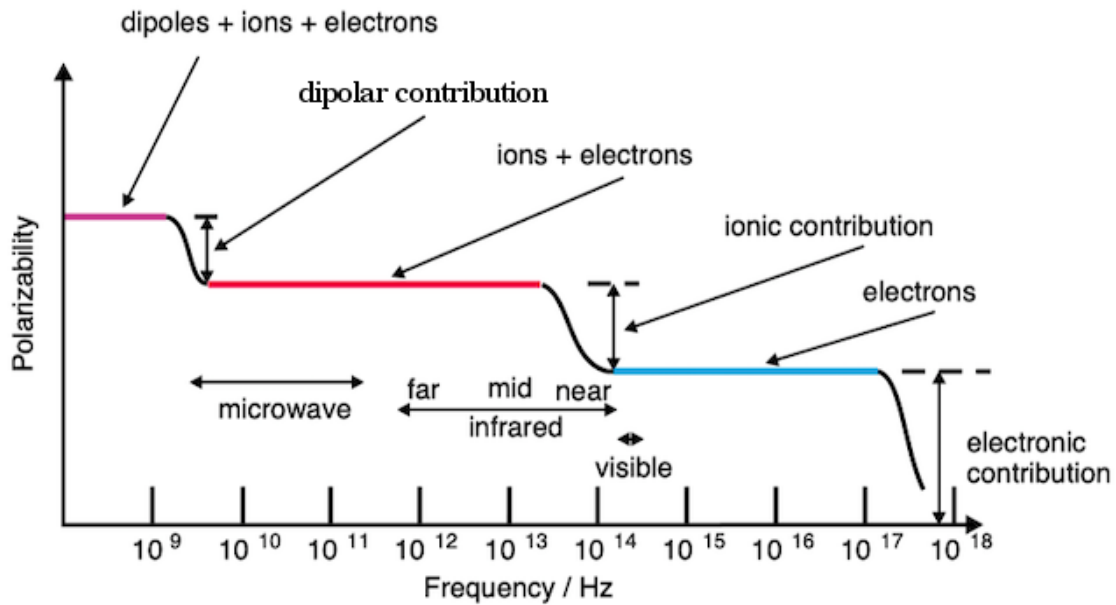


Figure 2.2. Relative contribution of permanent molecular dipoles, charged ions, and electrons at different frequencies.<sup>102</sup> Used with permission.

The relative contribution from each varies by frequency of the field (Figure 2.2.). The contribution from permanent molecular dipoles is lost entering the microwave region, that of the ionic contribution lost in the near infrared, making the electronic contribution the only factor at visible frequencies. Index measurements were performed at 1552 nm in this thesis, making the overall polarizability a sum of an

ionic and electronic contribution.<sup>1</sup> Applying a static electric field to a material polarizes (lining up with the field) the internal charge-carrying components. In the case of electromagnetic radiation, which contains not a static electric field but instead an alternating field, the charge-carrying contributors oscillate with the alternating electric field. This is the basis behind the operation of microwave ovens. The oven irradiates food with radiation in the microwave region of the electromagnetic spectrum; the alternating electric field causes dipoles to oscillate back and forth producing thermal energy that heats up the food. Classical electromagnetic theory considers this electric field-driven oscillation in charge-carrying species to emit a secondary electromagnetic wave of conserved frequency but reduced velocity compared to a vacuum. This reduction in velocity is measured as the refractive index.

Directionality in the orientation of charge-carrying species is also considered. The charge-carrying species in a medium can be arranged in an isotropic, directionally-independent, fashion which leads to the same  $n$  being observed regardless of which path the light takes. The contrary is also possible, where the charge-carrying species are arranged in an anisotropic, directionally-dependent, fashion. Under this situation,  $n$  differs on the direction the light takes through the medium leading to birefringence. Birefringent materials will be discussed in 2.6.

The RI is an important consideration in the design of optical components. Materials that refract light are ubiquitously found in a wide variety of photonic components including as encapsulant materials,<sup>103,104</sup> lenses,<sup>105</sup> waveguides,<sup>106</sup> and coatings.<sup>107</sup> Continuing advances in the field of photonics has necessitated

---

<sup>1</sup> The refractometer used was also equipped with a 532 nm laser. Measurements were attempted at this wavelength but the increased scattering that occurs at this lower wavelength resulted in undesirable instrument response and data of reduced validity. 1552 nm is also desirable since it is outside of any expected absorbances in these materials, preventing the need to describe the imaginary part of the complex refractive index that represents absorptive properties; this is also a typical telecommunications wavelength. One caveat of using 1552 nm is potential absorption from water, which can increase error in the measurements of compounds that are more laden with water.

investigation into refractive materials and in particular the idea of producing high index materials that can be used in optical applications.<sup>108–111</sup>

Internal reflection is a significant consideration in optical component design. Light crossing boundaries between media can be either transmitted or reflected. An effect called total internal reflection occurs when light travels between the boundary between a higher index medium and one of lower index. As the angle of incidence,  $\theta_1$ , at which the light approaches the boundary increases, the angle,  $\theta_2$ , at which the emergent ray enters the low index medium also increases (Figure 2.3). With increasing  $\theta_1$ , the amount of reflection of the light back into the high index medium also increases along with the corresponding decrease in intensity of the refracted emergent ray. As  $\theta_1$  is continually increased, eventually a critical angle,  $\theta_c$ , is reached at which the transmitted ray travels along the boundary surface (Figure 2.3, c). No light is transmitted with the entirety being internally reflected (total internal reflection) at all angles in excess of  $\theta_c$  (Figure 2.3, d). This leads to the light effectively being trapped in the higher index medium. The critical angle is related to the indices of the medium by:

$$\sin\theta_c = \frac{n_2}{n_1} = \frac{n_{low}}{n_{high}}$$

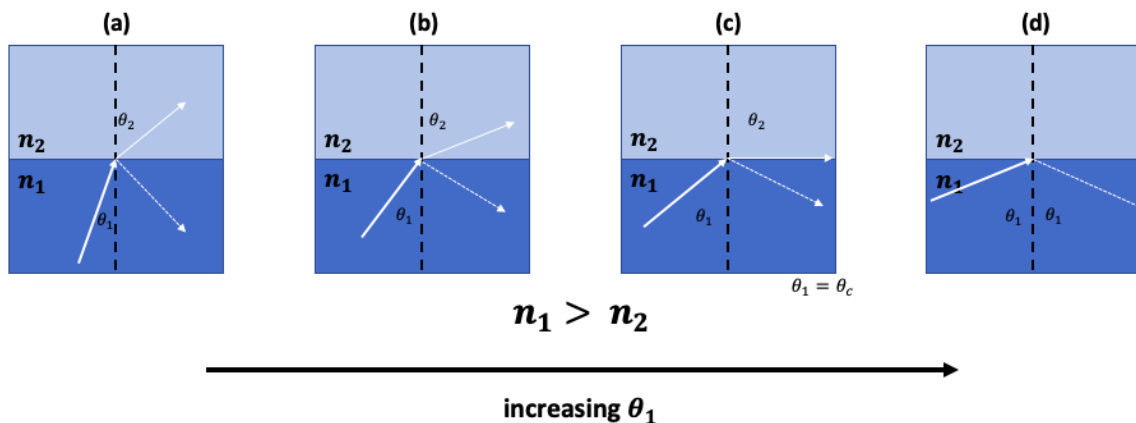


Figure 2.3. Effect of increasing angle of incidence on the refracted and reflected rays of light as it travels from a high to low index medium. The angle of incidence is increased from left to right.



Some consequences of this internal reflection is loss of coupling efficiency in optical devices when the index of the active circuitry (e.g. fibre optics) greatly contrast that of the encapsulant material.<sup>106,112</sup> This is also seen in light-emitting diodes (LEDs), particularly in the design of high-brightness variants. A low light extraction efficiency, which results from the mismatch in index between the inorganic LED (e.g. GaP,  $n = 3.45$ ) die and the organic encapsulant support ( $n < 1.80$ ), is the main hurdle.<sup>104</sup> The organic support is the low- $n$  component; if the ceiling on the index on the organic component can be raised, this can minimize the internal reflection that occurs when light produced by the die crosses into the encapsulant leading to a greater illumination efficiency. The same enhancement in efficiency can be realized in other photonic and optoelectronic devices by taking care to minimize the differences in the indices between various components. Access to novel high- $n$  medium will allow easier interfacing with the more highly refractive components found in these devices.

Another consideration in optical design is thickness of lenses. Lenses are governed by the principles of refraction which are a function of the curvature and refractive index of the lens. Lensmaker's formula can be used by lens manufacturers to craft lenses of desired focal length.

$$\frac{1}{f} = (n - 1) \left( \frac{1}{R_1} - \frac{1}{R_2} \right)$$

where  $f$  is the focal length,  $n$  is the index of refraction and  $R_1$  and  $R_2$  the radii of curvature of the two sides of a lens. As the radii of curvature is increased, the lens becomes thinner. Lenses made of high index materials can achieve a shorter focal length than those that are less refractive. This has implications in device miniaturization since thinner refractive surfaces may be used in modern photonic devices if the index is higher.<sup>111</sup> Considering a simple biconvex lens, consisting of two fused convex lenses, if the radii of both sides is equivalent the relationship simplifies to

$$\frac{1}{f} = (n - 1)$$

From this, it is seen that shorter focal lengths can be achieved for high index materials. The optical power,  $P$ , of a system is a measure of the degree to which an optical system (e.g. lens, mirrors) can converge or diverge light and is equal to the reciprocal of the focal length.

$$P = \frac{1}{f}$$

Optical systems with short focal lengths have high optical power which is required for improving optical performance of devices. In summary, the motivation behind achieving more highly refractive medium is two-fold: (1) using functional materials with higher index generally leads to higher performance devices and (2) the thickness of a refractive surface can be decreased providing the opportunity to miniaturize devices.

## 2.2 Design Criteria for High Index Materials

It is important to assess the considerations that lead to a high index material. The Lorentz-Lorenz relationship can be used as the guiding criterion for the design of high index materials:<sup>97</sup>

$$\frac{n^2 - 1}{n^2 + 2} = \frac{4\pi}{3} \frac{\rho N_A}{M_W} \alpha = \frac{4\pi}{3} \frac{\alpha}{V_{mol}}$$

where  $n$  is the refractive index,  $\rho$  the density,  $N_A$  Avogadro constant,  $M_W$  the molecular weight,  $\alpha$  the molecular polarizability, and  $V_{mol}$  the molecular volume. From this, it is seen that the highest index materials will come from using substituents that have the highest volume ratio of polarizability ( $\alpha/V_{mol}$ ). Under this scenario, the electric field driven oscillation of charge density is strongest leading to the most reduced light speed. To achieve the highest volume ratio of polarizability, attention must also be paid to use building blocks that can pack together tightly leading to a lower  $V_{mol}$  (Figure 2.4.).

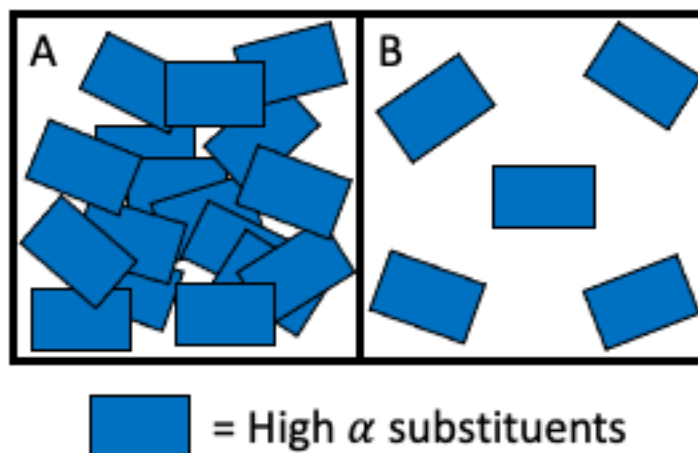


Figure 2.4. A: High  $\alpha/V_{mol}$ , the building blocks are able to pack together tightly; B: low  $\alpha/V_{mol}$ , the building blocks are diffuse

Highly polarizability substituents that have been used in refractive index studies include building blocks with aromatic rings (e.g. -phenyl, -naphthyl), halogen atoms excluding fluorine, and sulfur atoms (e.g. thiocarbonyl, thiols) especially those present in low oxidation states. Additionally, polarizable metal cations have also been investigated for their use in making high index materials.<sup>110</sup>

## 2.3 The Current Landscape of High Index Materials

The current synthetic methods to access high index materials are through (1) intrinsic high refractive index (HRIP) polymers and (2) HRIP nanocomposites.

### 2.3.1 Intrinsic High Refractive Index Polymers

The indices of conventional polymers such as polyethylene, polypropylene, and polystyrene have indices in the range of approximately 1.30-1.70. Intrinsic HRIPs contain substituents with high electronic polarizability to push the upper limit on this range. Substituents which are commonly used to achieve this include aromatic species, halogens (excluding fluorine, which has a low polarizability), sulphur atoms, or polarizable metal cations.<sup>110</sup> Incorporation of these groups into a polymer

leads to an additive synergistic effect, allowing tunability of the material towards desired indices.

The first systematic investigation into halogen-functionalized polymers was performed in 1992 by Gaudiana *et al.* They reported the polymerization of unsaturated monomers with pendant halogenated carbazoles, producing high index materials in the range of 1.67 to 1.77 depending on the type of halogen.<sup>113</sup> The researchers also describe the ability to use their materials as optical binding agents since it can be liquified and polymerized between the elements of devices.

HRIPs that contain sulfur in the form of thioethers,<sup>114</sup> thianthrenes,<sup>115</sup> and sulfones,<sup>116</sup> amongst many other types of functionalizations have been studied. Ueda and colleagues synthesized sulfur-containing aromatic polyimides through a two-step reaction, involving polycondensation followed by thermal imidization from the starting dianhydrides and diamines.<sup>114,116–120</sup> Some of these polyimides and their observed indices of refraction are displayed in Figure 2.5.

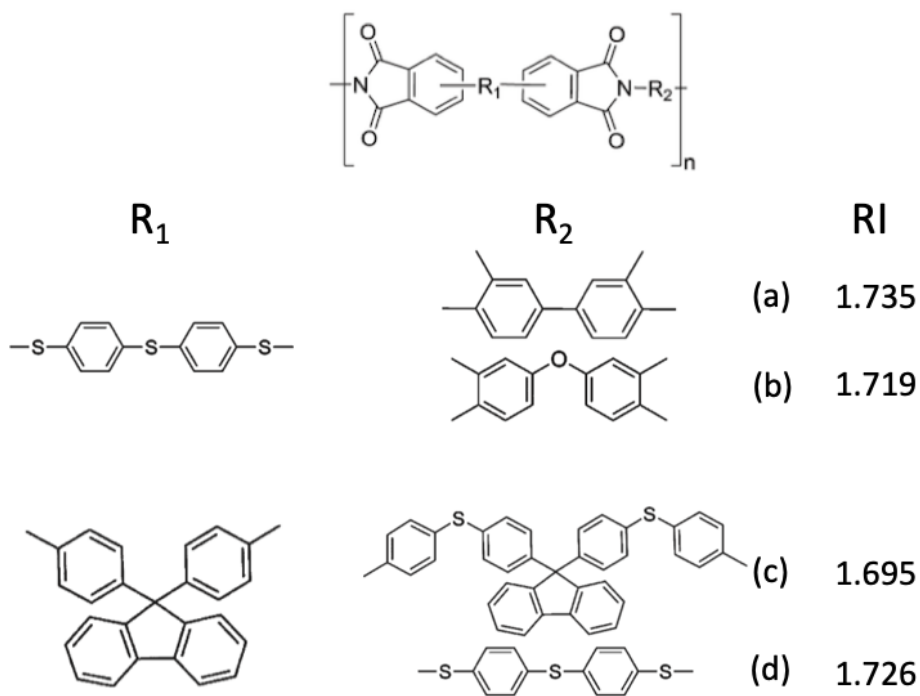


Figure 2.5. Indices of polyimides with varying substituents<sup>110</sup>

As expected from the Lorentz-Lorenz relationship, the polymers with the highest sulfur content by mass % have the highest indices. However, as discussed in 2.2, there is also a significant contribution from the packing efficiency of the material. This is seen through comparison of polyimide **c** with **d** above (Figure 2.5.). The former has much more steric bulk which hinders the ability to pack tightly, leading to a lower index observed (1.695) compared to the latter, which is more compact with a higher ability to pack (1.726).

Other than halogen and sulfur-containing HRIPs, a vast amount of work has gone into investigating other substituents that result in high index materials. Aromatic polyphosphonates have been synthesized using polycondensation reactions and the organocatalysts *N*-methyl imidazole and 4-(dimethylamino)pyridine. The top-performing polyphosphonate has an index of 1.61.<sup>121</sup> Additionally, polyphosphazenes synthesized via ring opening polymerization that exhibit good transparency in the visible region, low optical dispersion, and high index (up to 1.755) have also been reported.<sup>122,123</sup> Polarizable main group elements can also be used to make HRIPs. Silicon, germanium, and tin have been investigated in reactions of the type displayed in Figure 2.6. involving main group vinyl (or allyl) compounds and a multifunctional thiol.<sup>111,124–126</sup>

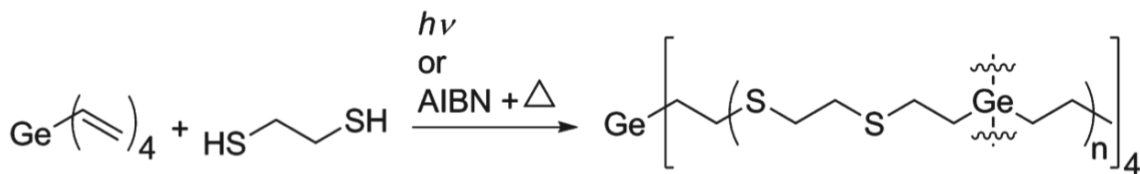


Figure 2.6. Coupling of tetravinylgermane and 1,2-ethanedithiol<sup>111</sup> Used with permission.

The polymers have good mechanical strength and the indices observed ranged from 1.590 – 1.703.<sup>125</sup>

Organometallic HRIPs have also been investigated due to the highly refractive nature of the metal. A range of polyferrocenes were synthesized by ring opening

polymerization of strained cyclic monomers.<sup>127</sup> These were also designed with main group spacers incorporating the previously aforementioned polarizable groups (e.g. phosphorus, silicon, germanium, tin,  $\pi$ -delocalized R groups) (Figure 2.7.).

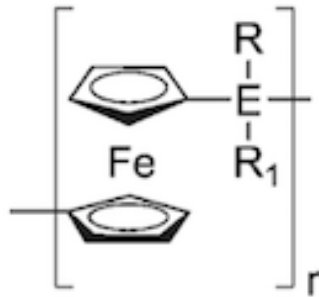
Repeat Unit	E	R/R <sub>1</sub>	<i>n</i>
	Si	R=CH <sub>3</sub> ; R <sub>1</sub> =CH <sub>2</sub> CH <sub>2</sub> CF <sub>3</sub>	1.60
		R=CH <sub>3</sub> ; R <sub>1</sub> =CH <sub>2</sub> CH <sub>3</sub>	1.66
		R=R <sub>1</sub> =CH <sub>3</sub>	1.68
		R=CH <sub>3</sub> ; R <sub>1</sub> =C <sub>6</sub> H <sub>5</sub>	1.68
	Ge	R=R <sub>1</sub> =CH <sub>3</sub>	1.69
	Sn	R=R <sub>1</sub> = <sup>t</sup> Bu	1.64
		R=R <sub>1</sub> =Mes	1.66
		R=R <sub>1</sub> =Nap	1.82

Figure 2.7. Polyferrocene HRIPs<sup>127</sup>

Intrinsic HRIPs tend to have good processability characteristics in that they are amenable towards the processes of high temperature extrusion and injection moulding that are often used in lenses or device fabrication.<sup>111</sup> The indices of these materials are also quite tunable due to the additive effect of introducing new refractive groups and they are generally stable under ambient conditions. However, there does appear to be an upper limit ( $n = 1.8$ ) on the index that can be realized using these materials. This arises from the observation that although the raw electronic polarizability is being increased, it is often coming at the cost of simultaneously increasing the molecular volume or affecting adversely the packing density. As such, the concentration ( $\alpha \text{ V}^{-1}$ ) of electronic polarizability remains relatively unchanged which imposes the upper constraint. Currently, if a higher index than 1.80 is required, it is necessary to functionalize the intrinsic HRIP with high index nanoparticles, creating an HRIP-nanocomposite.

### 2.3.2 High Refractive Index Polymer Nanocomposites

HRIP-nanocomposites, which are organic-inorganic hybrids, are produced by introducing high index nanoparticles into the aforementioned intrinsic-HRIP matrix. These inorganic-organic hybrids have been studied starting in the 1990s. Weibel et al (1991) were amongst the pioneers of this work, having developed a composite of 90% w/w lead sulfide in polyethylene glycol, which was measured to have an index around  $n = 3$ , the highest at the time for a polymer composite.<sup>128</sup>

The index of the composite is a function of the contributions from the two types of constituents and can be approximated as follows, where  $n_{composite}$ ,  $\phi_{org}$ ,  $n_{org}$ ,  $\phi_{np}$ ,  $n_{np}$  represent the index of the composite, volume fraction of the organic matrix, the index of the organic matrix, volume fraction of the nanoparticle, and index of the nanoparticle respectively.

$$n_{composite} = \phi_{org}n_{org} + \phi_{np}n_{np}$$

Generally, it is favourable to use an organic matrix of high  $n$  to reduce the  $\phi_{np}$  needed to achieve a high  $n$  composite. It has been noted high  $\phi_{np}$  loadings lead to problems such as fragility of the composite and loss of optical transparency due to opaqueness caused by aggregation of nanoparticles.<sup>110</sup> Other design considerations when making these nanocomposites include the nanoparticle size and functionalization of the surface of the nanoparticle. Diameters of less than 25 nm are desirable since anything larger results in loss of optical transparency and exhibits Rayleigh scattering.<sup>129</sup> Directly mixing the nanoparticles into the reaction mix when synthesizing the polymer matrix tends to result in aggregation. As a result, the surface of the nanoparticles are often functionalized by grafting substituents to avoid this problem.

A vast number of different types of nanoparticles have been used to make HRIP-nanocomposites. Generally, if the goal is to make a high index nanocomposite, it is favourable to use a higher index nanoparticle to keep the loading fraction low.  $\text{TiO}_2$  (anatase,  $n = 2.45$ ; rutile,  $n = 2.70$ )<sup>130</sup>,  $\text{ZrO}_2$  ( $n = 2.10$ )<sup>131</sup>, amorphous silicon

( $n = 4.23$ ) , PbS ( $n = 4.20$ )<sup>132</sup>, and ZnS ( $n = 2.36$ )<sup>133</sup> nanoparticles have been investigated for their use in these composites. Two approaches, referred to as *grafting from* and *grafting to*, have been used to graft substituents leading to higher compatibility between the inorganic nanoparticle and organic matrix.<sup>134,135</sup> In the former, monomeric units are allowed to diffuse to the nanoparticle at which point surface-initiated polymerization techniques can be used to affix the polymer chain onto the nanoparticle. To contrast, the latter approach involves coupling of polymeric chains containing an active terminal group to functionalized nanoparticles. A Cu(I) catalyzed azide-alkyne cycloaddition click reaction has been widely used to graft polymer chains to nanoparticles. This has been performed on surfaces including titania, silica, gold nanoparticles, and luminescent quantum dots amongst many others. The amount of enhancement seen in the  $n$  of the nanocomposite relative to that of the organic matrix depends on the loading percentage of nanoparticle.<sup>136</sup> Sulfur containing polyimide-TiO<sub>2</sub> nanocomposites that are optically transparent have been reported. The polyimides films have indices ranging from 1.6799-1.7130 measured at 632.8 nm. Upon grafting to silica-modified TiO<sub>2</sub> nanoparticles, the index of the composite was observed to be enhanced to 1.8100 at 632.8 nm.<sup>137</sup> There are other synthetic approaches that can be utilized to access these nanocomposites. High- $n$  aminoalkoxysilane capped pyromellitic dianhydride-titania<sup>138</sup> and poly(BPDA-ODA)/silica hybrid optical films<sup>139</sup> have been prepared with the sol-gel process. Esterification between titanium butoxide and the carbonyl endcaps of a soluble fluorinated polyimide promoted bonding between the two components generating the nanocomposite. Optically transparent films were obtained after some further chemical modifications (hydrolysis, condensation, and thermal curing). These films had indices measuring from 1.571 to 1.993.

Thus, HRIP-nanocomposites have a higher ceiling on the indices that can be realized. The index is also tunable to a degree like in intrinsic-HRIPs by varying the loading percentage of nanoparticles. However, this approach to accessing high-index materials also has some limitations. It is well observed that higher loading of nanoparticles results in processability issues including cracking,<sup>140</sup>



fragility, and scattering that leads to loss of optical transparency. These issues stem from agglomeration of the nanoparticles at higher loadings and can be partially offset by grafting organic substituents to the nanoparticles or using flexible polymer chains which both shield the nanoparticle core from aggregating.<sup>141</sup>

Comparing the two approaches that can be taken to access high-index materials, intrinsic HRIPs have a lower upper ceiling on indices that can be realized but they do have significant advantages in stability and other processability characteristics. The research described in this Chapter investigates alternative, completely novel approaches to creating a high index material drawing upon the design criteria discussed in 2.2. The work starts off with a quick survey into simple metal tungstates and molybdates before moving into larger anionic tungstate clusters (2.4). It is then investigated whether coordination polymers can be used to make refractive materials.

## 2.4 A Survey Into Tungstates, Molybdates, and Polyoxometallates

### 2.4.1 Background and Motivations

In the initial stages of this work, a synthetically facile, economically affordable, and high yielding method to produce high index materials was targeted. The naturally occurring minerals of metal tungstates and molybdates were identified as being candidates of interest due to the high refractive indices that they possess. [*CaWO<sub>4</sub>* ( $n = 1.9s$ ), *MnWO<sub>4</sub>* ( $n = 2.2s$ ), *FeWO<sub>4</sub>* ( $n = \text{up to } 2.4$ ), *CaMoO<sub>4</sub>*, *SrMoO<sub>4</sub>* ( $n = 1.9s$ ); *PbMoO<sub>4</sub>* ( $n = \text{up to } 2.4$ )]<sup>97</sup>

Tungstates and molybdates are tungsten and molybdenum compounds containing oxoanions. The simplest chemical form of these anions are  $\text{WO}_4^{2-}$  and  $\text{MoO}_4^{2-}$  referred to as the ortho- anions. These materials of the form MX (M: metal; X:  $\text{WO}_4^{2-}$  and  $\text{MoO}_4^{2-}$ ) possess interesting luminescence properties which has led to their use in applications such as optical fibers, fluorescent lamps, and scintillation counters for gamma radiation.<sup>142–145</sup>

Metal tungstates and molybdates are usually sourced from mining activities which tend to be resource intensive and also result in the ore being found in association with other minerals. Alternative methods to access these materials through simple solution chemistry producing bulk powders is desirable and thus a coordination polymer-type approach was investigated, as described below.

#### **2.4.2 Aqueous Synthesis of Metal Molybdates and Tungstates**

Metal tungstates (and molybdates) were synthesized through metathesis of sodium tungstate (or molybdate) with metal salts, including Zn(II) nitrate, Mn(II) chloride, Mg(II) nitrate, Ca(II) nitrate, Sr(II) nitrate, Ba(II) nitrate, In(III) chloride, and Pb(II) perchlorate (e.g.  $\text{Na}_2\text{WO}_4 + \text{Ca}(\text{NO}_3)_2 \rightarrow \text{CaWO}_4 + 2 \text{NaNO}_3$ ). Stoichiometric amounts of metal salts and sodium tungstate (or molybdate) were used. The resulting materials were colorless powders that could be easily filtered and collected. These reactions were energy efficient (without the need of thermal or pressurized input), high yielding, and performed on the benchtop in water without the use of specialized equipment. The powders were rendered into pellet form and the indices measured (Table 2.2.). The table is not all-inclusive since some difficulty came up in obtaining measurements for some of the materials due to their granular nature, making them less amenable towards being pressed into pellets. The concern of pursuing the rest of the index measurements was dropped after it was found that there were substantial discrepancies between the experimental values and those cited in literature.

Table 2.2. Refractive Indices of Tungstates and Molybdates

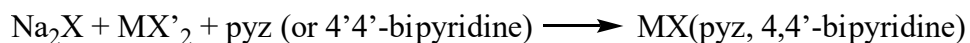
Literature values for (PbWO<sub>4</sub>, CaMoO<sub>4</sub>, SrMoO<sub>4</sub>)<sup>97</sup> and for BaMoO<sub>4</sub><sup>146</sup>

Tungstates (WO <sub>4</sub> <sup>2-</sup> )		Molybdates (MoO <sub>4</sub> <sup>2-</sup> )	
Metals	<i>n</i>	Metals	<i>n</i>
exp. Pb(II)	1.5669	exp. Ca(II)	1.6628
lit. Pb(II)	2.30	lit. Ca(II)	1.974
		exp. Sr(II)	1.6379
		lit. Sr(II)	1.926
		exp. Ba(II)	1.6933
		lit. Ba(II)	1.87

In all cases where a measurement was successfully made, the experimentally observed refractive index was seen to be lower than they should be. The synthesis of tungstates and molybdates is very sensitive to the reaction conditions (pH, temperature, pressure) of which none were controlled for in this experimentation. One explanation for the depressed indices can be the product consisting of a mixture of phases. However, this does not seem reasonable with the consideration that the tetragonal phase of PbWO<sub>4</sub> has indices of 2.27 and 2.19 at a wavelength of 671 nm depending on the crystallographic axis while the monoclinic phase has indices of 2.30 and 2.27. The surface of these pellets was highly granular, which may have led to non-ideal behaviour on the refractometer. This technique relies on the formation of a smooth interface between the sample and prism.

### 2.4.3 An Attempt to Improve Processability Characteristics of Metal Tungstates and Molybdates Using Organic Linkers

The granular, mineral-like properties of the metal tungstates and molybdates synthesized above would limit possible use in optical applications. Organic building blocks of pyrazine (pyz) and 4,4'-bipyridine were incorporated into the synthesis of the powder products of 2.4.2 according to the following reaction scheme (Figure 2.8.) in an attempt to reduce their mineral-like physical properties.



X:  $\text{WO}_4^{2-}$  or  $\text{MoO}_4^{2-}$

X':  $\text{NO}_3^-$ ,  $\text{Cl}^-$ ,  $\text{ClO}_4^-$ ,  $\text{CO}_3^{2-}$

M: Divalent Metal

Figure 2.8. Attempted synthesis of metal tungstates and molybdates incorporating organic linkers

It was hoped that in doing so, the refractive power of the metal tungstate or molybdate could be harnessed via processing techniques such as spin-coating into a thin film amenable to use in optical lenses or other components. Other than the bench-top attempts at incorporating pyz or 4,4'-bipyridine by simply adding them to the original synthesis conditions, reactions in excess pyz (or bipyridine), adding the organic first followed by the tungstate (or molybdate), changing solvent systems, and harsher solvothermal conditions were conducted. The resulting powders were assessed for the possibility of incorporation of the organic linkers with IR-spectroscopy, paying attention to the presence of any absorbances characteristic of pyz (or bipyridine). Despite these efforts, no evidence of ligand incorporation was ever observed, so this route was not pursued any further.

#### 2.4.4 Incorporation of Large Anionic POM Clusters

The approaches of 2.4.3. were unsuccessful at first glance, so an investigation into another type of tungstate system, polyoxometalates (POMs) was undertaken. POMs are polyoxoanions based on early transition metals (group 5 and 6) oxide building blocks with a general formula  $(\text{M}_x\text{O}_y)_n$  where  $\text{M} = \text{V}, \text{Nb}, \text{Ta}, \text{Cr}, \text{Mo}, \text{W}$ . The oxygen atoms bridge the metal atoms, resulting in large 3-D clusters. This type of polyoxoanion can come in two broad variations. A POM that contains one type of metal and oxygen is referred to as an isopolyoxometalate, with an example being Lindqvist hexamolybdate,  $[\text{Mo}_6\text{O}_{19}]^{2-}$ . POMs with additional elements (e.g., P, Si) are known as heteropoly acids or heteropolyoxometalates.

POMs find utility in a variety of applications<sup>147</sup> including catalysis, corrosion inhibition<sup>148–150</sup> and in dyes. Tungstosilicic acid hydrate,  $\text{H}_4[\text{SiW}_{12}\text{O}_{40}] \cdot x\text{H}_2\text{O}$ , and phosphotungstic acid hydrate,  $\text{H}_3[\text{PW}_{12}\text{O}_{40}] \cdot x\text{H}_2\text{O}$ , were identified, because of the highly polarizable nature of the anion, as candidate heteropolyoxometalates that can be investigated for their potential in creating a high-index material. Both of these are hydrates in their solid state with the water molecules decreasing the packing efficiency of the putatively high-index POM unit. The index of the material would have contributions from both the tungstate cluster and the auxiliary co-crystallants. Water has a low  $\alpha/V$  and its removal or replacement with higher  $\alpha/V$  auxiliaries would be expected to raise the index. Some of these water molecules can be substituted with pyrazine and 4,4'-bipyridine through crystallization of the POM in an excess of these reagents under solvothermal conditions. Additionally, due to their ability to act as a hydrogen bond acceptor, incorporation of pyz and 4,4'-bipyridine may coerce densification compared to the hydrated forms which would lead to a more refractive material.

The refractive power of the hydrated POMs were compared to that of the same POMs grown in an environment of pyz or 4,4'-bipyridine. The RI of  $\text{H}_4[\text{SiW}_{12}\text{O}_{40}] \cdot 28 \text{H}_2\text{O}$  and  $\text{H}_3[\text{PW}_{12}\text{O}_{40}] \cdot 30 \text{H}_2\text{O}$  were measured to be 1.71 and 1.75 respectively, thereby confirming that these materials have fairly high RI values as predicted. Replacement of some of the ligated water with pyz by crystallization under solvothermal conditions with the cluster and pyz in a 1:2 stoichiometric ratio resulted in  $\text{H}_4[\text{SiW}_{12}\text{O}_{40}](\text{pyz})_4$  (Si-pyz) and  $\text{H}_3[\text{PW}_{12}\text{O}_{40}](\text{pyz})_{3.5}$  (P-pyz) (characterized through elemental analysis) which had indices of 1.77 and 1.81 respectively. Likewise, replacement of some of the ligated water with 4,4'-bipyridine by crystallization under solvothermal conditions with the cluster and 4,4'-bipyridine in a 1:2 stoichiometric ratio resulted in  $\text{H}_4[\text{SiW}_{12}\text{O}_{40}] \cdot 5(4,4'\text{-bipyridine})$  and  $\text{H}_3[\text{PW}_{12}\text{O}_{40}] \cdot 3(4,4'\text{-bipyridine})$  which both had an index measuring to be 1.78. The results are summarized in Table 2.3.

Table 2.3. Refractive Indices of Tungstosilicic & Phosphotungstic Acid POM-systems

<b>H<sub>4</sub>[SiW<sub>12</sub>O<sub>40</sub>]</b>		<b>H<sub>3</sub>[PW<sub>12</sub>O<sub>40</sub>]</b>	
<b>Auxiliary</b>	<b><i>n</i></b>	<b>Auxiliary</b>	<b><i>n</i></b>
Hydrate	1.71	Hydrate	1.75
pyz	1.77	pyz	1.81
4,4'-bipyridine	1.78	4,4'-bipyridine	1.78

The indices of both Si-pyz and P-pyz were seen to increase by 0.06 (3.5%) over their hydrated forms. This is reasonable as the replacement of H<sub>2</sub>O with pyz would lead to an increased contribution to the index from the auxiliary component although, it is surprising that the effect was so muted.

The indices of both Si-4,4'-bipyridine and P-4,4'-bipyridine were higher than the hydrated form but are similar to that for the Si(P)-pyz. The reason for this is that although the  $\alpha$  is higher for 4,4'-bipyridine, it is unfortunately offset by an increase in  $V$ , leading to no apparent increase in the index. The index increase over the hydrated form is also just modest for both these organic molecules. This is perhaps because water is a stronger facilitator of hydrogen-bonding than pyz or 4,4'-bipyridine and thus although it has a low  $\alpha/V$  on its own, water's presence in a system that contains materials capable of hydrogen-bonding (i.e., the clusters) may serve to densify the network, and their removal may minimize any gain in index that can be realized by using higher  $\alpha/V$  auxiliaries.

## 2.4.5 Conclusions

Metal tungstates and molybdates were identified as an area of interest due to their highly refractive properties in mineral form. These materials were synthesized through simple metathesis reactions on the benchtop (2.4.2). The resulting metal tungstates and molybdates were found to have indices lower than those quoted in literature. This discrepancy is attributed to the fact that the synthesis of tungstates and molybdates is sensitive to a wide variety of conditions which were not

controlled for. Attempts to enhance the processability characteristics by incorporating organic molecules like pyrazine and 4,4'-bipyridine into the metal tungstates were not successful (2.4.3).

As a continuation from the simple metal tungstate and molybdate systems, more complex H-bonded heteropolyoxometalates systems involving  $\text{H}_4[\text{SiW}_{12}\text{O}_{40}] \cdot x\text{H}_2\text{O}$ ,  $\text{H}_3[\text{PW}_{12}\text{O}_{40}] \cdot x\text{H}_2\text{O}$ , pyrazine, and 4,4'-bipyridine were looked at (2.4.4). It is found that the index of the H-bonded network is tunable by varying the auxiliary co-crystallants. Coordination polymers incorporating POMs were not targeted in this thesis but POM-based open metal-organic frameworks are well known. It is not expected that these would have a high index since the presence of void space in the solid-state structure diminishes  $\alpha/V$ . Efforts can be made into densifying known POM-based networks by co-crystallizing high  $\alpha/V$  into the interstitial voids to see if that can increase their refractive power.

## 2.5 Extending Design Criteria to Coordination Polymers

This section explores whether the design criteria toward making a high-index material outlined in the Lorentz-Lorenz relationship, mainly a high  $\alpha/V$ , can be applied to coordination polymers. The overall refractive index of a CP is a sum of the contribution from the ligand and metal which make up the polymer.

$$RI_{TOT} = RI(L)V_f(L) + RI(M)V_f(M) \quad (3)$$

$$V_f(L) = \frac{V_L}{V_L + V_M}; \quad V_f(M) = \frac{V_M}{V_L + V_M} \quad (4)$$

where  $RI_{TOT}$ ,  $RI(M)$  and  $RI(L)$  is the total RI, RI of the metal and RI of the ligand, respectively, and  $V_f(M)$  and  $V_f(L)$  are the volume fractions of the metal and ligand, respectively. The volume fraction describes the volume proportion occupied by the metal,  $V_M$ , and ligand,  $V_L$ , of the total volume of the metal-ligand complex (equation 4).

Metal cations are expected to have high electronic polarizability. However, their volume fraction would also be low compared to the ligand, and can be approximated as small spheres of electron density, meaning that more of contribution towards the index comes from the ligand rather than metal. Ligands were selected based on the ability to survey the effect of changing  $\alpha/V$  on the index of the polymer. A set of eight novel coordination polymers were synthesized, structurally-resolved, and their refractive indices assessed.

### 2.5.1 Selection of Building Blocks

Three ligands (Figure 2.9.) were selected, with the first being 1,5-naphthalenedisulfonate, from the disodium salt. This building block contains sulfur atoms in a high valent state. The potassium salt of 5-Mercapto-3-phenyl-1,3,4-thiodiazole-2(3H)-thione was selected as the next ligand to assess the impact of increasing  $\alpha$  on the index since the sulfur atoms are in lower valent states than the naphthalenedisulfonate. Finally, the potassium salt of 1,3,4-thiadiazole-2,5-dithiol was selected as the final ligand in this study to assess the impact of  $V$  since it is structurally similar to 5-Mercapto-3-phenyl-1,3,4-thiodiazole-2(3H)-thione but without the -phenyl substitution on the heterocycle.



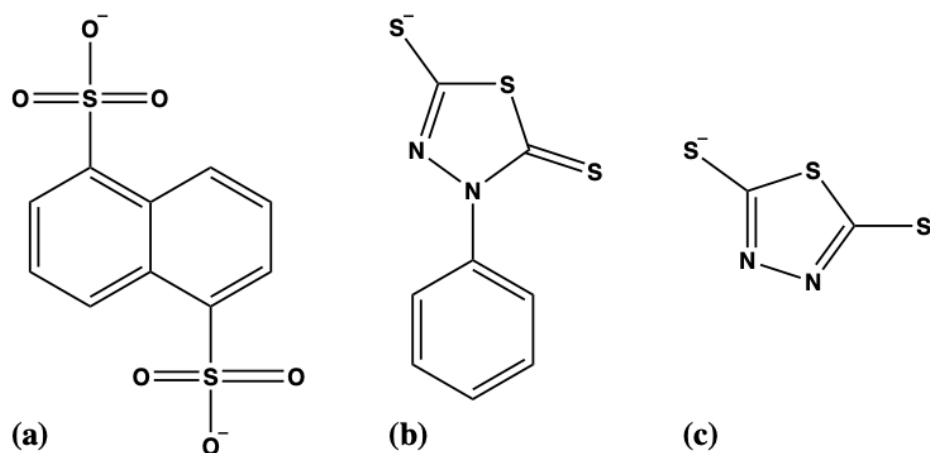


Figure 2.9. Ligand building blocks (a), 1,5-naphthalenedisulfonate (b), 5-Mercapto-3-phenyl-1,3,4-thiadiazole-2(3H)-thione (c), 1,3,4-thiadiazole-2,5-dithiol

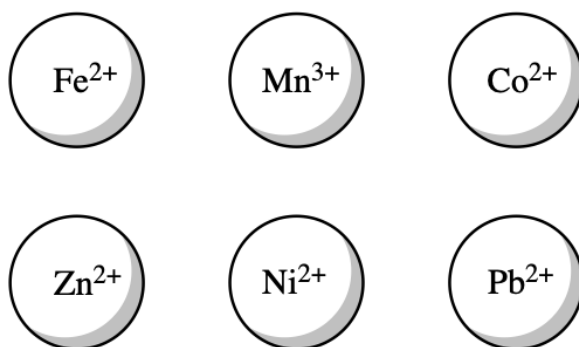


Figure 2.10. Metal node selection

A variety of transition and main group metals were used in this study (Figure 2.10.). Metal salts with non-coordinating anions such as nitrate and perchlorate were used in attempt to have the coordination polymer as just a binary system of ligand and metal. It would be undesirable to have a coordinating anion be involved in the structure since that would complicate the study of the effect of the metal or ligand on the refractive index.

### 2.5.2 Structure and Characterization of 1,5-naphthalenedisulfonate CPs

The disodium salt which is colorless and crystalline is a commercially available source of the 1,5-naphthalenedisulfonate anion ( $1,5\text{-nda}^{2-}$ ) and is the starting point

of the study into this particular ligand. The disodium salt was recrystallized out of water. The structure of  $\text{Na}_2(1,5\text{-nda})\text{H}_2\text{O}$  (Figure 2.11.) contains repeating sodium and 1,5-nda units. The coordination about Na is distorted trigonal bipyramidal, with coordination to a sulfonate of  $1,5\text{-nda}^{2-}$  and a bridging water molecule in the axial positions. In the equatorial positions, coordination to two sulfonates and another bridging water is seen. The naphthalene backbone of 1,5-nda is stacked through  $\pi$ - $\pi$  interactions in a staggered arrangement extending through three-dimensions. The index of  $\text{Na}_2(1,5\text{-nda})\text{H}_2\text{O}$  was measured to be 1.60.

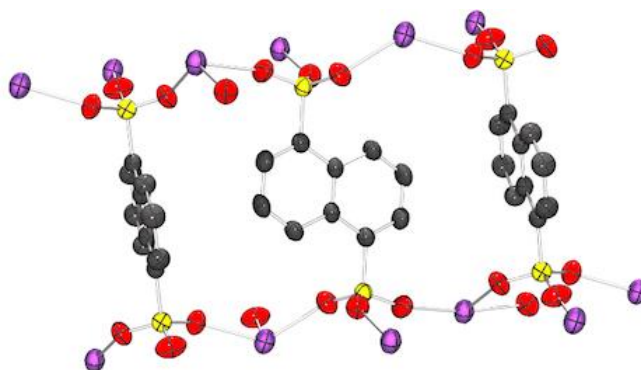


Figure 2.11. Extended structure of  $\text{Na}_2(1,5\text{-nda})\text{H}_2\text{O}$  with 80% probability thermal ellipsoids. Colour scheme: Na, purple; C, grey; S, yellow; O, red; H, omitted for clarity.

Simple cation-metathesis of the disodium salt was carried out in lead perchlorate in water, yielding  $\text{Pb}(1,5\text{-nda})(\text{H}_2\text{O})_3$ . Similar to  $\text{Na}_2(1,5\text{-nda})\text{H}_2\text{O}$ ,  $\text{Pb}(1,5\text{-nda})(\text{H}_2\text{O})_3$ , which is also colorless and crystalline (Figure 2.12.) contains chains of repeating lead and  $1,5\text{-nda}^{2-}$  units extending in three dimensions. The coordination geometry about lead adopts a distorted pentagonal bipyramidal geometry with three or four equivalents of ligated water and sulfonate functionalities from  $1,5\text{-nda}^{2-}$  respectively. The naphthalene backbone in this lead CP also stacks through  $\pi$ - $\pi$  interactions in a herringbone arrangement. The refractive index of  $\text{Pb}(1,5\text{-nda})(\text{H}_2\text{O})_3$  was measured to be 1.60, identical to that of  $\text{Na}_2(1,5\text{-nda})\text{H}_2\text{O}$ .

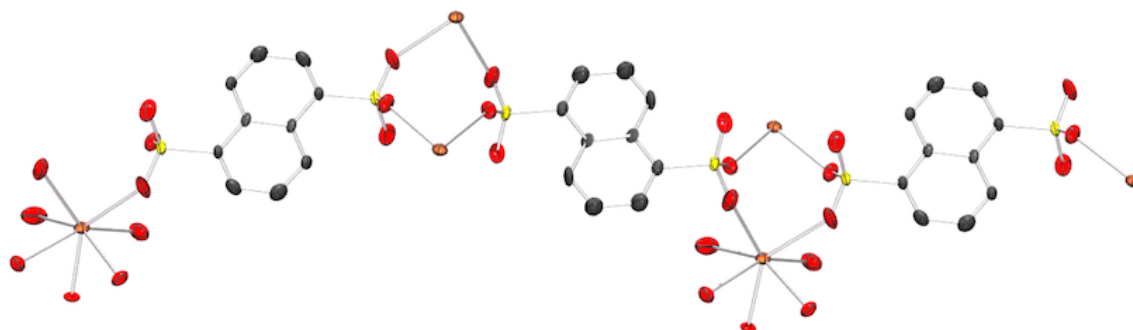


Figure 2.12. Extended structure of  $\text{Pb}(1,5\text{-nda})(\text{H}_2\text{O})_3$  with 80% probability thermal ellipsoids. Colour scheme: Pb, orange; C, grey; S, yellow; O, red; H and ligated waters, omitted for clarity.

### 2.5.3 Structure and Characterization of 5-Mercapto-3-phenyl-1,3,4-thiodiazole-2(3H)-thione CPs

To assess the impact of lower valent sulfur atoms, 5-Mercapto-3-phenyl-1,3,4-thiodiazole-2(3H)-thione was used as the next ligand. For clarity purposes, the anionic ligand,  $\text{C}_8\text{H}_5\text{N}_2\text{S}_3^-$ , will from this point be referred to by its commercial name of *bismuthiol II*.

The monopotassium salt, a beige powder, is a commercially available source of *bismuthiol II*; we recrystallized this salt to generate X-ray quality crystals. The structure of  $\text{K}(\text{bismuthiol II})\text{H}_2\text{O}$  (Figure 2.13.) contains chains of alternating potassium and *bismuthiol II* units extending in a zig-zag along one-dimension. The coordination geometry about potassium adopts a distorted octahedron with coordination to four equivalents of *bismuthiol II* and two equivalents of water that bridge potassium atoms. The phenyl moiety and cyclic core of *bismuthiol II* exhibit stacking through  $\pi$ - $\pi$  interactions.  $\text{K}(\text{bismuthiol II})\text{H}_2\text{O}$  has a measured index of 1.78. Again, a cation-metathesis was carried out replacing potassium with the more polarizable zinc and lead yielding  $\text{Zn}(\text{bismuthiol II})_2$  and  $\text{Pb}(\text{bismuthiol II})_2$  respectively. The potassium, zinc, and lead CPs,  $\text{KC}_8\text{H}_5\text{N}_2\text{S}_3(\text{H}_2\text{O})$ ,  $\text{ZnC}_{16}\text{H}_{10}\text{N}_4\text{S}_6$ , and  $\text{PbC}_{16}\text{H}_{10}\text{N}_4\text{S}_6$  respectively, provided crystals of sufficient quality for structural determination.

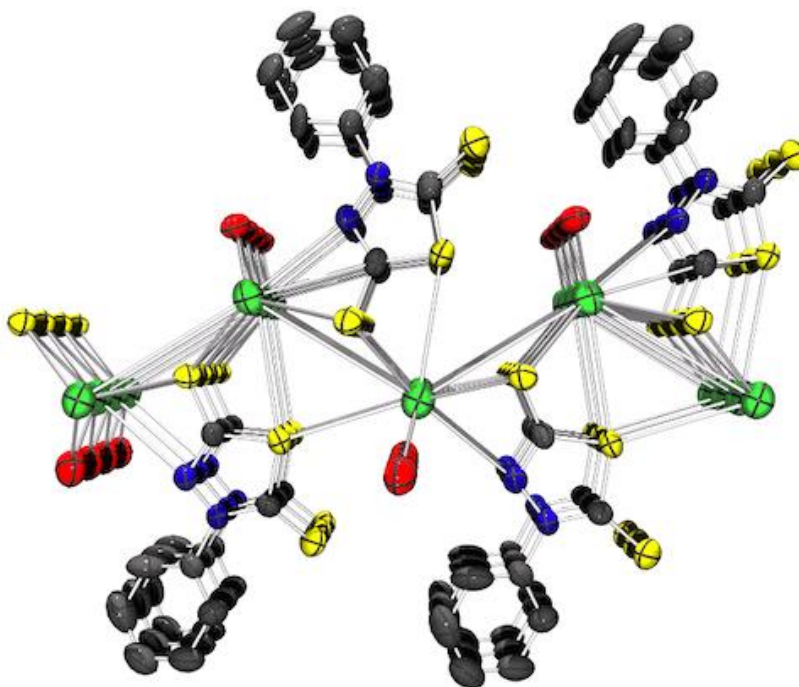


Figure 2.13. Extended structure of  $\text{K}(\text{bismuthiol II})\text{H}_2\text{O}$  with 80% probability thermal ellipsoids. Colour scheme: K, green; C, grey; N, blue; S, yellow; H, white.

The structure of  $\text{Zn}(\text{bismuthiol II})_2$ , an off-white powder, (Figure 2.14.) contains interpenetrating chains of alternating zinc and *bismuthiol II* units extending in two-dimensions. The coordination geometry about zinc is tetrahedral with coordination to four equivalents of bismuthiol II through two thione and two thiolate functionalities on the ligand.  $\text{Zn}(\text{bismuthiol II})_2$  has a measured refractive index of 1.77.

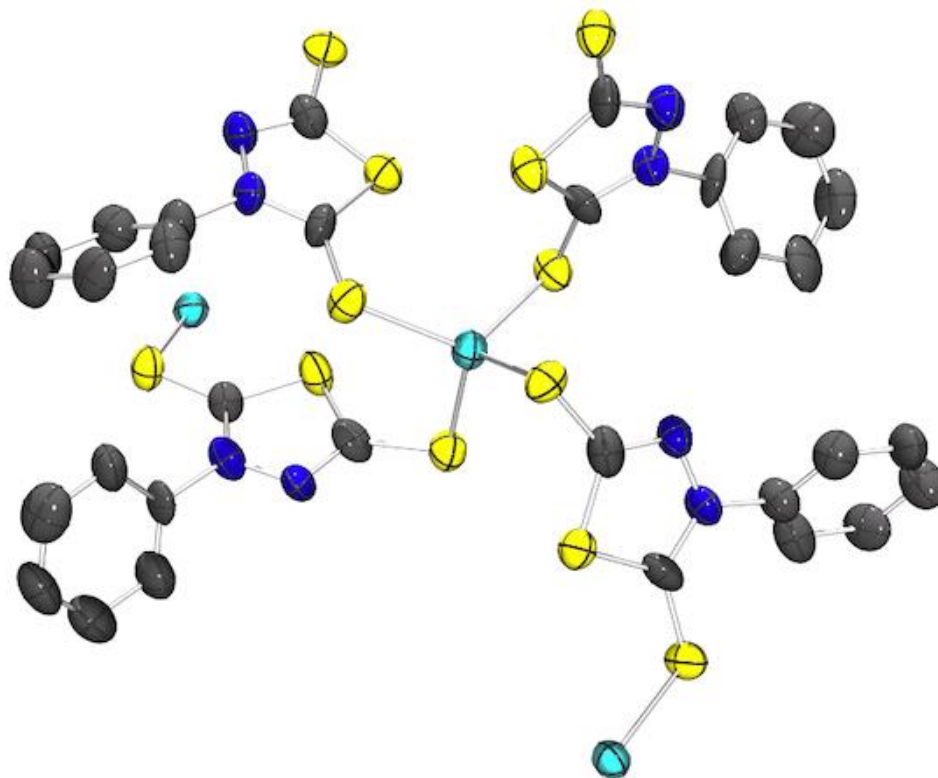


Figure 2.14. Extended structure of  $\text{Zn}(\text{bismuthiol II})_2$  with 80% probability thermal ellipsoids. Colour scheme: Zn, cyan; C, grey; N, blue; S, yellow; H, white.

The structure of  $\text{Pb}(\text{bismuthiol II})_2$ , a light yellow powder, (Figure 2.15.) involves interpenetrating chains of alternating lead and bismuthiol II units extending in two-dimensions. The coordination geometry about the lead adopts a seesaw geometry with the presence of a stereochemically active lone pair. Each lead node is coordinated to four equivalents of bismuthiol II through two thione and two thiolate functionalities on the ligand.  $\text{Pb}(\text{bismuthiol II})_2$  has a measured refractive index of 1.83.

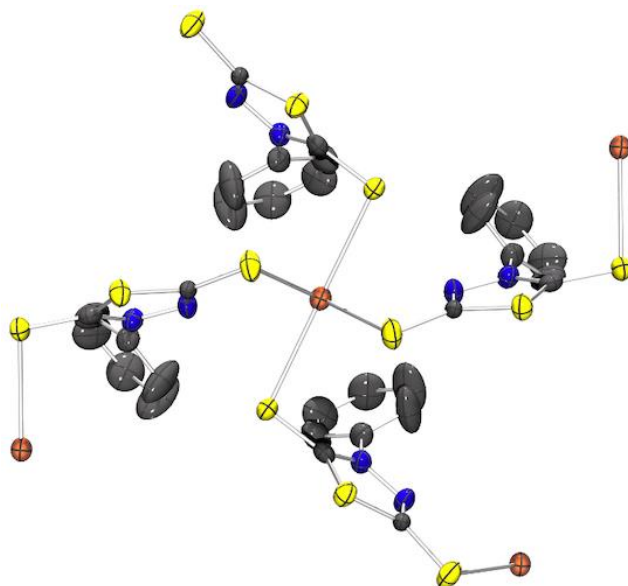


Figure 2.15. Extended structure of  $\text{Pb}(\text{bismuthiol II})_2$  with 80% probability thermal ellipsoids. Colour scheme: Pb, orange; C, grey; N, blue; S, yellow; H, omitted for clarity.

#### 2.5.4 Structure and Characterization of 1,3,4-Thiadiazole-2,5-dithiol CPs

Bismuthiol I was investigated as a ligand to assess the effect of changing the molecular volume on the refractive index. The structure of  $\text{K}_2(\text{bismuthiol I})$ , a brown powder, (Figure 2.16.) contains chains of repeating bismuthiolate and potassium units extending in three-dimensions. The coordination geometry about potassium adopts a pentagonal bipyramidal geometry with coordination to five thiolate and two secondary amine functionalities from the heterocycle from neighbouring bismuthiol units. Staggered chains of bismuthiol units are oriented anti-parallel to neighbouring chains.  $\text{K}_2(\text{bismuthiol I})$  has a measured refractive index of 1.68. In an attempt to enhance the RI, a cation-metathesis was carried out, replacing potassium with the more polarizable zinc and lead, yielding  $\text{Zn}(\text{bismuthiol I}+\text{H})_2$  and  $\text{Pb}(\text{bismuthiol I})$  respectively.

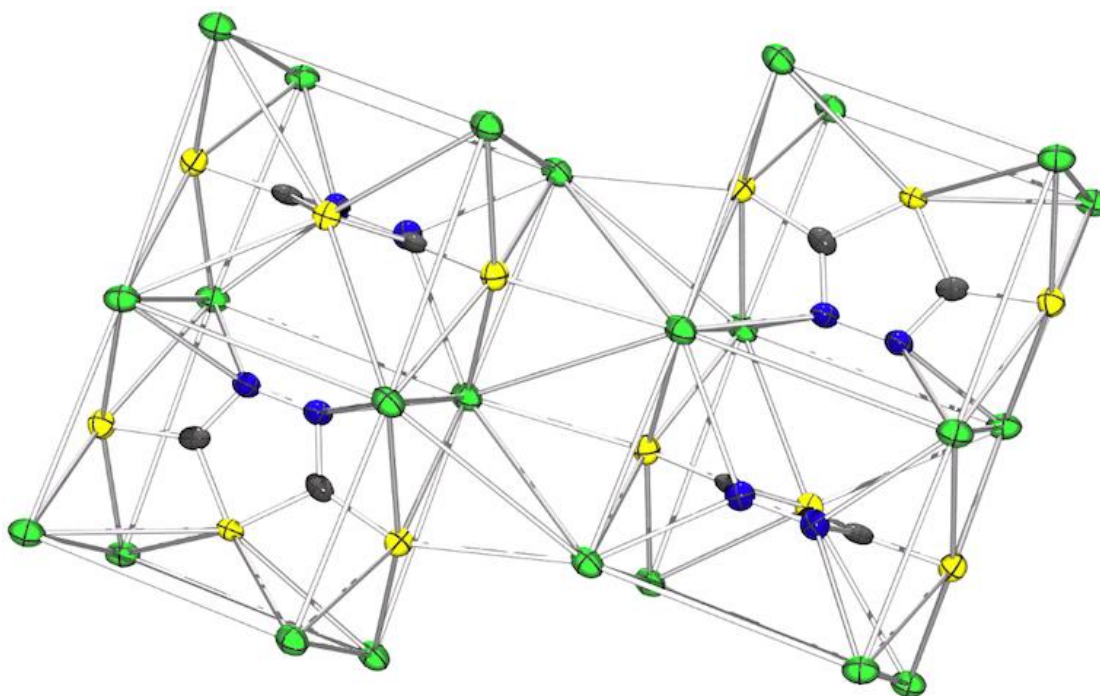


Figure 2.16. Extended structure of  $K_2(\text{bismuthiol I})$  with 80% probability thermal ellipsoids. Colour scheme: K, green; C, grey; N, blue; S, yellow.

The potassium and zinc CPs,  $K_2C_2N_2S_3(H_2O)_{0.5}$  and  $ZnC_4N_4S_6H_2$  respectively, provided crystals of sufficient quality for structural determination.

The structure of  $Zn(\text{bismuthiol I}+H)_2$ , a white powder, (Figure 2.17.) contains interpenetrating chains of alternating zinc and bismuthiol I units extending in three-dimensions. In the solid state, the bismuthiol I ligand is observed to undergo protonation at the N1 position. This results in the breaking of symmetry of the ligand with both thione and thiolate functionalities present on the building block. Each zinc node possesses a tetrahedral coordination geometry coordinated to four equivalents of bismuthiol I through two thione and two thiolate functionalities.  $Zn(\text{bismuthiol I}+H)_2$  has a measured index of 1.72.

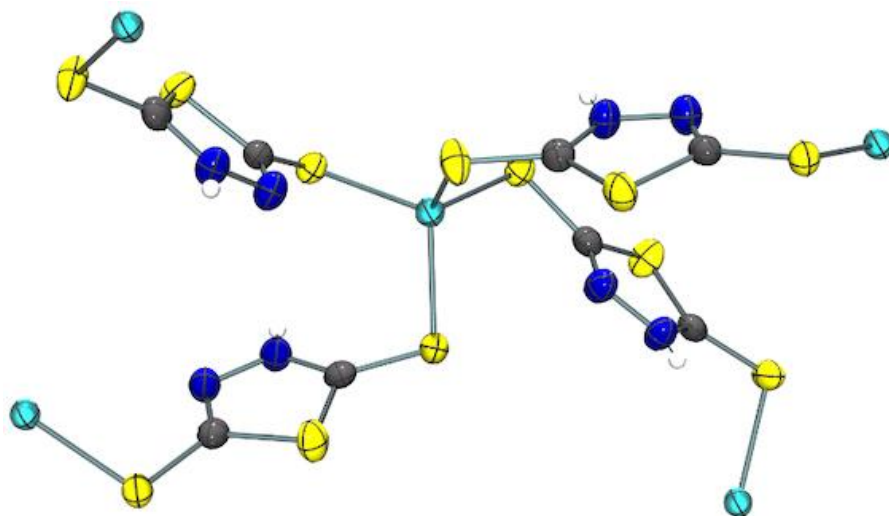


Figure 2.17. Extended structure of  $\text{Zn}(\text{bismuthiol I}+\text{H})_2$  with 80% probability thermal ellipsoids. Colour scheme: Zn, cyan; C, grey; N, blue; S, yellow; H atoms, omitted for clarity.

Attempts to recrystallize  $\text{Pb}(\text{bismuthiol I})$ , a yellow powder, have thus far been unsuccessful.  $\text{Pb}(\text{bismuthiol I})$  was measured to have a very high, refractive index of 2.25, which rivals the RIs of materials that can be produced through the other aforementioned routes of HRIPs and nanocomposites.

### 2.5.5 Discussion

The CPs containing the  $1,5\text{-nda}^{2-}$  ligand possess respectable refractive indices but they are not overly impressive, especially for  $\text{Pb}(1,5\text{-nda})(\text{H}_2\text{O})_3$  considering the presence of the high  $\alpha/V$  lead atom. The factors working against this ligand in achieving a higher refractive index polymer are (1) the high  $V$  of the naphthalene and (2) the high oxidation states (+4) of the sulphur, which diminishes  $\alpha$ . Structural characterization of the  $\text{Mn}(\text{III})$  and  $\text{Ni}(\text{II})$  –  $1,5\text{-nda}$  CPs was not successful but the lower index of the Mn-CP is most likely due to the higher ionic charge of the metal, leading to the greatest ratio (3:2) between the ligand and metal which would depress the index for the reasons described above in section 2.2.

The goal in identifying the second candidate ligand was to find something that has a qualitatively high  $V$  but lower oxidation states of sulfur. The impact of increasing



$\alpha$ , through the reduction of oxidation states, on the index can be assessed this way. *Bismuthiol II*, a heterocyclic monoanion with a phenyl substituent on one of its nitrogen atoms, thiolate, and thione functionalities was selected in attempt to isolate the effect of  $\alpha$ . This anion possesses sulfur in a low valent (-2) state compared to 1,5-nda. Consistent with this, it was observed that *bismuthiol II*-based CPs have higher refractive indices than the aforementioned 1,5-nda based materials.

The potassium CP  $K(bismuthiol II) \cdot H_2O$  has a refractive index of 1.78 compared to 1.60 seen for  $Na_2(1,5-nda)H_2O$ . This increase in refractive index can be qualitatively attributed to the increased contribution from the ligand relative to the metal; there is a 1:1 ratio between K and *bismuthiol II* in  $K(bismuthiol II) \cdot H_2O$  whereas there is a 2:1 ratio between Na and 1,5-nda in  $Na_2(1,5-nda)H_2O$ . The  $Zn^{2+}$  and  $Pb^{2+}$  CPs of this ligand,  $Zn(bismuthiol II)_2$  and  $Pb(bismuthiol II)_2$  also have relatively high refractive indices of 1.77 and 1.88 respectively. The Mn(III) and Ni(II)-*bismuthiol II* CPs were not structurally characterized but possessed refractive indices of 1.58 and 1.62 respectively, both an increase over the Mn(III) and Ni(II)-1,5-nda CPs. This is presumably due to the increased polarizability of the *bismuthiol II* ligand with lower oxidation states than 1,5-nda based CPs.

A similar heterocyclic anionic building block, *Bismuthiol I*, was chosen to isolate for the effect that decreasing  $V$  has on the index of the CP. *Bismuthiol I* is structurally similar to *Bismuthiol II* with the differences being (a) lack of phenyl substituent and (b) two thiolate functionalities instead of one thiolate and one thione.

This ligand has the highest  $\alpha/V$  of the three used for this study and as such would be expected to yield the highest refractive index CPs.  $K_2(bismuthiol I)$  was measured to have an index of 1.68. Metathesis to Zn and Pb produced  $Zn(bismuthiol I + H)_2$  and  $Pb(bismuthiol I)$ , which have refractive indices of 1.72 and 2.25 respectively. High refractive indices were also observed for the *Bismuthiol I*-CPs where structural determination was not possible. The Cu(II) and Co(II) CPs exhibited refractive indices of 1.97 and 2.10, which is promising for application

purposes since they involve the use of more benign metals compared to lead. The observations seen of *bismuthiol I*-based CPs reinforce the importance of not just polarizability in producing high RI materials but also the need to have this polarizability to be concentrated.

A computational analysis was performed by Carson Zellman from the Williams group at Simon Fraser University to assess whether an *a priori* approach to designing high index-CPs and tailoring them to certain indices through choice of metals and ligands was possible. Calibration curves were generated relating the  $\alpha/V$  to RI for both a group of representative ligands and metals and from these a predictive index based on the relative contributions of each in the CP can be produced. The  $\alpha/V$  was determined with DFT using the Becke three parameter Lee-Yang Parr method at the 3-21G\* level. The validity of this calibration was assessed against the empirically determined indices for eight CPs in this study. The results are summarized in Table 2.4.

Table 2.4. Summary of Empirical and Predicted Indices

<b>CP</b>	<b>Empirical</b>	<b>Predicted</b>	<b>Deviation</b>
$\text{Na}_2(1,5\text{-nda})(\text{H}_2\text{O})$	1.60	1.60	-
$\text{Pb}(1,5\text{-nda})(\text{H}_2\text{O})_3$	1.60	1.87	0.27
$\text{K}(\text{bismuthiol II})\text{H}_2\text{O}$	1.78	1.72	-0.06
$\text{Zn}(\text{bismuthiol II})_2$	1.77	1.71	-0.06
$\text{Pb}(\text{bismuthiol II})_2$	1.88	1.91	0.03
$\text{K}_2(\text{bismuthiol I})(\text{H}_2\text{O})_{0.5}$	1.68	1.76	0.08
$\text{Zn}(\text{bismuthiol I}+\text{H})_2$	1.72	1.66	-0.06
$\text{Pb}(\text{bismuthiol I})$	2.25	2.23	-0.02

One key structural feature that was left out in the making of the calibration curve for the ligand set is hydrogen bonding. It was noticed during the calculations that compounds capable of hydrogen bonding worsened the linear relationship. Upon

analysis, it was realized that the packing efficiency of these compounds was not considered; when compared to the empirical density, the calculated density was much lower than the observed density. The density is proportional to the RI but the  $\alpha/V$  is calculated on a single molecule and thus does not consider the extended packing. As such, the calibration for the ligands systematically underestimates the index of hydrogen bonded compounds; this underestimation is particularly evident for molecules with multiple hydrogen bonding sites. For these reasons, the entire ligand data set incorporated in the calibration does not include compounds that have functionalities capable of hydrogen bonding. The final calibration curve for the ligands is displayed in Figure 2.18. This calibration accounts for the ligands as distinct entities and does not consider the situation within a polymer.

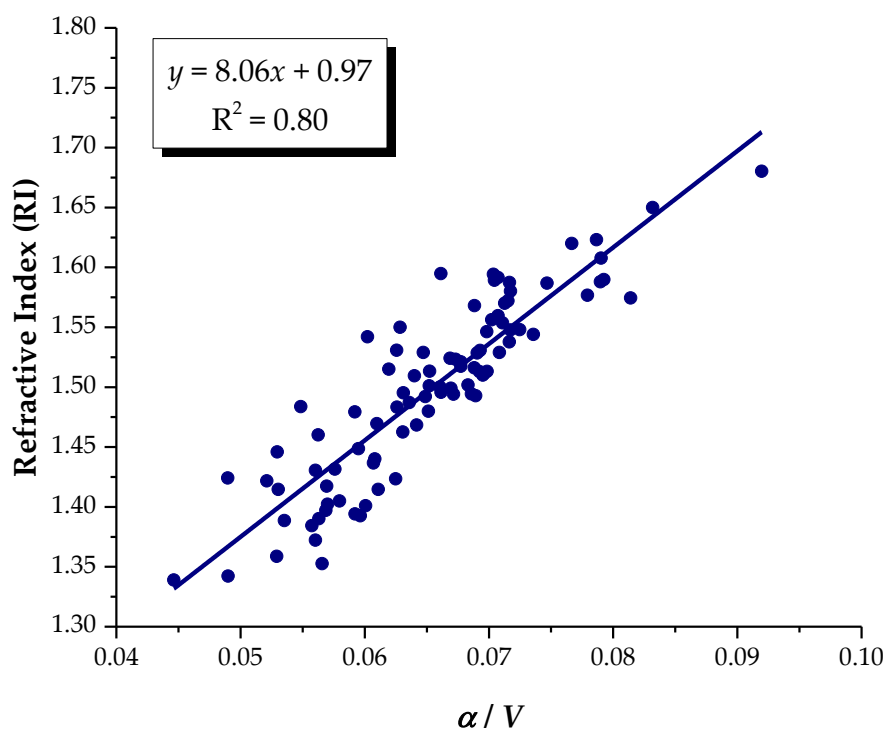


Figure 2.18. Calibration relating  $\alpha/V$  to the refractive index

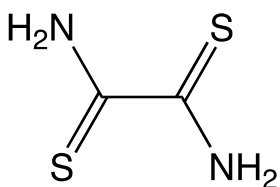
There is a significant negative deviation between the empirically determined and predicted indices for  $\text{Pb}(1,5\text{-nda})(\text{H}_2\text{O})_3$ . This can be attributed to electronic

repulsion from the stereochemically active lone pair of lead, which may effect a lower packing density that is not accounted for in the model. Additionally, the presence of a large number of ligated waters increases the margin of error. The other significant deviation is seen for  $K_2(\text{bismuthiol I})(\text{H}_2\text{O})_{0.5}$ . This can be explained by the fact that the material is very hygroscopic and hence likely absorbed water by the time the refractive index was measured. The addition of water into the sample is expected to decrease the refractive index and thus why the predicted value is larger than the actual measured value. The rest of the results show good agreement with the predictive methods and the experimentally determined results.

### 2.5.5 Attempts to Make CPs Using Other Building Blocks

Two other ligands that were identified as being potential candidates for producing high RI materials are discussed below. These were chosen for their high polarizability, low volume, and presence of possible binding sites allowing coordination to metals.

#### Dithiooxamide (i.e. rubeanic acid)

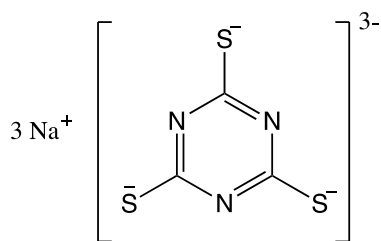


Dithiooxamide was briefly explored as a candidate building block for making refractive CPs. It was considered attractive for this purpose due to the presence of low valent atoms (S & N) and  $\pi$ -electron density in the C=S bond, as well as a small volume. The presence of lone pairs on the molecule would also allow it to function as either a neutral ligand or an anionic one, if the amide groups were to be deprotonated during coordination polymer synthesis.

Dithiooxamide, a fine brown powder, was dissolved in either water or methanol and added to solutions of metal salts, including zinc nitrate, manganese(III) chloride, indium(III) chloride, and lead perchlorate. Dithiooxamide was assumed to be mono-anionic when deciding stoichiometric ratios between the ligand and metal salt (e.g. two equivalents with one equivalent of lead(II) nitrate). Upon addition of

the two components, powders of dark colours ranging from beige-brown for zinc and black for lead precipitated out immediately. Triethylamine was used in subsequent trials in an attempt to deprotonate the ligand. These materials were not pursued further due to the lack of transparency at visible wavelengths and the inability to produce a crystalline sample for structural analysis.

### Trithiocyanuric acid (trisodium salt)



This heterocyclic building block was also identified as a candidate ligand for making a highly refractive CP. It was predicted to have a high electronic polarizability arising from low valent atoms (S & N) and  $\pi$ -electron density in

the ring. It is also a tri-anion which would make it amenable toward CP synthesis. This ligand was reacted with a variety of metal salts including zinc nitrate, manganese (III) chloride, indium (III) chloride, barium nitrate, magnesium nitrate, and lead perchlorate under hydrothermal conditions producing amorphous powders. The manganese product had a green, algae-like appearance; the indium product, an orange powder; the lead product, a jet-black powder. All other materials were white powders. These reactions were low-yielding and attempts at crystallization failed so the products were not pursued further.

Other ligands to investigate include sulphur based dithiocarbamates, dithiocarboxylates and xanthates. The objective is to find building blocks that would lead to products with high electron density. Greater studies into finding the crystallization conditions of trithiocyanuric acid and dithiooxamide should also be carried out.

### 2.5.6 Conclusions

Coordination polymers were explored as a novel way to access high-index materials. The design principles, mainly high  $\alpha/V$ , used to make intrinsic-HRIPs

and nanocomposite-HRIPs were applied to CPs. A survey of eight CPs derived from three polarizable anionic building blocks, (1) 1,5-naphthalenedisulfonate, (2) 5-mercapto-3-phenyl-1,3,4-thiadiazole-2(3H)-thione, and (3) 2,5-dimercapto-1,3,4-thiadiazole were synthesized and characterized in attempt to validate the use of CPs as a new route towards high-index materials. The results indicate that the  $\alpha/V$  shows a strong correlation to the RI. Computational analysis was performed to produce a calibration relating the  $\alpha/V$  to RI for both the metals and ligands in a CP. Such a tool can potentially allow the prospect of tunable RI CPs. The validity of the calibration was assessed by comparing against the empirically determined RIs of the eight CPs in the survey set. Good agreement was seen for all but two examples, which thereby validates the computational method as a reasonable predictive tool. Moreover, one of the materials produced,  $\text{Pb}(\text{bismuthiol I})$ , has an index of 2.25, which is competitive with the upper ceilings seen in intrinsic HRIPs and nanocomposite-HRIPs. These findings pave the way toward harnessing the robust and modular nature of CP synthesis to study a largely neglected property in this field of study, the refractive index.

High refractive index medium are desirable for use in some device fabrications. However, the refractive index is but one design consideration. Other considerations that come up when making devices include transparency, dispersion, and birefringence. High transparency, especially at the frequencies of interest, are desirable since absorption leads to optical loss. The dispersion of a material describes the dependency of the refractive index on wavelength. One metric that quantifies dispersion is the Abbe number, named after the German physicist Ernst Abbe (1840-1905). High Abbe numbers indicate low dispersion.

$$V_D = \frac{n_D - 1}{n_F - n_C}$$

where  $n_D$ ,  $n_F$ , and  $n_C$  are the indices of the material at various spectral lines of 589.3, 486.1, and 656.3 nm respectively. Materials with high Abbe numbers are ideal for applications in lenses because highly dispersive, low Abbe number materials, suffer greater chromatic aberration.<sup>110</sup> Birefringence is an optical

property that describes the difference in refractive indices along different crystallographic axes. Birefringent materials may be useful for one application but not good for others. High birefringence materials degrade the performance of optical devices that require focusing of light<sup>151</sup> but are useful in applications that require the modulation of the polarization of light such as in the components of devices used in the telecommunications industry. A brief look into birefringent materials follows in 2.6.

## **2.6 A Brief Adventure Into the World of Birefringence**

### **2.6.1 Background and Motivations**

A property intimately related to the refractive index is the birefringence, which is a measure of the differential in the refractive index along different crystallographic planes. These differences arise from the polarizability being anisotropic or directionally dependent. This contrasts with an isotropic medium, in which the polarizability is directionally independent and the refractive index is the same in all planes. Gases, liquids, and some amorphous solids like glasses are isotropic but crystalline materials are more often anisotropic.

The unit cell of a crystal defines the smallest volume which contains the symmetry operators which if extended can produce the macroscopic crystal. The unit cell has three axes *a*, *b*, and *c*. Classification of external symmetry led to the derivation of seven crystal systems (Table 2.5.). From analysis of the parameters of the crystal systems, we see that cubic systems would be isotropic since all of the axes are identical and would have the same refractive index. In contrast, all other crystal systems are anisotropic with the refractive index being directionally dependent. For instance, orthorhombic crystal systems will have a different index for each of the three crystallographic axes. The highest refractive index axis is referred to as the *slow axis* whereas the lowest refractive index axis is the *fast axis*. Numerically, the birefringence is the difference between the refractive index of the fast and slow axis.

Table 2.5. Crystal Systems

Crystal System	Unit Cell
Triclinic	$a \neq b \neq c; \alpha \neq \beta \neq \gamma \neq 90^\circ$
Monoclinic	$a \neq b \neq c; \alpha = \gamma = 90^\circ \neq \beta$
Hexagonal	$a = b \neq c; \alpha = \beta = 90^\circ, \gamma = 120^\circ$
Rhombohedral	$a = b = c; \alpha = \beta = \gamma \neq 90^\circ$
Orthorhombic	$a \neq b \neq c; \alpha = \beta = \gamma = 90^\circ$
Tetragonal	$a = b \neq c; \alpha = \beta = \gamma = 90^\circ$
Cubic	$a = b = c; \alpha = \beta = \gamma = 90^\circ$

The rational design criteria for making birefringent materials involves incorporation of molecules with highly anisotropic polarizability and orienting them in a fashion that yields an additive effect. Birefringent media are desirable for many optical applications, chiefly those that require the splitting of light, and have found use in applications as optical filters,<sup>152,153</sup> phase matching,<sup>154,155</sup> and optical wave-plates to form circularly polarized light.<sup>31,156</sup>

In this section, compounds and CPs made of two anisotropic ligands 2,2';6'2'-terpyridine (terpy) and 2,6-bis(benzimidiazol-2-yl)pyridine (bbp) are investigated.<sup>157</sup>

### 2.6.2 Synthesis and Characterization of 2,2';6'2'-terpyridine and 2,6-bis(benzimidiazol-2-yl)pyridine Compounds and Polymers

The materials discussed in this section have been published in Guan, D.; Thompson, J. R.; Leznoff, D. B. *Can. J. Chem.* **2018**, 96 (2), 226–234.

The metal coordination geometries for  $\text{Hg}(\text{L})(\text{CN})_2$  (L = terpy, bbp) are illustrated in Fig. 2.18. The coordination spheres of Hg(II) in these complexes adopt a very distorted trigonal bipyramid with a tridentate terpy or bbp ligand in the equatorial plane and two axial cyanide ligands. The Lewis acidic properties of Hg(II) allows it



to coordinate to Lewis basic ligands and can adopt coordination geometries ranging from linear to octahedral. Molecules of  $\text{Hg}(\text{terpy})(\text{CN})_2$  and  $\text{Hg}(\text{bbp})(\text{CN})_2$  stack through  $\pi$ - $\pi$  interactions (3.34 and 3.46 Å respectively, measured plane to plane), forming an extended structure highlighted in Figure 2.19. where all the terpy and bbp ligands are co-planar. Terpy and bbp are structurally similar and often generate isostructural complexes.

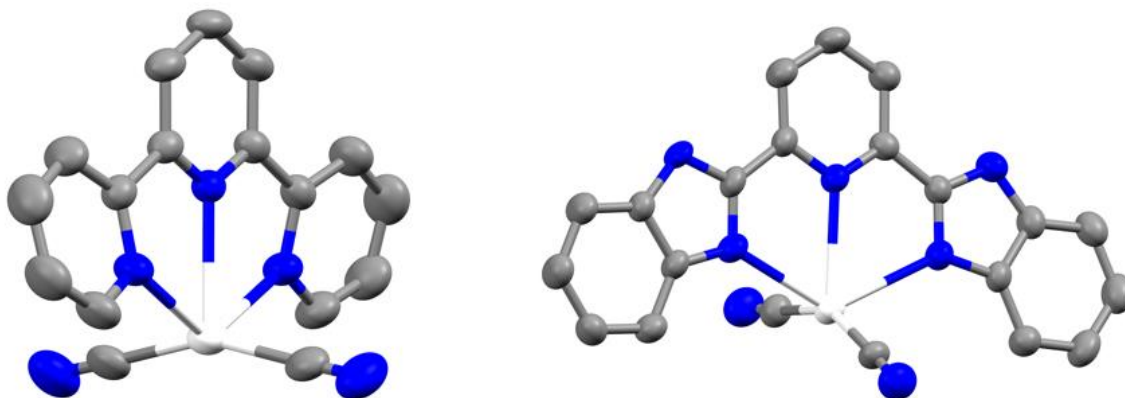


Figure 2.19. Molecular structure of (left)  $\text{Hg}(\text{terpy})(\text{CN})_2$  and (right)  $\text{Hg}(\text{bbpb})(\text{CN})_2$  with 50% probability thermal ellipsoids. Color scheme: Hg, white; C, grey; N, blue; H atoms, omitted for clarity.

### Birefringence of $\text{Hg}(\text{terpy})(\text{CN})_2$

Crystals of  $\text{Hg}(\text{terpy})(\text{CN})_2$  have monoclinic symmetry and grow as plates perpendicular to the (100) face (Figure 2.20.). The birefringence measured down this face is 0.37(2), over double the 0.17 of calcite. A view of this face shows terpy ligands stacked parallel in an ordered structure; however, it also shows an incline of the terpy ligands as a result of a  $36^\circ$  angle between the terpy plane and the viewing direction. This deviation from the edge-on view results in a decrease in polarizability anisotropy. As such, the birefringence of 0.37(2) is only a fraction of the maximum possible for this compound.

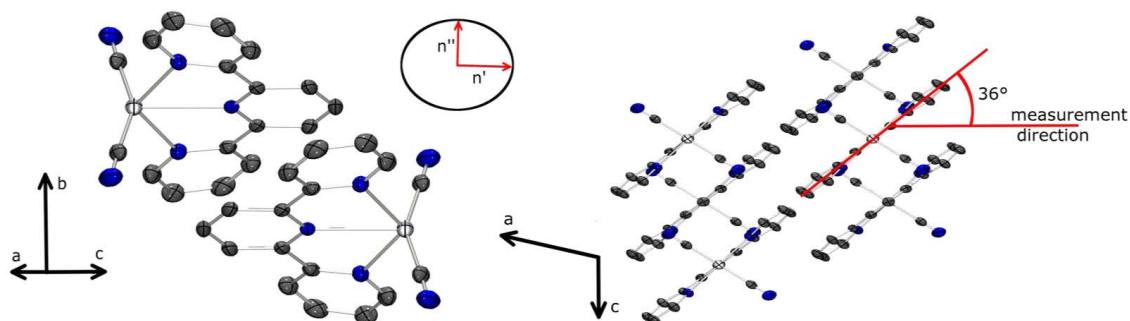


Figure 2.20. View normal to primary crystallographic face of  $\text{Hg(terpy)(CN)}_2$  (Left) View normal to primary crystallographic face (100) of  $\text{Hg(terpy)(CN)}_2$  displaying  $\pi$ -stacking interactions and (Right) down the crystallographic b-axis. Color scheme: Hg, white; C, grey; N, blue; H atoms, omitted for clarity.

### Birefringence of $\text{Hg(bbp)(CN)}_2$

Crystals of  $\text{Hg(bbp)(CN)}_2$  have triclinic symmetry and grow as plates perpendicular to the (010) face, and have a birefringence of 0.45(2). In this case, a view of the available crystal face shows bbp ligands edge-on in a well-ordered array parallel to one another (Figure 2.21.). The significant increase in birefringence compared to the terpy version can likely be attributed to the combination of anisotropic structure and edge-on view. However, this case does not represent the highest value for the crystal as the measurement contains the highest polarizability tensor of bbp (the longest axis) and, therefore, is a measurement of the intermediate and smallest (perpendicular to the plane) polarizability tensors.

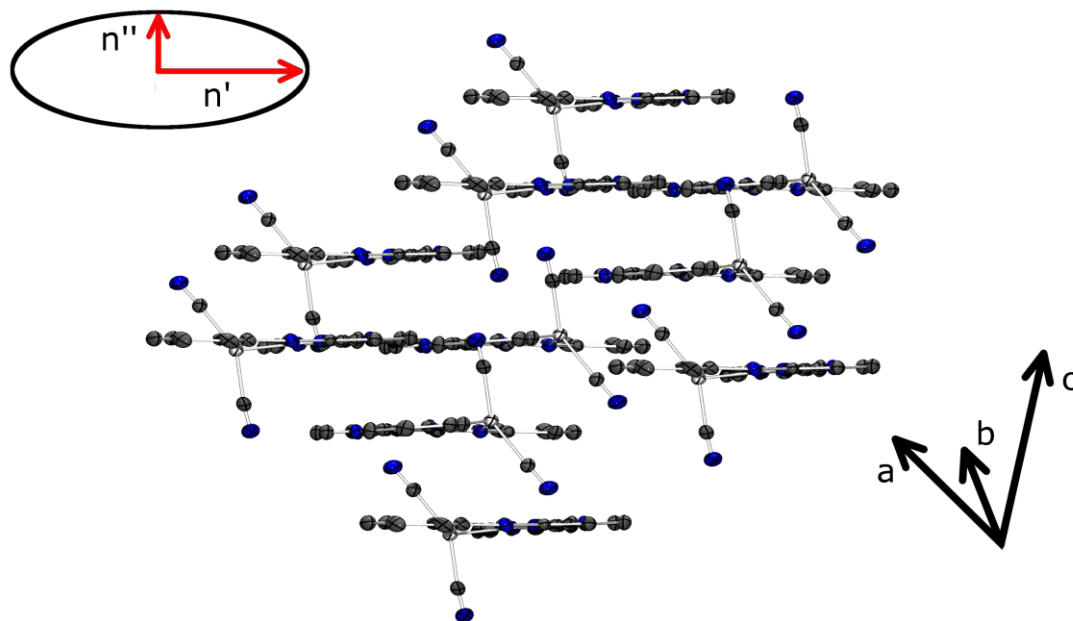


Figure 2.21. View normal to the primary crystallographic face (010) of  $\text{Hg}(\text{bbp})(\text{CN})_2$ . Color scheme: Hg, white; C, grey; N, blue; H atoms, omitted for clarity.

The structure of  $\text{Pb}(\text{terpy})\text{Cl}_2[\text{Hg}(\text{CN})_2]_{0.5}$  contains a seven-coordinate Pb(II) centre with a distorted pentagonal bipyramidal geometry (Figure 2.22, bottom). The tridentate terpy and N-cyano ligands from the  $\text{Hg}(\text{CN})_2$  linkers of the neighbouring Pb(II) centre complete the equatorial plane. Two chloride ligands occupy the axial positions. Geometric distortions consistent with the presence of a stereochemically active lone pair occupying an equatorial site in the coordination sphere was noted. The supramolecular structure of  $\text{Pb}(\text{terpy})\text{Cl}_2[\text{Hg}(\text{CN})_2]_{0.5}$  forms a coordination polymer bridged by  $\text{Hg}(\text{CN})_2$ . Each chain connections to an adjacent one through the N-cyano linkage.

The structure of  $\text{Pb}(\text{terpy})\text{Br}_2[\text{Hg}(\text{CN})_2]_{0.5}$  is comparable with that of  $\text{Pb}(\text{terpy})\text{Cl}_2[\text{Hg}(\text{CN})_2]_{0.5}$ .  $\text{Hg}(\text{CN})_2$  units bridge  $\text{Pb}(\text{terpy})\text{Br}_2$  units and an axial bromide of one Pb(II) chain forms a long equatorial bond, 3.509(2) Å, to a Pb(II) centre on an adjacent chain (Figure 2.22, top). Two bromide ligands occupy the axial position and the tridentate terpy completes the equatorial plane.

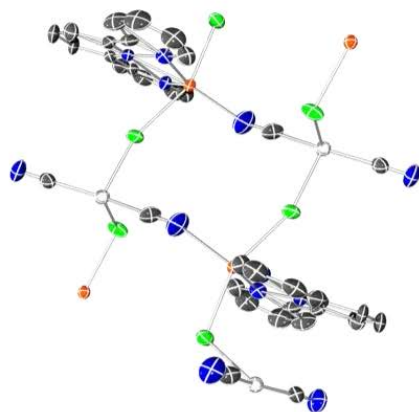
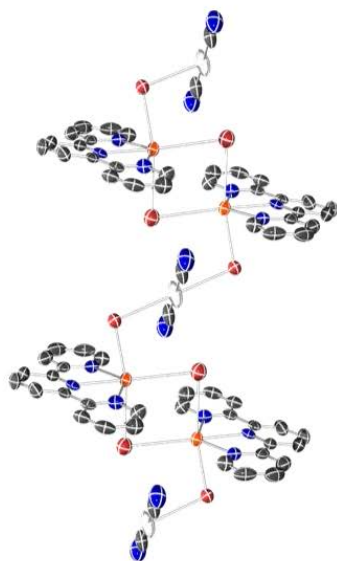


Figure 2.22. Extended network of (top)  $\text{Pb(terpy)Br}_2[\text{Hg(CN)}_2]_{0.5}$  and (bottom)  $\text{Pb(terpy)Cl}_2[\text{Hg(CN)}_2]_{0.5}$ . Color scheme: Pb, orange; Hg, white; C, grey; N, blue; Cl, green; Br, red; H atoms, omitted for clarity.

### Birefringence of $\text{Pb(terpy)Cl}_2[\text{Hg(CN)}_2]_{0.5}$

Crystals of  $\text{Pb(terpy)Cl}_2[\text{Hg(CN)}_2]_{0.5}$  are also monoclinic but grow as plates perpendicular to the (101) face (Figure 2.23.). The  $\Delta n$  of 0.407(11) for this face is similar to the previous bromide example with the bbp ligands edge-on and the measurement approximately aligned with the central Pb-pyridine bond. In this case, the axial positions contain less polarizable Pb-Cl and Hg-Cl bonds, leading to a greater polarizability anisotropy compared with the previous case and therefore a slightly higher  $\Delta n$ . However, the terpy ligands are not parallel to one another; rather, they have a  $14^\circ$  angle between them, leading to lower anisotropy in the terpy component.

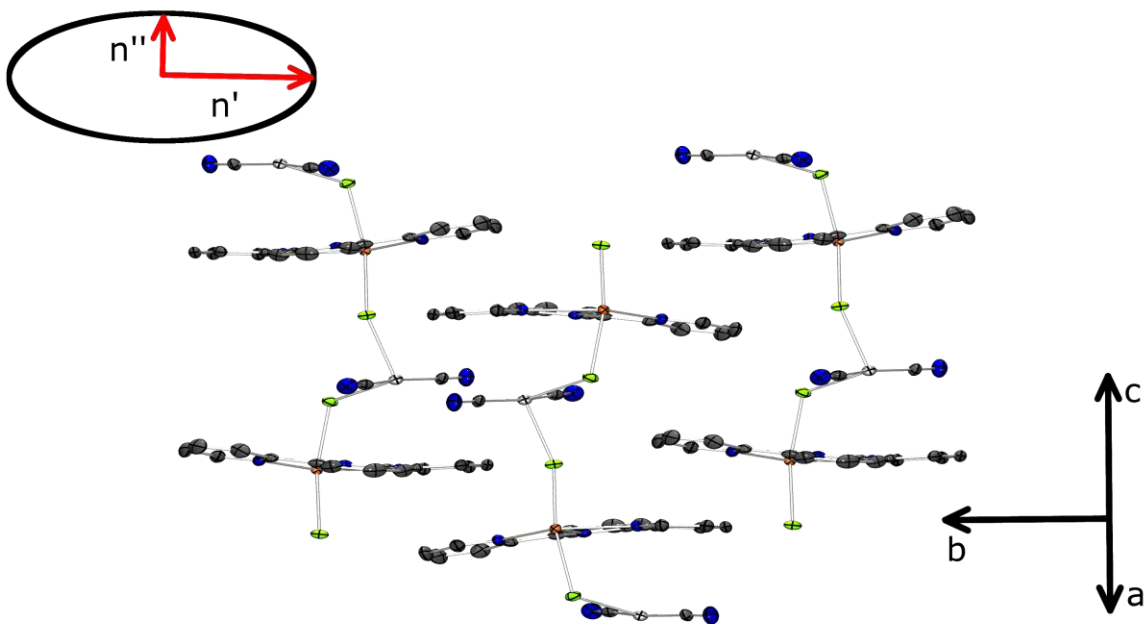


Figure 2.23. View normal to the primary crystallographic face (101) of  $\text{Pb(terpy)Cl}_2[\text{Hg(CN)}_2]_{0.5}$ . Color scheme: Pb, orange; Hg, white; Cl, green; C, grey; N, blue; H atoms, omitted for clarity.

### Birefringence of $\text{Pb(terpy)Br}_2[\text{Hg(CN)}_2]_{0.5}$

Analysis of  $\text{Pb(terpy)Br}_2[\text{Hg(CN)}_2]_{0.5}$  crystals reveals a birefringence value of 0.38(2). The crystals have monoclinic symmetry and grow as plates perpendicular to the (010) face. A view of this face again shows terpy ligands edge-on in a well-ordered network (Figure 2.24.). In this case, the measurement axis is

approximately parallel to the central pyridine-Pb bond and, therefore, is a measurement of the largest and smallest polarizability tensors of terpy. This should lead to a greater birefringence than  $\text{Hg}(\text{bbp})(\text{CN})_2$ ; however, this structure contains highly polarizable Pb-Br bonds in the axial sites, as well as Br-Hg bonds (vs Hg-CN in the previous case), which add polarizability in the low polarizability direction of bbp, therefore making the view more isotropic, resulting in the lower birefringence value.

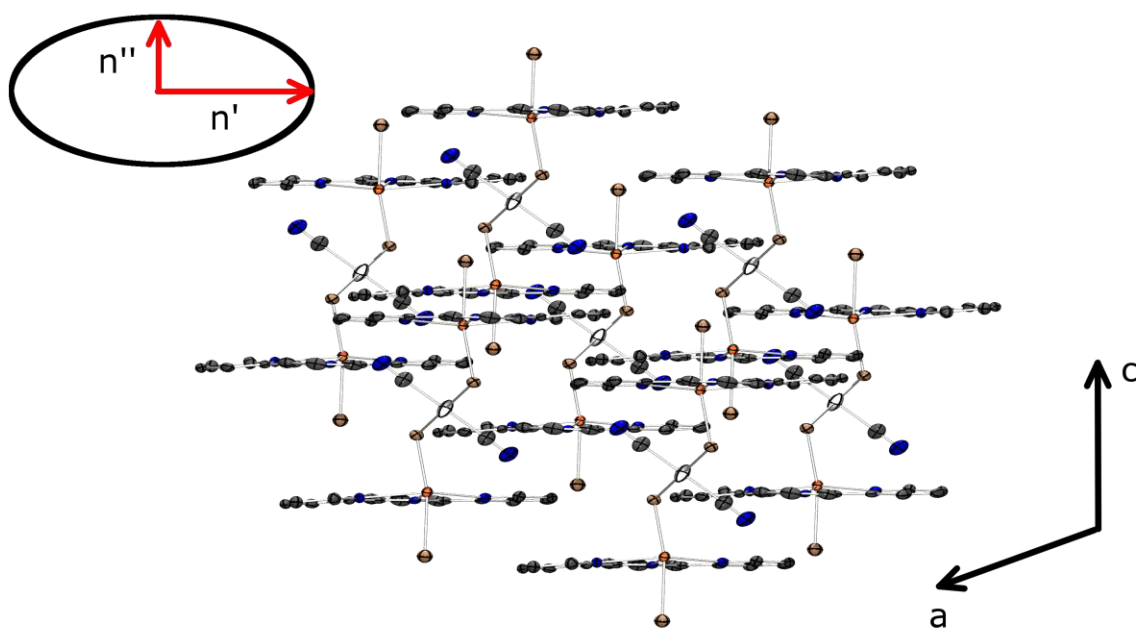


Figure 2.24. View normal to the primary crystallographic face (010) of  $\text{Pb}(\text{terpy})\text{Br}_2[\text{Hg}(\text{CN})_2]_{0.5}$ . Color scheme: Pb, orange; Hg, white; Br, brown; C, grey; N, blue; H atoms, omitted for clarity.

Solid state fluorescence data for  $\text{Hg}(\text{terpy})(\text{CN})_2$ ,  $\text{Hg}(\text{bbp})(\text{CN})_2$ , and  $\text{Pb}(\text{terpy})\text{Br}_2[\text{Hg}(\text{CN})_2]_{0.5}$  were collected at room temperature.  $\text{Hg}(\text{terpy})(\text{CN})_2$  has two broad excitation peaks centered at 310 and 337 nm. Excitation into 310 nm generates a broad emission peak centered at 373 nm while excitation into 337 nm generates emission centered about 374, 484, and 558 nm.  $\text{Pb}(\text{terpy})\text{Br}_2[\text{Hg}(\text{CN})_2]_{0.5}$  shows a broad excitation peak at approximate 388 nm which generates a broad emission peak at 518 nm. These observations are consistent with terpy-based emissions.  $\text{Hg}(\text{bbp})(\text{CN})_2$  has a single broad excitation

peak at 359 nm whereupon excitation generates emission at 440 nm consistent with bbp-based emission. Mercury spectral emission lines are also observed for Hb(bbp)(CN)<sub>2</sub> at 436, 544, and 611 nm.

## **2.7 Experimental**

### **2.7.1 General Methods and Materials**

All reactions were conducted in air. All reagents were obtained from commercial sources and used as received. IR spectra were recorded on a Thermo Nicolet Nexus 670 FTIR spectrometer equipped with a Pike MIRacle attenuated total reflection (ATR) sampling accessory with a Ge crystal. Raman spectra were recorded on a Renishaw inVia Raman Microscope equipped with a 200 mW 785 nm laser. Spectra were obtained from 100 to 3200 cm<sup>-1</sup> using a 1200 l/mm (633/780) grating for an exposure time of 10 seconds. Specific accumulations and % laser power are stated for each experiment.

#### **Measurement of Refractive Index**

The refractive indices were determined after confirmation of bulk purity through microanalysis. The powders were hand ground with a pestle and mortar to promote homogeneity in particle size and subsequently were pressed into pellets using a hydraulic press and a commercially purchased 13 mm evacuable die set. The indices of the pellets were determined through the prism coupling technique using a Metricon 2010/M refractometer equipped with a 532 and 1552 nm laser diode. All measurements were done at 1552 nm.

#### **Measurement of Birefringence**

The optical retardation and crystal thickness measurements were obtained through polarized-light microscopy using an Olympus BX60 microscope, with a tilted U-CTB thick Berek compensator at  $\lambda = 546(10)$  nm at room temperature. The birefringence was calculated by dividing the measured retardation by the crystal

thickness. The face assignment of the crystals was determined using the crystal faces application in APEX II.

### 2.7.2 Single crystal X-ray diffraction structure determinations

All crystals were mounted on a 150  $\mu\text{m}$  MiTe-Gen Dual-Thickness MicroMount using paraffin oil and data collected at room temperature unless specified. Diffraction data was collected using a Bruker SMART APEX III Duo CCD diffractometer with TRIUMPH graphite-monochromated Mo  $K\alpha$  ( $\lambda=0.71073 \text{ \AA}$ ) or Cu  $K\alpha$  ( $\lambda=1.54178 \text{ \AA}$ ). Additional crystallographic information can be found in Appendix A. Selected bond lengths and angles are displayed in Appendices B1 and B2. All diffraction data was processed with the Bruker APEX III software suite. All structures were solved with intrinsic phasing<sup>76</sup> method and subsequent refinements performed using SHELXle.<sup>77</sup> All non-hydrogen atoms were refined anisotropically. Diagrams were prepared using ORTEP-3<sup>78</sup> and POV-RAY.<sup>79</sup>

### 2.7.3 Synthetic Procedures

#### **H<sub>4</sub>[SiW<sub>12</sub>O<sub>40</sub>]· 28 H<sub>2</sub>O**

Commercially purchased tungstosilicic acid hydrate was used as received.

FT-IR (ATR,  $\text{cm}^{-1}$ ): 3733 w, 3492 w br, 1747 w br, 1611 w, 1017 w, 978 s, 916 vs, 770 vs br. Raman (514 nm, %lp: 5,  $\text{cm}^{-1}$ ): 1795 w br, 1373 m br, 1000 s, 978 w, 921 w, 536 w br, 231 m, 154 m. Anal. Calcd for H<sub>4</sub>[SiW<sub>12</sub>O<sub>40</sub>]·28 H<sub>2</sub>O: C, 0.00 %; H, 1.79 %; N, 0.00 %. Found: C, 0.00 %; H, 1.79 %; N, 0.12 %.

#### **H<sub>3</sub>[PW<sub>12</sub>O<sub>40</sub>]· 30 H<sub>2</sub>O**

Commercially purchased phosphotungstic acid hydrate was used as received.

FT-IR (ATR,  $\text{cm}^{-1}$ ): 3736 w, 3511 w br, 1725 w br, 1607 w, 1074 vs, 976 vs, 904 s, 782 vs br. Raman (514 nm, %lp: 5,  $\text{cm}^{-1}$ ): 1386 w br, 1012 s, 994 m, 931 w, 886



w, 524 w br, 477 w, 337 w, 238 m, 222 m, 159 m. Anal. Calcd for  $\text{H}_3[\text{PW}_{12}\text{O}_{40}]\cdot 30\text{H}_2\text{O}$ : C, 0.00 %; H, 1.86 %; N, 0.00 %. Found: C, 0.00 %; H, 1.86 %; N, 0.16 %.

#### **$\text{H}_4[\text{SiW}_{12}\text{O}_{40}]\cdot 4(\text{pyz})$**

Pyrazine (32 mg, 0.4 mmol) and tungstosilicic acid hydrate (575 mg, 0.2 mmol – anhydrous basis) were charged into a microwave reaction tube in 5 mL of water. The temperature was raised to 140 °C over 4 hours, held at this set-point temperature for 12 hours, followed by a cool down time of 72 hours to room temperature. White crystalline powder was isolated and washed with ethanol. Yield: 226 mg (18 %). FT-IR (ATR,  $\text{cm}^{-1}$ ): 3500 w br, 3123 w, 3096 w, 3058 w, 2975 w, 1592 w, 1479 w, 1438 w, 1377 w, 1173 w, 1077 w, 1039 w, 972 s, 915 s, 880 m, 750 vs br. Raman (514 nm, %lp: 5,  $\text{cm}^{-1}$ ): 1600 w br, 1370 w br, 1219 w, 1173 w, 1037 w, 1015 w, 994 s, 975 w, 902 w br, 883 w, 699 w, 684 w, 601 w, 537 w br, 455 w, 375 w, 243 m, 219 s, 167 m, 153 m. Anal. Calcd for  $\text{H}_4[\text{SiW}_{12}\text{O}_{40}](\text{pyz})_4$ : C, 6.01 %; H, 0.63 %; N, 3.50 %. Found: C, 6.08 %; H, 0.94 %; N, 3.46 %.

#### **$\text{H}_4[\text{SiW}_{12}\text{O}_{40}]\cdot 5(4,4'\text{-bipyridine})$**

4,4'-bipyridine (62 mg, 0.4 mmol) and tungstosilicic acid hydrate (575 mg, 0.2 mmol – anhydrous basis) were charged into a microwave reaction tube in 5 mL of water. The temperature was raised to 140 °C over 4 hours, allowed to stay at this plateau for 12 hours, followed by a cool off time of 72 hours to room temperature. White crystalline powder was isolated and washed with ethanol.

Yield: 284 mg (39 %). FT-IR (ATR,  $\text{cm}^{-1}$ ): 3474 w br, 3245 w, 3153 w, 3080 w, 2980 w, 2168 w br, 1632 w, 1598 w, 1490 w, 1390 w, 1371 w, 1354 w, 1261 w, 1242 w, 1202 w, 1048 w, 1012 w, 972 s, 919 vs, 883 m, 865 m, 778 vs, 750 vs, 730 vs. Raman (514 nm, %lp: 5,  $\text{cm}^{-1}$ ): 1648 w, 1523 w, 1297 w, 1015 m, 991 s, 908 w br, 756 w, 645 w, 570 w br, 529 w, 245 m, 217 m, 166 m, 151 m, 132 m. Anal. Calcd for  $\text{H}_4[\text{SiW}_{12}\text{O}_{40}]\cdot 5(4,4'\text{-bipyridine})$ : C, 13.72 %; H, 1.04 %; N, 3.20 %. Found: C, 13.66 %; H, 1.42 %; N, 3.23 %.

### **H<sub>3</sub>[PW<sub>12</sub>O<sub>40</sub>]·3.5(pyz)**

Pyrazine (32 mg, 0.4 mmol) and phosphotungstic acid hydrate (575 mg, 0.2 mmol – anhydrous basis) were charged into a microwave reaction tube in 5 mL of water. The temperature was raised to 140 °C over 4 hours, allowed to stay at this plateau for 12 hours, followed by a cool off time of 72 hours to room temperature. Slightly off-white crystalline powder was isolated and washed with ethanol.

Yield: 203 mg (32 %). FT-IR (ATR, cm<sup>-1</sup>): 3122 w, 3056 w, 2989 w, 2946 w, 2879 w, 1614 w, 1595 w, 1493 w, 1483 w, 1443 w, 1369 w, 1175 w, 1077 s, 976 s, 885 s, 785 vs, 762 vs br. Raman (514 nm, %lp: 5, cm<sup>-1</sup>): 1370 w br, 1224 w, 1170 w, 1006 s, 996 m, 916 w, 770 w, 695 w, 536 w, 518 w, 472 w, 237 m, 216 m, 164 m, 143 m. Anal. Calcd for H<sub>3</sub>[PW<sub>12</sub>O<sub>40</sub>](pyz)<sub>3.5</sub>: C, 5.32 %; H, 0.51 %; N, 3.10 %. Found: C, 5.63 %; H, 0.78 %; N, 2.83 %.

### **H<sub>3</sub>[PW<sub>12</sub>O<sub>40</sub>]·3(4,4'-bipyridine)**

4,4'-bipyridine (62 mg, 0.4 mmol) and phosphotungstic acid hydrate (575 mg, 0.2 mmol – anhydrous basis) were charged into a microwave reaction tube in 5 mL of water. The temperature was raised to 140 °C over 4 hours, allowed to stay at this plateau for 12 hours, followed by a cool off time of 72 hours to room temperature. White crystalline powder was isolated and washed with ethanol.

Yield: 441 mg (66 %). FT-IR (ATR, cm<sup>-1</sup>): 3240 w br, 3101 w br, 2972 w br, 1628 w, 1603 w, 1488 w, 1402 w, 1201 w, 1078 vs, 975 vs, 891 s, 786 vs br. Raman (514 nm, %lp: 5, cm<sup>-1</sup>): 1641 w, 1606 w, 1526 w, 1293 m, 1234 w, 1079 w, 1007 s, 994 s, 913 w, 766 w, 644 w, 519 w br, 472 w, 339 w, 240 m, 217 s, 164 m, 144 m. Anal. Calcd for H<sub>3</sub>[PW<sub>12</sub>O<sub>40</sub>]·3 (4,4'-bipyridine): C, 10.76 %; H, 0.81 %; N, 2.51 %. Found: C, 11.10 %; H, 1.59 %; N, 2.61 %.

### **Na<sub>2</sub>(1,5-nda)(H<sub>2</sub>O)**

Commercially purchased 1,5-naphthalenedisulfonic acid disodium salt hydrate was recrystallized from water to yield colorless plate crystals. Anal. Calcd for

$\text{Na}_2\text{C}_{10}\text{H}_8\text{O}_7\text{S}_2$ ,  $\text{Na}_2(1,5\text{-nda})(\text{H}_2\text{O})$ : C, 34.29 %; H, 2.30 %; N, 0.00 %; S, 18.31 %. Found: C, 34.25 %; H, 2.69 %; N, 0.10 %; S, 18.51 %. FT-IR (ATR,  $\text{cm}^{-1}$ ): 3440 sbr, 1700 w, 1650 m, 1502 m, 1241 s, 1223 s, 1183 vs, 1046 vs, 976 w, 911 w, 851 w, 786 s, 769 s. Raman (785 nm, a: 1, %lp: 1,  $\text{cm}^{-1}$ ): 1616 vw, 1573 vw, 1462 vw, 1402 s, 1352 s, 1175 vw, 1091 w, 1005 w, 835 w, 818 w, 726 w, 675 w, 573 w, 537 w, 514 w, 474 vw, 451 vw, 270 w, 124 vs.

### **$\text{Pb}(1,5\text{-nda})(\text{H}_2\text{O})_3$**

An equimolar amount of 1,5-nds disodium salt (100 mg, 0.3 mmol) and  $\text{Pb}(\text{ClO}_4)_2 \cdot 3\text{H}_2\text{O}$  (138 mg, 0.3 mmol) were each fully dissolved in 10 mL of water. The solution of 1,5-nds disodium salt was added dropwise to the solution of lead perchlorate. Nucleation sites were noticed after an hour and the crystals allowed to grow for a week. Colourless, cubic crystals were extracted and rinsed with cold water. Yield: 104 mg (63%). Anal. Calcd for  $\text{PbC}_{10}\text{H}_6\text{S}_2\text{O}_6(\text{H}_2\text{O})_3$ ,  $\text{Pb}(1,5\text{-nda})(\text{H}_2\text{O})_3$ : C, 21.94 %; H, 2.21 %; N, 0.00 %; S, 11.71 %. Found: C, 22.33 %; H, 2.42 %; N, 0.18%; S, 12.36 %. FT-IR (ATR,  $\text{cm}^{-1}$ ): 3418 sbr, 2955 w, 2924 w, 2857 w, 1593 wbr, 1503 w, 1335 w, 1241 m, 1203 s, 1176 s, 1160 s, 1064 m, 1031 vs, 793 s, 787 s, 768 s. Raman (514 nm, a: 1, %lp: 5,  $\text{cm}^{-1}$ ): 3086 m, 3057 w, 1617 wm, 1573 m, 1463 w, 1409 m, 1355 s, 1216 wbr, 1097 m, 1085 m, 1002 m, 838 w, 679 wbr, 569 w, 533 w, 511 vw, 482 vw, 292 vw, 192 w.

### **$\text{K}(\text{bismuthiol II})\text{H}_2\text{O}$**

Commercially purchased Bismuthiol II potassium salt was dried gently on a heating mantle and stored in a desiccator. Anal. Calcd for  $\text{KC}_8\text{H}_5\text{N}_2\text{S}_3(\text{H}_2\text{O})$ ,  $\text{K}(\text{bismuthiol II})(\text{H}_2\text{O})$ : C, 34.02 %; H, 2.50 %; N, 9.92 %. Found: C, 34.35 %; H, 2.53 %; N, 9.94 %. FT-IR (ATR,  $\text{cm}^{-1}$ ): 3533 mbr, 3410 mbr, 3064 w, 1612 m, 1594 m, 1494 m, 1473 m, 1458 m, 1422 vs, 1353 vs, 1313 m, 1297 m, 1243 vs, 1171 w, 1153 vw, 1127 w, 1073 s, 1046 vs, 1027 s, 1006 s, 992 m, 965 w, 913 w, 869 w, 831 vs, 760 vs. Raman (514 nm, a: 1, %lp: 1,  $\text{cm}^{-1}$ ): 3073 w, 2991 vw, 2975 vw, 2785 vw, 1595 vw, 1427 m, 1353 w, 1245 vw, 1030 w, 1005 vw, 725 vs, 687 vw, 651 w, 419 w, 317 vw, 249 vw, 104 w.

### **Zn(bismuthiol II)<sub>2</sub>**

Zn(ClO<sub>4</sub>)<sub>2</sub>·6H<sub>2</sub>O (223 mg, 0.6 mmol) and bismuthiol II monopotassium salt (318 mg, 1.2 mmol) were each dissolved in 5 mL of water. The solution of bismuthiol II monopotassium salt was added dropwise to the solution of zinc perchlorate resulting in instantaneous pale yellow precipitates. The reaction solution was stirred for half an hour after which the precipitate was collected and washed with cold water. The precipitate was gently dried on a heating mantle. Anal. Calcd for ZnC<sub>16</sub>H<sub>10</sub>N<sub>4</sub>S<sub>6</sub>, Zn(bismuthiol II)<sub>2</sub>: C, 37.24 %; H, 1.95 %; N, 10.86 %. Found: C, 37.14 %; H, 2.11 %; N, 10.77 %. Yield: 229 mg (74%). (FT-IR (ATR, cm<sup>-1</sup>): 3733 vw, 1591 w, 1493 m, 1434 m, 1376 m, 1356 w, 1294 w, 1245 m, 1233 m, 1218 m, 1170 w, 1157 w, 1088 m, 1040 s, 1020 s, 1003 m, 917 w, 842 s, 760 s. Raman (514 nm, a: 1, %lp: 5, cm<sup>-1</sup>): 3076 w, 1592 w, 1493 w, 1435 vs, 1376 s, 1317 w, 1244 m, 1087 w, 1024 w, 1004 w, 681 w, 649 m, 493 w, 422 w, 324 vw.

### **Pb(bismuthiol II)<sub>2</sub>**

Pb(ClO<sub>4</sub>)<sub>2</sub>·3H<sub>2</sub>O (184 mg, 0.4 mmol) and bismuthiol II monopotassium salt (212 mg, 0.8 mmol) were each fully dissolved in 10 mL of water. The solution of bismuthiol II monopotassium salt was added dropwise to the solution of lead perchlorate resulting in instantaneous yellow precipitate. The reaction solution was stirred for half an hour after which the precipitate was collected and washed with cold water. Subsequently, acetone washes were performed to remove residual moisture. Anal. Calcd for PbC<sub>16</sub>H<sub>10</sub>N<sub>4</sub>S<sub>6</sub>, Pb(bismuthiol II)<sub>2</sub>: C, 29.21 %; H, 1.53 %; N, 8.52 %; S, 29.24 %. Found: C, 29.46 %; H, 1.47 %; N, 8.56 %; S, 29.60 %. Yield: 233 mg (89%). FT-IR (ATR, cm<sup>-1</sup>): 1590 w, 1493 s, 1480 m, 1456 m, 1422 vs, 1365 vs, 1242 vs, 1158 vw, 1138 vw, 1092 w, 1080 m, 1074 m, 1051 vs, 1031 s, 1024 s, 1003 m, 963 vw, 913 w, 839 s, 761 m. Raman (514 nm, a: 1, %lp: 5, cm<sup>-1</sup>): 1424 vs, 1336 m, 1240 m, 1080 w, 1032 w, 650 w, 495 vw, 421 w, 388 vw, 158

### **K<sub>2</sub>(bismuthiol I)(H<sub>2</sub>O)<sub>0.5</sub>**

Commercially purchased Bismuthiol I dipotassium salt was slurried in acetone to remove moisture. Anal. Calcd for  $K_2C_2N_2S_3(H_2O)_{0.5}$ ,  $K_2(\text{bismuthiol I})(H_2O)_{0.5}$ : C, 10.20 %; H, 0.43 %; N, 11.90 %; S, 40.85 %. Found: C, 10.06 %; H, 0.49 %; N, 11.75 %; S, 41.68 %. FT-IR (ATR,  $cm^{-1}$ ): 1454 vw, 1404 vw, 1342 s, 1293 w, 1266 w, 1217 w, 1151 m, 1110 m, 1064 vw, 1031 vs, 733 vw, 715 vs. Raman (514 nm, a: 1, %lp: 5,  $cm^{-1}$ ): 1364 vs, 1013 m, 637 m, 383 vw, 326 vw, 221 vw, 130 vw.

### **Zn(bismuthiol I +H)<sub>2</sub>**

An equimolar amount of bismuthiol I dipotassium salt (136 mg, 0.6 mmol) and  $Zn(ClO_4)_2 \cdot 6H_2O$  (223 mg, 0.6 mmol) were charged into a 50-mL round bottom flask. A 10 mL aliquot of water was added and the reaction mixture allowed to stir and reflux under ambient conditions for 2 hours. The instantaneous formation of white precipitate was noted. After 2 hours, the flask was removed, allowed to cool, and the water pipetted out. A 10-mL aliquot of methanol was added to the flask and subsequently allowed to reflux for 15 minutes to remove unreacted starting materials. This methanol reflux was duplicated upon removal of the first aliquot. The reaction mixture was transferred over to a 4-dram vial and dried on the rotary evaporator. Amorphous, white precipitate was obtained. Yield: 106 mg (49%). Anal. Calcd for  $ZnC_4N_4S_6H_2$ ,  $Zn(\text{bismuthiol I}+H)_2$ : C, 13.21 %; H, 0.55 %; N, 15.40 %; S, 52.87 %. Found: C, 13.32 %; H, 0.64 %; N, 15.32 %; S, 53.11 %. FT-IR (ATR,  $cm^{-1}$ ): 3359 wbr, 1608 w, 1390 s, 1377 s, 1366 s, 1359 s, 1094 vs, 1053 m, 779 m. Raman (514 nm, a: 1, %lp: 5,  $cm^{-1}$ ): 1394 mbr, 1104 wbr, 1047 wbr, 700 w, 670 w, 387 vw.

### **Pb(bismuthiol I)**

An equimolar amount of bismuthiol I dipotassium salt (68 mg, 0.3 mmol) and  $Pb(ClO_4)_2 \cdot 3H_2O$  (138 mg, 0.3 mmol) were each fully dissolved in 10 mL of water. The solution of bismuthiol I dipotassium salt was added dropwise to the solution of lead perchlorate, resulting in instantaneous yellow precipitate. The reaction solution was stirred for half an hour, after which the precipitate was collected and washed with cold water. Subsequently, acetone washes were performed to

remove residual moisture. Attempts to isolate single crystals of Pb(bismuthiol I) have been unsuccessful. Yield: 96 mg (90%). Anal. Calcd for  $\text{PbC}_2\text{N}_2\text{S}_3$ , Pb(bismuthiol I): C, 6.76%; H, 0.00%; N, 7.88%; S, 27.06%. Found: C, 6.94%; H, 0.15%; N, 8.01%; S, 27.68%. FT-IR (ATR,  $\text{cm}^{-1}$ ): 1346 vs, 1145 w, 1059 vs, 897 w, 760 m. Raman (514 nm, a: 1, %lp: 5,  $\text{cm}^{-1}$ ): 1728 vw, 1350 vs, 1071 m, 1059 w, 756 vw, 662 vw, 601 vw, 542 vw, 380 m, 349 vw, 199 w, 161 w, 136 w.

### **Hg(terpy)(CN)<sub>2</sub>**

Hg(CN)<sub>2</sub> (25 mg, 0.1 mmol) was dissolved in 5 mL of methanol. A methanol solution of terpy (23 mg, 0.1 mmol) was added dropwise to the Hg(CN)<sub>2</sub> to create a pale-yellow solution. The solvent was slowly evaporated over three days to give colorless crystals of Hg(terpy)(CN)<sub>2</sub>. Yield: 48 mg (99%). FTIR (ATR,  $\text{cm}^{-1}$ ): 3067 wbr, 2165 ( $\nu_{\text{CN}}$ , vw) 1591 m, 1580 m, 1573 m, 1479 m, 1445 ms, 1431 ms, 1396 w, 1336 vw, 1309 w, 1289 vw, 1244 w, 1192 vw, 1172 w, 1148 w, 1084 vw, 1047 vw, 1001 m, 828 w, 767 vs, 725 w. Raman (785 nm, %lp: 50,  $\text{cm}^{-1}$ ): 2166 ( $\nu_{\text{CN}}$ , s), 1589 s, 1566 m, 1490 m, 1446 m, 1324 s, 1291 m, 1264 m, 1192 vw, 1116 w, 1070 w, 1041 w, 1005 s, 792 m, 723 w, 649 w, 636 w, 395 vw, 369 m, 317 w, 274 w, 257 w, 218 m, 142 m, 125 s. Anal. Calcd for  $\text{C}_{17}\text{H}_{11}\text{N}_5\text{Hg}$  (Hg(terpy)(CN)<sub>2</sub>): C, 42.02%; H, 2.28%; N, 14.41%. Found: C, 41.92%; H, 2.32%; N, 14.06%.

Alternatively, this material can also be synthesized hydrothermally by heating Hg(CN)<sub>2</sub> (25 mg, 0.1 mmol) and terpy (23 mg, 0.1 mmol) in 3 mL of water to 135 °C, maintaining this plateau for 12 h, followed by cooling over 60 h. Colorless crystals were collected via filtration. Yield: 48 mg (99%).

### **Hg(bbp)(CN)<sub>2</sub>(H<sub>2</sub>O)**

The bbp (31 mg, 0.1 mmol) and Hg(CN)<sub>2</sub> (25 mg, 0.1 mmol) were added to a microwave vial with 6 mL of H<sub>2</sub>O before sealing the vial under ambient conditions. The vial was heated to 125 °C, maintained at this plateau temperature for 12 h, followed by cooling over 60 h. Light beige–brown crystals were collected via filtration and washed with hot H<sub>2</sub>O and methanol. Yield: 47 mg (81%). FTIR (ATR,

cm<sup>-1</sup>): 3493 mbr, 3355 ms, 2989 m, 2182 ( $\nu_{CN}$ , vw), 2171 ( $\nu_{CN}$ , vw), 1934 vw, 1890 vw, 1603 s, 1589 s, 1579 s, 1494 w, 1475 m, 1454 s, 1431 s, 1428 s, 1374 w, 1340 w, 1315 m, 1289 s, 1252 w, 1235 wm, 1185 w, 1150 wm, 1116 wm, 1029 vw, 1001 wm, 992 wm, 965 w, 928 w, 905 w, 843 m, 817 s, 804 w, 762 s, 744 vs, 735 vw. Raman (785 nm, %lp: 50, cm<sup>-1</sup>): 2182 ( $\nu_{CN}$ , vw), 2171 ( $\nu_{CN}$ , vw), 1629 wm, 1605 m, 1578 m, 1545 m, 1528 s, 1491 wm, 1456 vw, 1447 s, 1430 vw, 1363 vw, 1318 w, 1289 m, 1266 ms, 1238 w, 1153 wm, 1123 vw, 1009 s, 1000 s, 965 w, 805 w, 762 vw, 751 vw, 739 vw, 661 w, 625 w, 380 vw, 321 vw, 271 vw, 197 vw, 186 vw. Anal. Calcd for C<sub>21</sub>H<sub>15</sub>N<sub>7</sub>HgO (Hg(bbp)(CN)<sub>2</sub>(H<sub>2</sub>O)): C, 43.34%; H, 2.60%; N, 16.85%. Found: C, 43.41%; H, 2.82%; N, 16.96%.

### **Pb(terpy)Cl<sub>2</sub>[Hg(CN)<sub>2</sub>]<sub>0.5</sub>**

Pale yellow crystals of Pb(terpy)Cl<sub>2</sub>[Hg(CN)<sub>2</sub>]<sub>0.5</sub> were synthesized hydrothermally by heating PbCl<sub>2</sub> (28 mg, 0.1 mmol), terpy (23 mg, 0.1 mmol), and Hg(CN)<sub>2</sub> (75 mg, 0.3 mmol) in 6 mL H<sub>2</sub>O to 140 °C, maintaining this plateau temperature for 12 h, followed by cooling over 48 h. Crystals were collected through filtration and washed with H<sub>2</sub>O and methanol prior to mechanical separation from unreacted PbCl<sub>2</sub>. Yield: 7 mg (11%). FTIR (ATR, cm<sup>-1</sup>): 2163 ( $\nu_{CN}$ , vw), 1619 w, 1591 s, 1581 s, 1542 w, 1521 w, 1508 w, 1478 s, 1447 s, 1432 s, 1399 w, 1307 m, 1291 w, 1244 m, 1192 w, 1170 w, 1155 w, 1088 vw, 1073 vw, 1054 vw, 1006 m, 828 w, 768 vs, 726 w. Raman (785 nm, %lp: 5, cm<sup>-1</sup>): 2167 ( $\nu_{CN}$ , vw), 1589 vs, 1566 m, 1481 m, 1489 m, 1452 ms, 1324 vs, 1291 ms, 1264 m, 1256 w, 1043 w, 1005 vs, 825 vw, 792 vw, 723 vw, 647 vw, 638 vw, 620 vw, 271 vw, 221 w, 125 m. Anal. Calcd for C<sub>32</sub>H<sub>22</sub>N<sub>8</sub>Cl<sub>4</sub>HgPb<sub>2</sub> (Pb(terpy)Cl<sub>2</sub>[Hg(CN)<sub>2</sub>]<sub>0.5</sub>)<sub>2</sub>: C, 30.14%; H, 1.74%; N, 8.79%. Found: C, 30.18%; H, 1.82%; N, 9.02%.

### **Pb(terpy)Br<sub>2</sub>[Hg(CN)<sub>2</sub>]<sub>0.5</sub>**

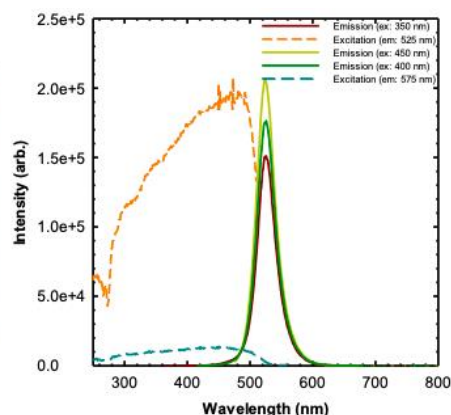
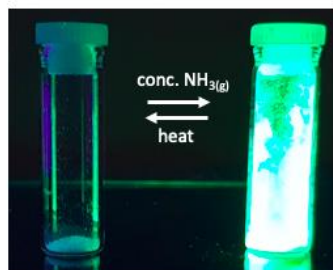
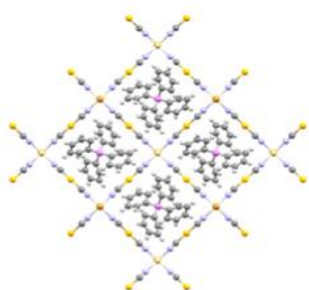
Pale yellow plates of Pb(terpy)Br<sub>2</sub>[Hg(CN)<sub>2</sub>]<sub>0.5</sub> were synthesized hydrothermally by heating PbBr<sub>2</sub> (37 mg, 0.1 mmol), terpy (23 mg, 0.1 mmol) and Hg(CN)<sub>2</sub> (75 mg, 0.3 mmol) in 3 mL H<sub>2</sub>O to 140 °C, maintaining this plateau temperature for 12 h, followed by cooling over 60 h. Crystals were collected through filtration and

washed with methanol. Yield: 51 mg (70%). FTIR (ATR,  $\text{cm}^{-1}$ ): 3105 w, 3071 m, 3015 w, 1590 ms, 1573 m, 1564 m, 1506 w, 1483 ms, 1449 s, 1434 s, 1419 w, 1395 w, 1311 m, 1263 w, 1244 m, 1197 m, 1169 ms, 1159 ms, 1092 w, 1072 w, 1053 w, 1009 s, 970 w, 833 w, 798 w, 776 vs, 732 w. Raman (785 nm, %lp: 10,  $\text{cm}^{-1}$ ) 2177 ( $\nu_{\text{CN}}$ , s), 1591 m, 1564 m, 1496 m, 1475 w, 1455 w, 1328 vs, 1297 m, 1264 w, 1111 m, 1074 m, 1042 ms, 1013 s, 828 w, 808 w, 733 w, 722 m, 653 m, 632 m, 509 w, 300 m, 285 m, 267 m, 219 m, 154 m, 132 s, 112 vs. Anal. Calcd for  $\text{C}_{32}\text{H}_{22}\text{N}_8\text{Br}_4\text{HgPb}_2$  ( $\text{Pb}(\text{terpy})\text{Br}_2[\text{Hg}(\text{CN})_2]_{0.5}$ )<sub>2</sub>: C, 26.45%; H, 1.53%; N, 7.71%. Found: C, 26.12%; H, 1.51%; N, 7.58%.



## Chapter 3

# Luminescent Response of Group 12 Dicyanoaurate Coordination Polymers To Ammonia



### 3.1 Introduction

The use of ammonia as a refrigerant has increased since the ratification of the Montreal Protocol in 1989, which prohibited the use of chlorofluorocarbons (CFCs) and related materials due to their high ozone depletion potential.<sup>158–162</sup> Ammonia has many properties that make it an ideal refrigerant species: it has an ozone depletion potential of zero, is relatively inexpensive to produce and to use, and has a high heat of vaporization.<sup>163</sup> It also finds heavy usage in agricultural settings as fertilizer.<sup>160</sup> However, the use of ammonia does also have some drawbacks. In the presence of moisture, ammonia corrodes copper- and zinc- containing alloys so care must be taken to not use these materials when dealing with ammonia, to prevent leaks. Exposures to high concentrations of ammonia also have negative physiological impacts.<sup>164</sup> Ammonia is corrosive and an irritant to which exposure can result in respiratory distress, chemical burns, and can be lethal at concentrations higher than 300 ppm.<sup>165</sup> US-OSHA guidelines restrict the permissible exposure limit for ammonia to be 50 parts per million (ppm) averaged over an eight hour work day.<sup>166</sup> The human nose can detect ammonia at concentrations of >5 ppm but there are additional considerations, reflex glottis closure, a protective response of the body towards inhaling irritants, is seen to be

invoked at increasing concentrations as individuals age.<sup>167</sup> Ammonia also causes olfactory fatigue or adaptation which diminishes an individual's ability to smell ammonia after prolonged exposure.<sup>168</sup>

There are a variety of methods utilized to sense gaseous ammonia, which generally have the sensing basis of detecting changes in current and resistivity of a material brought about by the adsorption of the analyte (ammonia) and subsequent alteration of its electrical properties.<sup>169–171</sup> Some examples of sensing platforms include metal-oxide based materials,<sup>32,33</sup> catalytic materials based on the activity of some metals towards ammonia,<sup>172,173</sup> and conductive polymer sensors.<sup>174,175</sup> The main drawbacks of this type of sensing platform is that they often display poor selectivity towards ammonia and are operated at high temperatures.<sup>176,177</sup> Common interferences include the presence of other reducing gases such as methane, hydrogen sulfide, and carbon monoxide which would compete with ammonia and lead to an increase in conductivity.<sup>176</sup>

Another synthetic platform that has shown success in detecting ammonia and other analytes is CPs which use an optical readout rather than an electrical one.<sup>178–181</sup> The aurophilicity of Gold(I) is harnessed into a sensing platform towards concentrated ammonia vapours in this chapter. Previous work in the group had shown that CPs incorporating dicyanoaurate,  $[\text{Au}(\text{CN})_2]^-$  can display luminescent sensing properties<sup>181–184</sup> and more specifically that those containing zinc with dicyanoaurate have shown excellent response towards ammonia based on changes in Au-Au distances in the structure upon binding of  $\text{NH}_3$  generating a shift in emission energy.<sup>69</sup> A new family of coordination polymers synthesized from halogenated zinc metal salts, templating cations of  $[\text{Ph}_4\text{As}]^+$  or  $[\text{Ph}_4\text{P}]^+$  (Ph = Phenyl,  $-\text{C}_6\text{H}_5$ ), and dicyanoaurate were synthesized to expand on this prior work, in which the key elements of a zinc binding site and emissive cyanoaurate units were preserved but the supramolecular structure and stoichiometry altered with respect to the aforementioned  $\text{Zn}[\text{Au}(\text{CN})_2]_2$ . In addition, recently, the use of cadmium-based coordination polymers and MOFs as a sensing platform has been gaining traction.<sup>185,186</sup> As such, the analogous halogenated cadmium products

have also been synthesized in attempt to discern the effect of using a different group 12 metal cation. Synthesis of the corresponding halogenated mercury analogues were attempted but coordination polymers were not obtained. Thus, herein, a family of CPs of the form  $\text{Ph}_4\text{AsMX}[\text{Au}(\text{CN})_2]_2$  ( $\text{Ph}_4\text{As}$ : tetraphenylarsonium;  $\text{MX}$ :  $\text{ZnCl}$ ,  $\text{CdCl}$ ,  $\text{CdBr}$ ) and  $\text{Ph}_4\text{AsMX}_2[\text{Au}(\text{CN})_2]$  ( $\text{MX}_2$ :  $\text{ZnBr}_2$ ,  $\text{ZnI}_2$ ) are described. The sensing performance of these materials towards gaseous ammonia is discussed.

### 3.2 Group 12 metal dicyanoaurate coordination polymers for sensing of ammonia

Bench-top reactions of an equimolar amount of  $\text{Ph}_4\text{As}[\text{Au}(\text{CN})_2]$  and Group 12 metal halides produced two classes of crystalline material. The first class (3.2.1) crystallizes into the tetragonal space group,  $P4/n$ , and adopts the general formula of  $\text{Ph}_4\text{AsMX}[\text{Au}(\text{CN})_2]_2$  ( $\text{MX}$ :  $\text{ZnCl}$ ,  $\text{CdCl}$ ,  $\text{CdBr}$ ). The second class (3.2.2) crystallizes into the orthorhombic space group,  $P2_12_12_1$ , and adopts the general formula of  $\text{Ph}_4\text{AsMX}_2[\text{Au}(\text{CN})_2]$  ( $\text{MX}_2$ :  $\text{ZnBr}_2$ ,  $\text{ZnI}_2$ ). Initially, these reactions were performed using equimolar amounts of dicyanoaurate and metal halide salts, producing polymers with the two stoichiometries between the metal and dicyanoaurate. In all cases, the  $\nu_{\text{CN}}$  stretches observed in the IR and Raman spectra shifted to higher energies compared with free  $\text{K}[\text{Au}(\text{CN})_2]$  ( $2142\text{ cm}^{-1}$  in IR), consistent with ligand to metal binding through donation of electron density from an antibonding molecular orbital. Attempts to synthesize materials with the other stoichiometry (e.g. hypothetical  $\text{Ph}_4\text{AsZnBr}[\text{Au}(\text{CN})_2]_2$ ) by tuning the amounts of reagents used to match the stoichiometry expected in the solid-state structure, and by modifying reaction temperatures under the assumption that the 2:1 M:Au product was the thermodynamic product and the 1:1 M:Au the kinetic product were carried out to no avail. This reactivity is summarized in Figure 3.1. below.

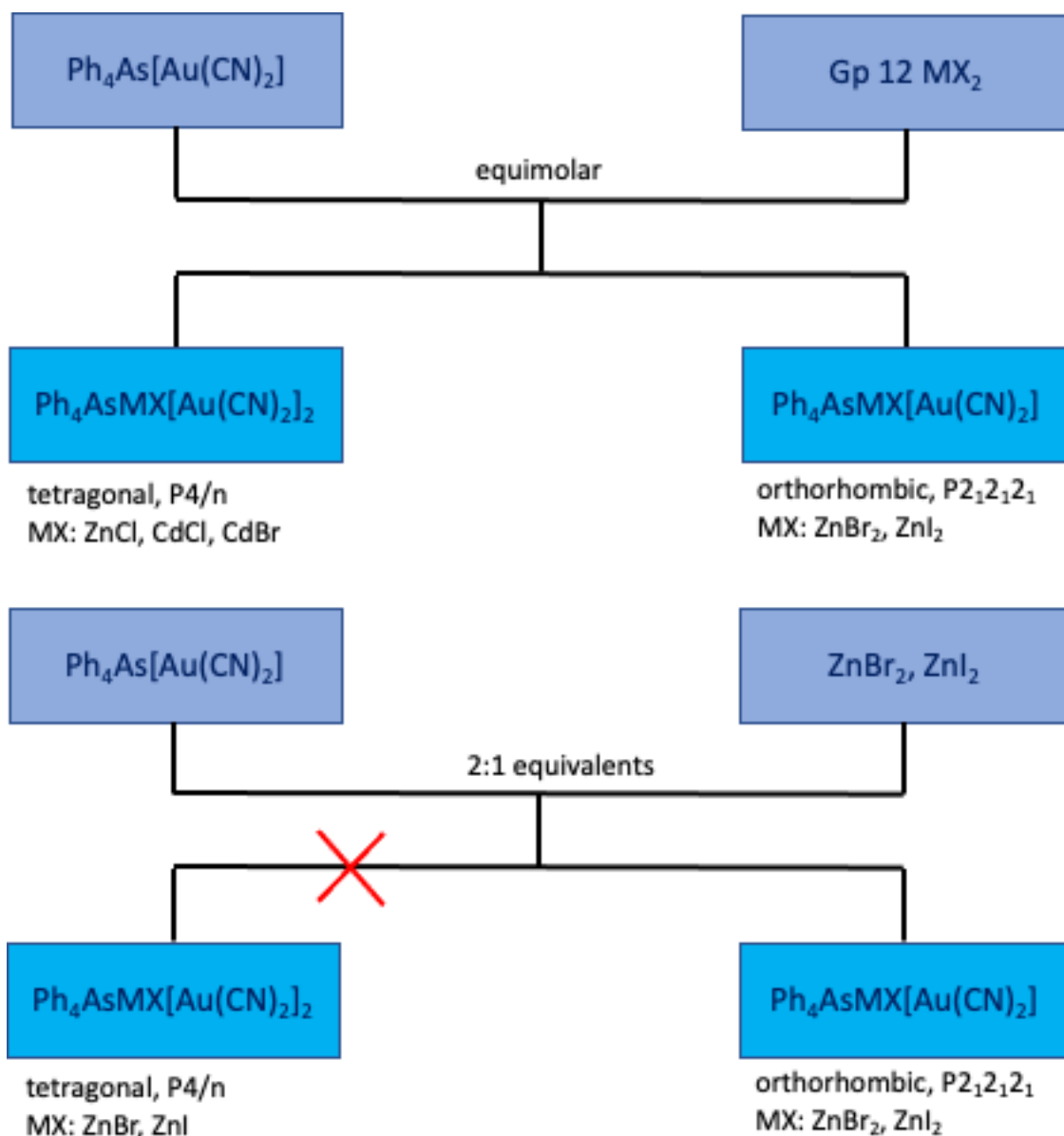


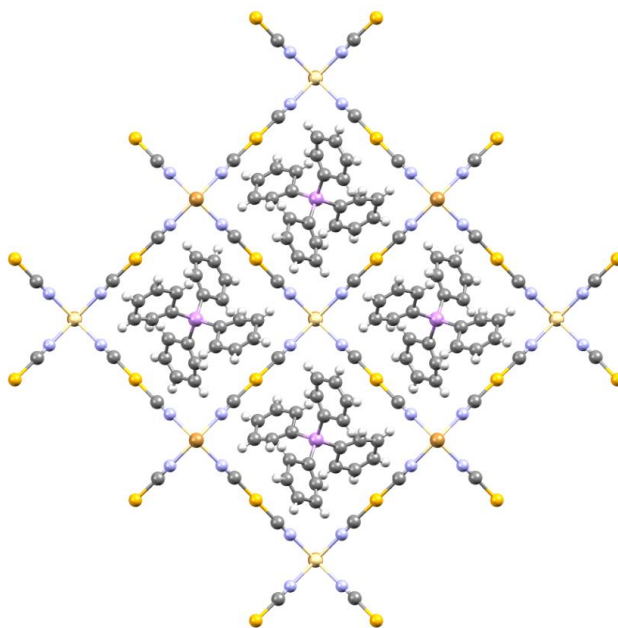
Figure 3.1. Reaction scheme of Group 12 metal halides and  $\text{Ph}_4\text{As}[\text{Au}(\text{CN})_2]$

These materials are sensitive towards concentrated ammonia vapors and undergo changes in luminescence upon exposure. These materials are fully characterized herein and their practicality for use in ammonia sensing discussed. The  $[\text{Ph}_4\text{P}]^+$  cation was also used in place of  $[\text{Ph}_4\text{As}]^+$  in each of the two structural forms to mitigate the toxicity concerns of using arsenic containing materials.

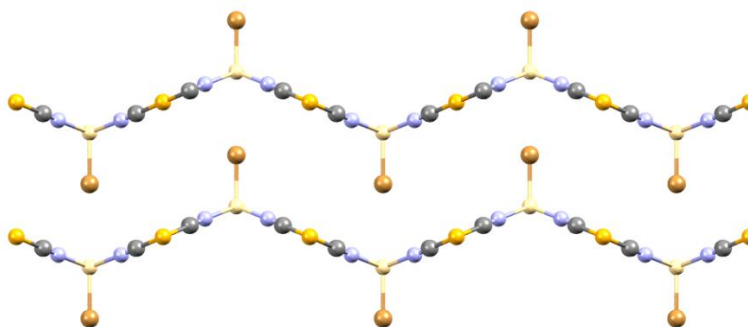
### 3.2.1 Synthesis, Structure, and Characterization of Coordination Polymers of the Form $\text{Ph}_4\text{AsMX}[\text{Au}(\text{CN})_2]_2$

Reaction of a 1-to-2 molar ratio of group 12 metal halides ( $\text{ZnCl}_2$ ,  $\text{CdCl}_2$ ,  $\text{CdBr}_2$ ) with  $\text{Ph}_4\text{As}[\text{Au}(\text{CN})_2]$  or  $\text{Ph}_4\text{P}[\text{Au}(\text{CN})_2]$  in ethanol yields isostructural coordination polymers of the form  $\text{Ph}_4\text{AsMX}[\text{Au}(\text{CN})_2]_2$  and  $\text{Ph}_4\text{PMX}[\text{Au}(\text{CN})_2]_2$  respectively (MX:  $\text{ZnCl}$ ,  $\text{CdCl}$ ,  $\text{CdBr}$ ). Reaction of the two materials in a 1:1 stoichiometry only gave lower yields of the 1:2 product.

In these isostructural systems, the  $\text{Zn(II)}$  or  $\text{Cd(II)}$  centre adopts a distorted square pyramidal geometry with four N-bound  $[\text{Au}(\text{CN})_2]^-$  units occupying the base and a halide (either  $\text{Cl}$  or  $\text{Br}$ ) capping the axial position (Figure 3.2.). The  $[\text{Au}(\text{CN})_2]^-$  units are all bridging and join the metal cations into a 2-D dimensional anionic pleated sheet, with the  $\text{Ph}_4\text{As}$  or  $\text{Ph}_4\text{P}$  cations occupying the grids of the sheet, in the interstitial spaces. The sheet is not planar; the grid lines are oriented in a zig-zag manner with the halide occupying alternating up and down positions.



(a)



(b)

Figure 3.2. Crystal structure of 2-D sheet motif,  $\text{Ph}_4\text{As}(\text{Ph}_4\text{P})\text{MX}[\text{Au}(\text{CN})_2]_2$

a) top-down view and b) side view. MX:  $\text{ZnCl}$ ,  $\text{CdCl}$ ,  $\text{CdBr}$ . Colour scheme: Au, yellow; N, blue; C, grey; As(P), purple; H, white; halide (X), brown; metal (M), beige.

### 3.2.2 Synthesis, Structure, and Characterization of Coordination Polymers of the Form $\text{Ph}_4\text{AsMX}_2[\text{Au}(\text{CN})_2]$

Reaction of an equimolar amount of  $\text{ZnBr}_2$  and  $\text{ZnI}_2$  with  $\text{Ph}_4\text{As}[\text{Au}(\text{CN})_2]$  or  $\text{Ph}_4\text{P}[\text{Au}(\text{CN})_2]$  in ethanol yields isostructural coordination polymers of the form

$\text{Ph}_4\text{AsMX}_2[\text{Au}(\text{CN})_2]$  and  $\text{Ph}_4\text{PMX}_2[\text{Au}(\text{CN})_2]$  respectively ( $\text{MX}_2$ :  $\text{ZnBr}_2$ ,  $\text{ZnI}_2$ ). Reaction of the two materials in a 1:2 stoichiometry yielded the same 1:1 product.

The 1:1 products has a distinctively different structure than the 1:2 products. Instead of the pleated-sheets seen for the 1:2, the 1:1 system contains chains. In this system, zinc (II) centres are connected by a single bridging N-bound  $[\text{Au}(\text{CN})_2]^-$  unit, forming a 1-dimensional anionic chain where each metal centre adopts a tetrahedral geometry (Figure 3.3.). The Zn(II) coordination sphere is filled by two halide atoms and the two N-cyano units. The  $\text{Ph}_4\text{As}$  and  $\text{Ph}_4\text{P}$  cations occupy the interstitial spaces between the chains.

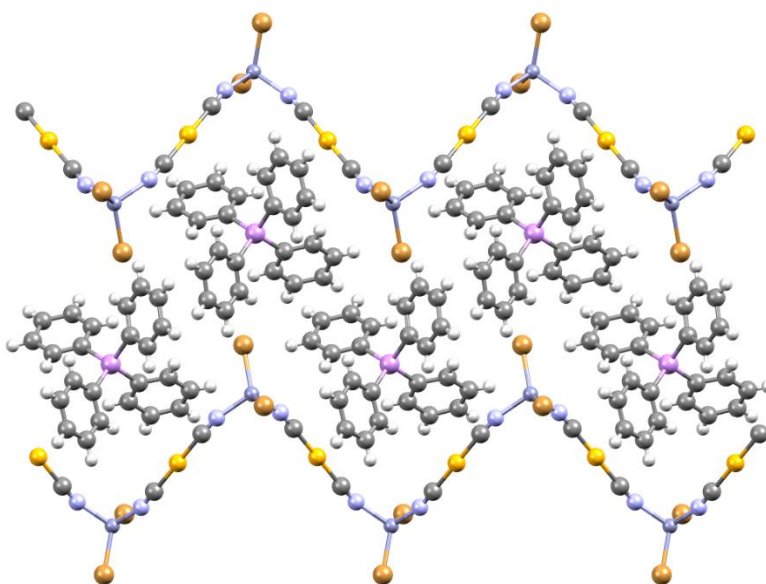


Figure 3.3. Crystal structure of 1-D chain motif,  $\text{Ph}_4\text{As}(\text{Ph}_4\text{P})\text{MX}_2[\text{Au}(\text{CN})_2]$ .

Color scheme: Au, yellow; C, grey; N, blue; As(P), purple; H, white; halide (X), brown; metal (M), light grey.

### 3.2.3 Luminescence Analysis of $\text{Ph}_4\text{AsMX}[\text{Au}(\text{CN})_2]_2$ and $\text{Ph}_4\text{AsMX}_2[\text{Au}(\text{CN})_2]$

$\text{Zn}[\text{Au}(\text{CN})_2]_2$  was another ammonia sensing system produced by our group.<sup>69</sup> In the original synthesis, four different polymorphs with slightly different excitation and emission maxima were obtained. These excitation maxima range from 345-390 nm and the emission has maxima centred about 390 and 480 nm which are

attributed to Au-Au based singlet fluorescence and triplet phosphorescence respectively. In contrast,  $\text{Ph}_4\text{AsMX}[\text{Au}(\text{CN})_2]_2$  (MX: ZnCl, CdCl, CdBr) and  $\text{Ph}_4\text{AsMX}_2[\text{Au}(\text{CN})_2]$  (MX<sub>2</sub>: ZnBr<sub>2</sub>, ZnI<sub>2</sub>),  $\text{Ph}_4\text{PCdCl}[\text{Au}(\text{CN})_2]_2$ , and  $\text{Ph}_4\text{PZnBr}_2[\text{Au}(\text{CN})_2]$  lack Au-Au emissions but exhibit emissions attributed to the cations,  $[\text{Ph}_4\text{As}]^+$  and  $[\text{Ph}_4\text{P}]^+$ .  $\text{Ph}_4\text{AsZnCl}[\text{Au}(\text{CN})_2]$  and  $\text{Ph}_4\text{AsCl}$  have two emission profiles centered about 360-420 nm and 425-600 nm (Figure 3.4.). Excitation into the higher energy absorption band (305 nm) leads to preferential fluorescence from the lower energy emission profile. Conversely, excitation into the lower energy absorption band (337 nm) leads to preferential fluorescence from the higher energy emission profile. Interestingly, the emission intensity of a sample of  $\text{Ph}_4\text{AsZnBr}_2[\text{Au}(\text{CN})_2]$  was seen to increase after thermal annealing at a temperature of 160°C for one hour with a concomitant blue shift of 19 nm in the emission maxima to 468 nm. This observation was not explored further.

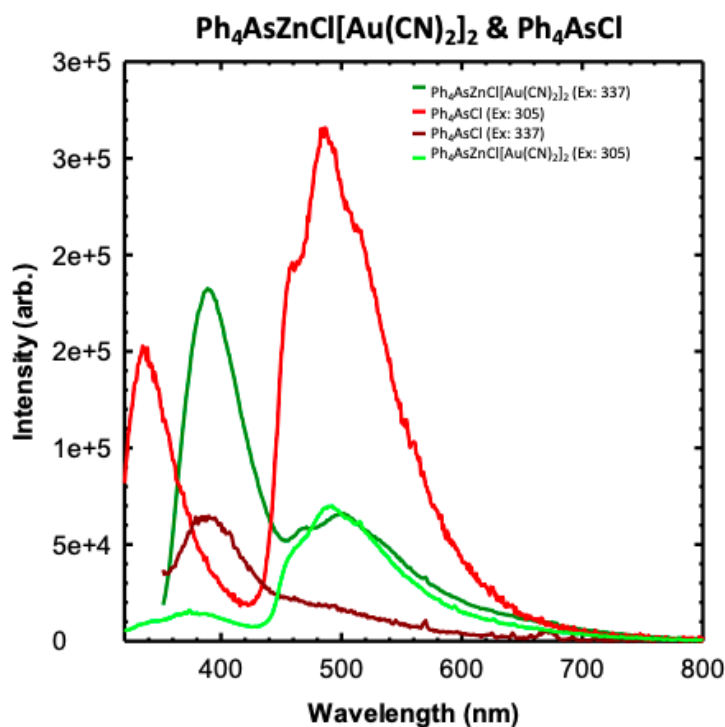


Figure 3.4. Solid-state luminescence spectra of native  $\text{Ph}_4\text{AsZnCl}[\text{Au}(\text{CN})_2]_2$  and  $\text{Ph}_4\text{AsCl}$  excited at 305 and 337 nm. Data collected at room temperature.



Similarly, native  $\text{Ph}_4\text{AsZnBr}_2[\text{Au}(\text{CN})_2]$  has two emission profiles centered about 360-420 nm and 425-600 nm (Figure 3.5.). Similar emissive properties seen for  $\text{Ph}_4\text{AsZnCl}[\text{Au}(\text{CN})_2]_2$  are observed for  $\text{Ph}_4\text{AsZnBr}_2[\text{Au}(\text{CN})_2]$ .

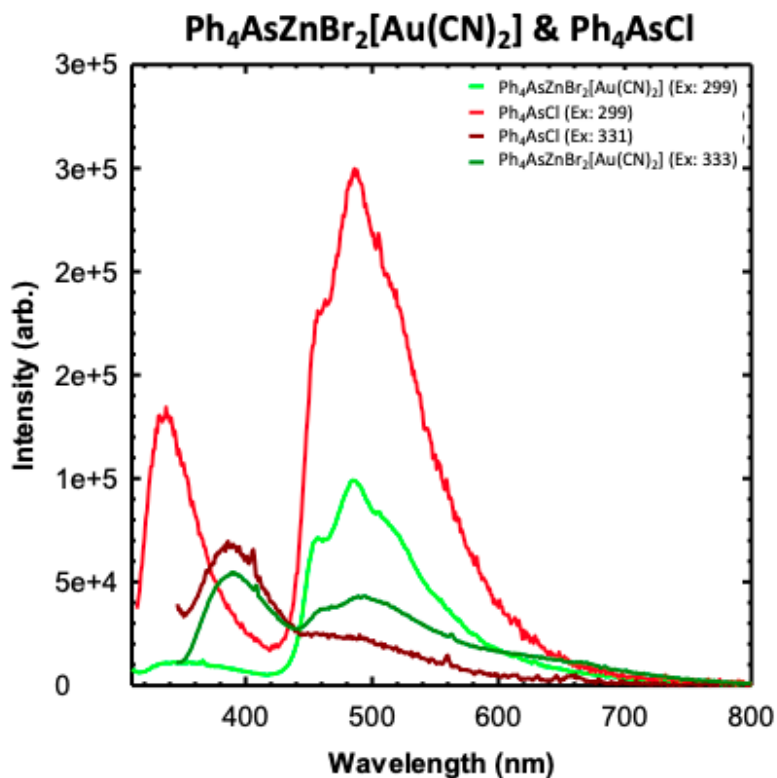


Figure 3.5. Solid-state luminescence spectra of native  $\text{Ph}_4\text{AsZnBr}_2[\text{Au}(\text{CN})_2]$  and  $\text{Ph}_4\text{AsCl}$  excited at 299 and 331 nm. Data collected at room temperature.

$[\text{Ph}_4\text{P}]\text{CdCl}[\text{Au}(\text{CN})_2]_2$  and  $[\text{Ph}_4\text{P}]\text{Br}$  have two emission profiles centered about 355-400 nm and 420-600 nm (Figure 3.6.). Excitation into the lower energy absorption (327 nm) of  $\text{Ph}_4\text{PBr}$  leads to enhancement of the higher energy emission. Comparatively, the intensity of the higher energy emission in the CP is greatly reduced when exciting into this band.

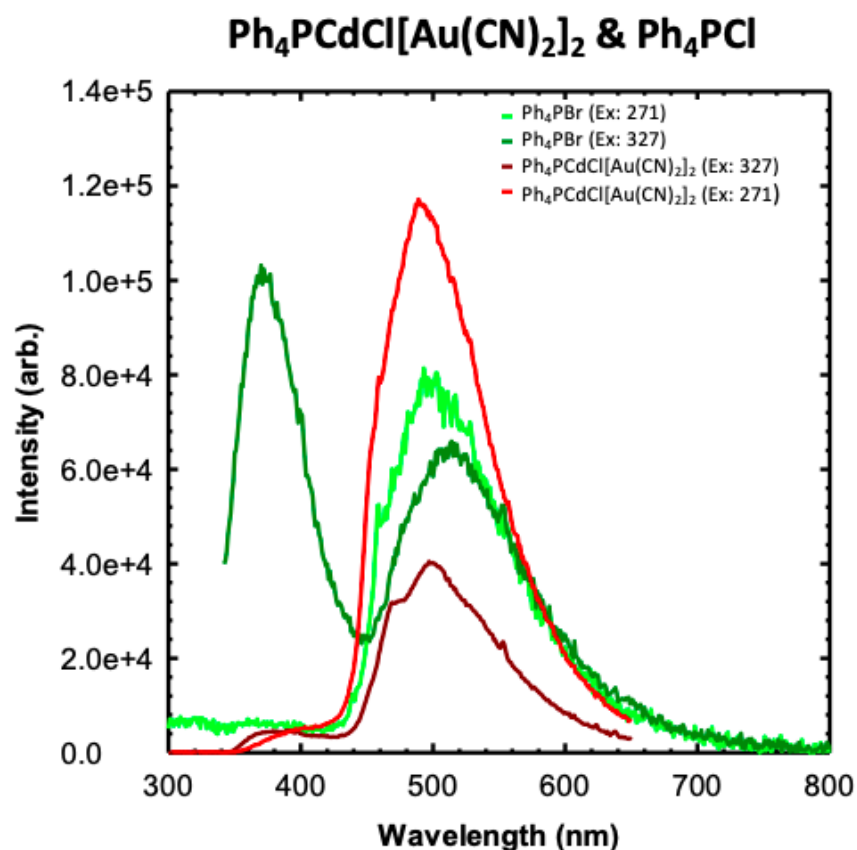


Figure 3.6. Luminescence spectra of native  $\text{Ph}_4\text{PCdBr}[\text{Au}(\text{CN})_2]_2$  and  $\text{Ph}_4\text{PBr}$  excited at 271 and 327 nm.

Since the emission profiles overlap for the cationic species (in halide form) overlap those seen in the native CPs, it is concluded that the origin of the emission from the native materials is from the cations.

### 3.2.4 Ammoniation of the Native Materials and Characterization Attempts

Both the 1-D and 2-D materials lack Au-Au contacts of  $< 3.6 \text{ \AA}$  and thus have no Au-Au interactions and resultingly display no Au-based luminescence. However, intense luminescence is noted upon ammoniation of these species which is suggestive of gold-gold contacts being formed due to a structural rearrangement.

This is supported by the observation of the decrease in stretching frequency of  $\nu_{CN}$  which would be expected if Au-Au interactions are invoked.

In order to test their response in the solid state to ammonia vapor, the coordination polymers were ground using an agate mortar and pestle to increase reactive surface area. The sample was transferred to a one-dram vial and spiked using a glass pasteur pipette with the concentrated headspace of a bottle of 28-30% ammonia hydroxide in water solution and sealed. Subsequently, a test strip wetted with ammonium hydroxide solution was introduced to the sealed system and allowed to sit for ten minutes to promote full conversion of the native materials to their ammoniated forms. This spiking was repeated and the ammoniation process tracked by monitoring the shift of  $\nu_{CN}$ . Prior to spectroscopic analysis, the samples were allowed to air-dry permitting excess ammonia vapors to escape. The samples were maintained in an ammoniated atmosphere prior to combustion analysis. Spectroscopic results for the ammoniated species have been included at the end of this chapter.

### **3.2.5 Luminescence Analysis of $\text{Ph}_4\text{AsMX}[\text{Au}(\text{CN})_2]_2$ and $\text{Ph}_4\text{AsMX}_2[\text{Au}(\text{CN})_2]$ Ammoniated Materials**

Attempts were made to elucidate the structure of the ammoniated species. The systems were synthesized under concentrated atmospheres of ammonia vapours through both bench-top slow evaporation techniques and solvothermal reactions. Additionally, ammonium hydroxide solution was added to the ethanolic reaction mix during crystal growth or the final crystals subjected to ammonia vapour exposure. These experiments were done in hopes that ammonia would be incorporated into the solid-state structure. All of the attempts failed to produce the desired result. The incorporation appears to be a bulk effect since there is complete shifting of the cyanide stretching frequencies as observed by IR and Raman spectroscopy. The difficulties in getting a structural determination may arise if the structural rearrangement is drastic. This hypothesis is supported by the visual observation that exposure to concentrated ammonia vapours leads to an

immediate loss of crystallinity. Growing the system in ammonium hydroxide solution tended to produce complex ions with coordinated ammonia. None-the-less, vivid luminescence response was noted upon exposure of the crystal systems to ammonia vapours in the solid state and their luminescence is analyzed in this section.

All materials exhibited an almost instantaneous response when exposed to concentrated headspace of a 28-30% ammonium hydroxide in water solution leading to the formation of luminescent green powders with wide excitation bands ranging from 300-450 nm and emission maxima at approximately 500 nm, consistent with Au(I)-based fluorescence (Tables 3.1 & 3.2).<sup>69</sup> The largest deviations were seen in  $\text{Ph}_4\text{AsZnBr}_2[\text{Au}(\text{CN})_2]$  and  $\text{Ph}_4\text{AsCdCl}[\text{Au}(\text{CN})_2]_2$  which exhibited emission maxima at 469 and 525 nm respectively. Comparing the  $[\text{Ph}_4\text{P}]^+$  and  $[\text{Ph}_4\text{As}]^+$  analogues,  $\text{Ph}_4\text{PCdCl}[\text{Au}(\text{CN})_2]_2$  displayed an emission maxima at 511 nm when excited at 420 nm which is blue-shifted 14 nm compared to the emission maxima of 525 nm observed of  $\text{Ph}_4\text{AsCdCl}[\text{Au}(\text{CN})_2]_2$  when excited at 400 nm.  $\text{Ph}_4\text{PZnBr}_2[\text{Au}(\text{CN})_2]$  has an emission maxima of 486 nm when excited at 356 nm, a red-shift of 17 nm compared to the maxima of 469 nm observed of  $\text{Ph}_4\text{AsZnBr}_2[\text{Au}(\text{CN})_2]$  when excited at 349 nm. Only a single emission peak was observed for both the  $[\text{Ph}_4\text{P}]^+$  and  $[\text{Ph}_4\text{As}]^+$  CPs post ammoniation (Figures 3.7-3.9.).

Table 3.1. Summary of Luminescence Data at 298 K for [Ph<sub>4</sub>As]<sup>+</sup> compounds.

Topology	Compound	Excitation $\lambda_{\text{max}}(\text{nm})$	Emission $\lambda_{\text{max}}(\text{nm})$	Quantum Yield (%)
2-D	Ph <sub>4</sub> AsZnCl[Au(CN) <sub>2</sub> ] <sub>2</sub>	337	390	27
	(Ammoniated)	387	503	<b>86</b>
1-D	Ph <sub>4</sub> AsZnBr <sub>2</sub> [Au(CN) <sub>2</sub> ]	299	487	16
	(Ammoniated)	349	469	17
2-D	Ph <sub>4</sub> AsCdCl[Au(CN) <sub>2</sub> ] <sub>2</sub>	299	492	28
	(Ammoniated)	400	525	<b>84</b>
2-D	Ph <sub>4</sub> AsCdBr[Au(CN) <sub>2</sub> ] <sub>2</sub>	299	499	34
	(Ammoniated)	380	505	23

Table 3.2. Summary of Luminescence Data at 298 K for [Ph<sub>4</sub>P]<sup>+</sup> compounds.

Topology	Compound	Excitation $\lambda_{\text{max}}(\text{nm})$	Emission $\lambda_{\text{max}}(\text{nm})$
1-D	Ph <sub>4</sub> PZnBr <sub>2</sub> [Au(CN) <sub>2</sub> ]	400	490
	(Ammoniated)	490	400
	(Thermally Annealed)	330	470
2-D	Ph <sub>4</sub> PCdCl[Au(CN) <sub>2</sub> ] <sub>2</sub>	291	505
	(Ammoniated)	401	511

Two different states of ammoniation were observed with all the synthesized polymers which is analogous to the situation that was seen for Zn[Au(CN)<sub>2</sub>]<sub>2</sub>. The fully saturated compounds, which were analyzed immediately after their removal from the ammoniated atmosphere, exhibited different spectroscopic properties compared to the unsaturated states which are presumed to form over time. The fully saturated state is transient, and after a short period of time, will convert to the first ammoniated state via shedding of bound ammonia. This can be observed by assessing the real time fluorescence profile on the fluorimeter. Due to the short lived nature of this fully saturated state, fluorescence data was not collected.

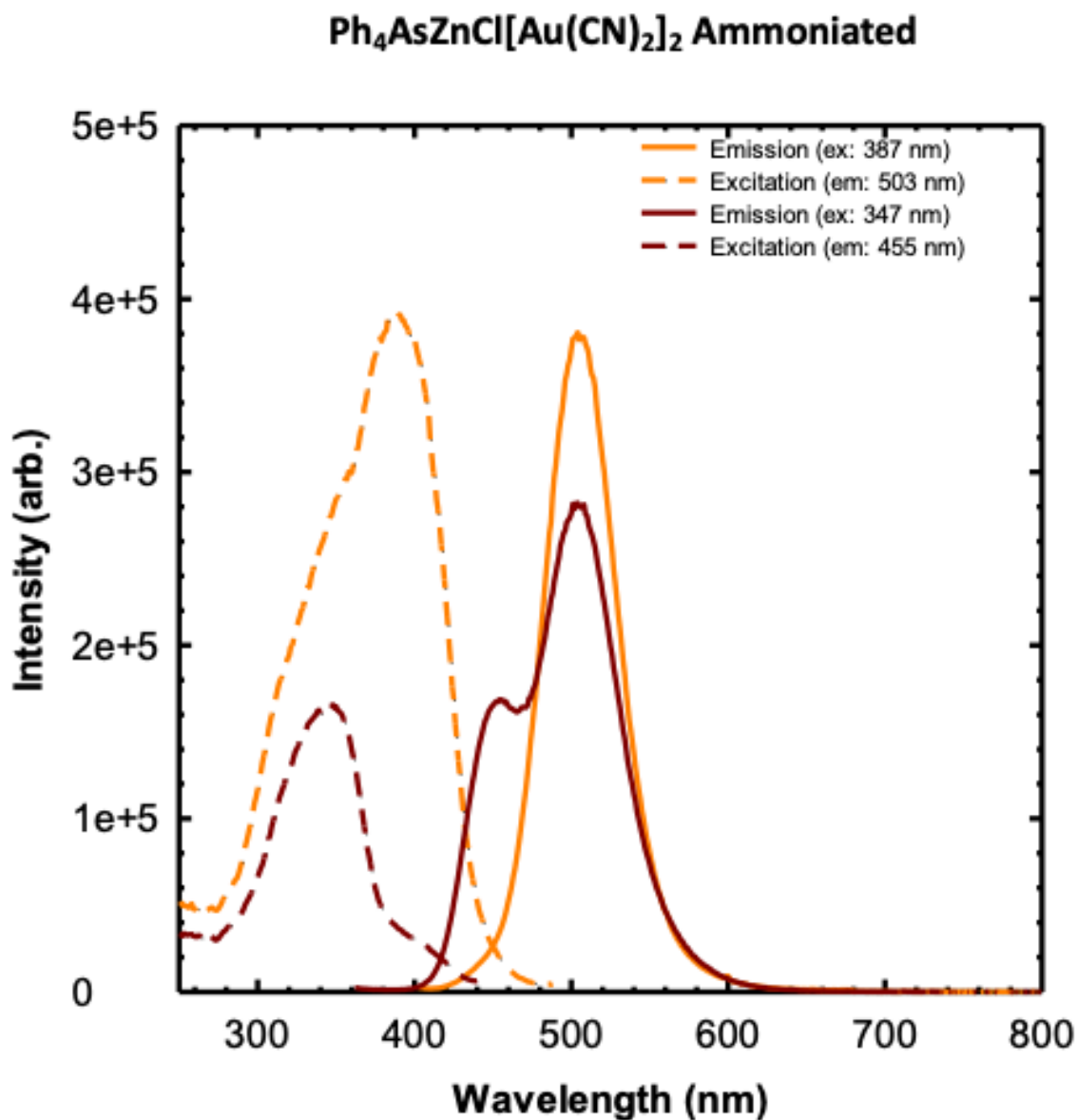


Figure 3.7. Solid-state luminescence spectra of  $\text{Ph}_4\text{AsZnCl}[\text{Au}(\text{CN})_2]_2$  post ammonia exposure.

Data collected at room temperature after the sample had been exposed to concentrated ammonia vapor. The sample was not contained under a concentrated ammonia atmosphere.

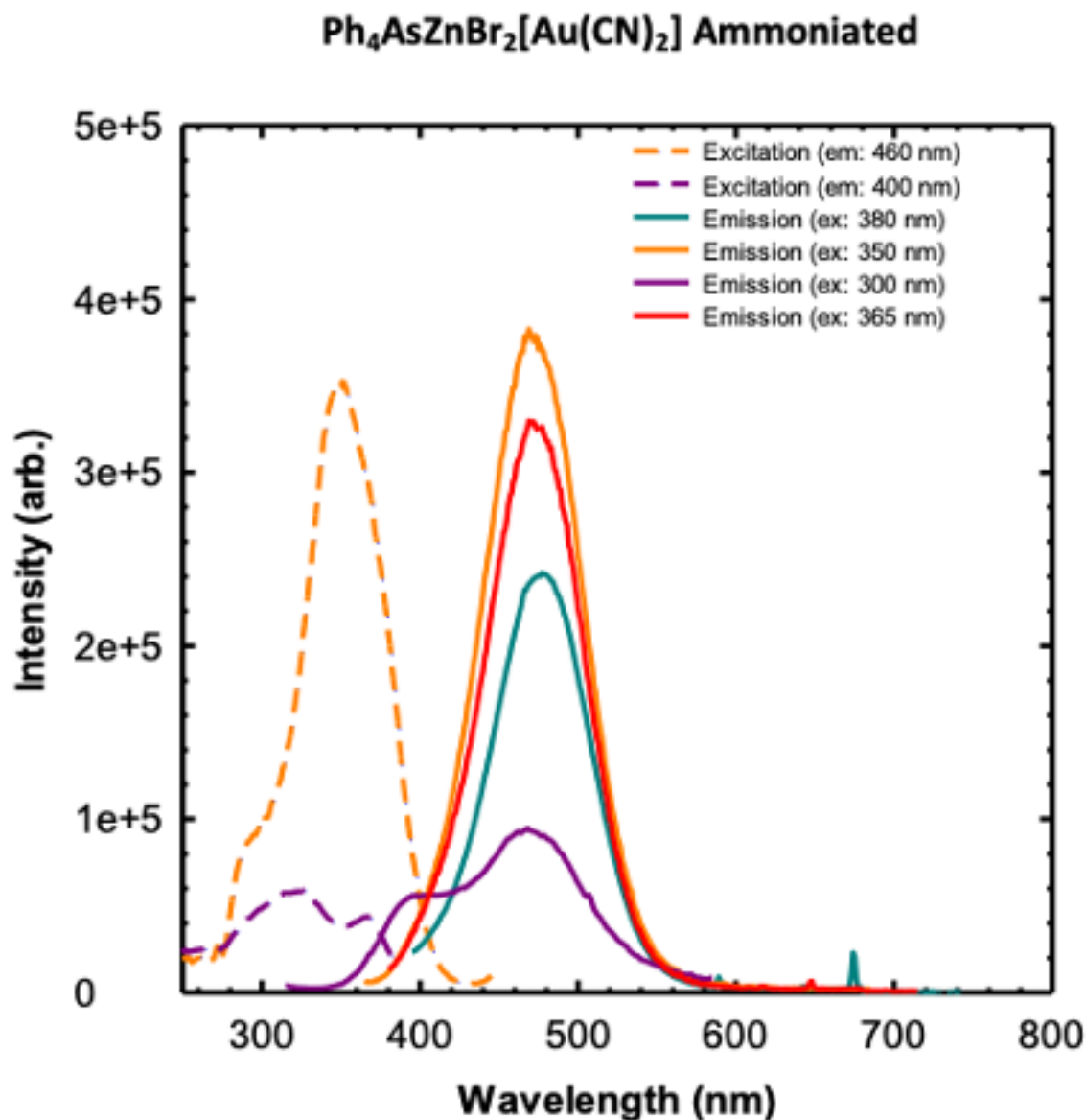


Figure 3.8. Solid-state luminescence spectra of  $\text{Ph}_4\text{AsZnBr}_2[\text{Au}(\text{CN})_2]$  post ammonia exposure.

Data collected at room temperature after the sample had been exposed to concentrated ammonia vapor. The sample was not contained under a concentrated ammonia atmosphere.

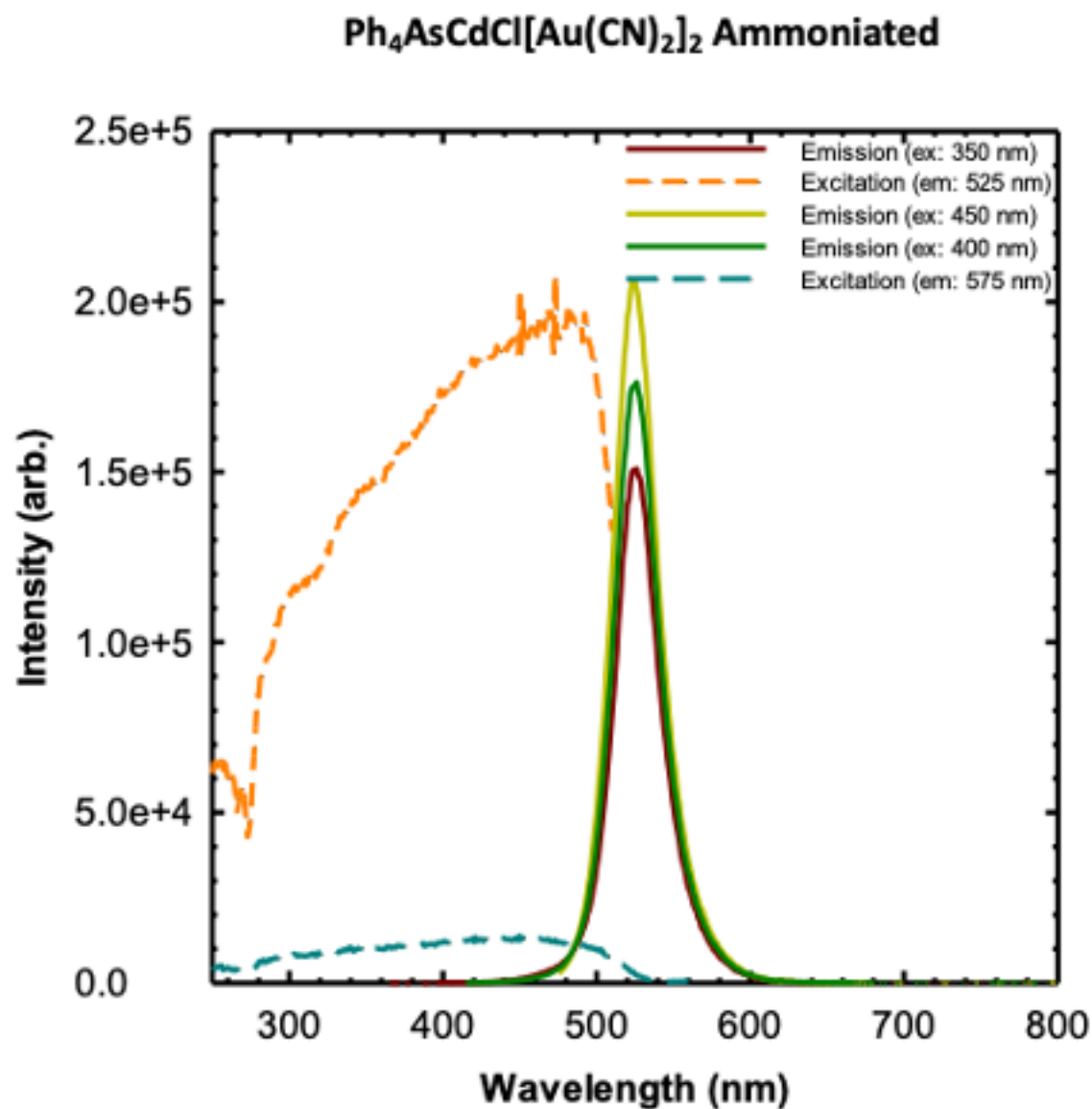


Figure 3.9. Solid-state luminescence spectra of  $\text{Ph}_4\text{AsCdCl}[\text{Au}(\text{CN})_2]_2$  post ammonia exposure.

Data collected at room temperature after the sample had been exposed to concentrated ammonia vapor. The sample was not contained under a concentrated ammonia atmosphere.



### 3.2.6 Quantum Yield Analysis

The emission intensity for the bromine and chlorine samples varied substantially upon visual examination under broadband UV-light. As such, the differences were quantified through quantum yield measurements. The  $[\text{Ph}_4\text{As}]^+$  containing compounds displayed quantum yields ranging from 16-34% in their native state. Upon ammoniation, this range became 17-86%. Considering the metals, there is no apparent difference between the zinc and cadmium compounds. However, it appears that the chlorine containing materials display a much more vivid response compared to the bromine.  $\text{Ph}_4\text{AsZnCl}[\text{Au}(\text{CN})_2]_2$  and  $\text{Ph}_4\text{AsCdCl}[\text{Au}(\text{CN})_2]_2$  both exhibit a threefold increase in quantum yield upon ammoniation.  $\text{Ph}_4\text{AsZnBr}_2[\text{Au}(\text{CN})_2]$  and  $\text{Ph}_4\text{AsCdBr}[\text{Au}(\text{CN})_2]_2$  exhibit a minimal response to ammonia. In comparing the 1-D or 2-D structures, it does not appear that one nor the other exhibits a stronger response.  $\text{Ph}_4\text{AsCdBr}[\text{Au}(\text{CN})_2]_2$  which is 2-D does not exhibit the same increase in fluorescence seen in  $\text{Ph}_4\text{AsZnCl}[\text{Au}(\text{CN})_2]_2$ . It appears that the presence of chlorine is important for the enhanced response. One rationale for this can be differences in bond polarization seen in metal-chlorine vs. metal-bromine bonds. The slight differences in electronegativity between chlorine and bromine may render the chlorine variant a more reactive form over the bromine due to increased attraction of the metal center for Lewis donors such as ammonia. The results are summarized in Table 3.1.

### 3.2.7 Reversibility, Limit of Detection, Thermogravimetric Analysis

#### Selectivity

One candidate from each structural motif,  $[\text{TPA}]\text{CdCl}[\text{Au}(\text{CN})_2]_2$  and  $[\text{TPA}]\text{ZnBr}_2[\text{Au}(\text{CN})_2]$ , was screened for selectivity toward ammonia by assessing their response toward other amines. Various amine vapours were applied in the gas phase to solid samples of the CPs, the samples sealed, and subsequently they were viewed under a broad-band UV-lamp. The results are summarized below.

Table 3.3. Qualitative Response of [TPA]CdCl[Au(CN)<sub>2</sub>]<sub>2</sub> and [TPA]ZnBr<sub>2</sub>[Au(CN)<sub>2</sub>]<sub>2</sub> to Amine Vapours

[TPA]CdCl[Au(CN) <sub>2</sub> ] <sub>2</sub>		[TPA]ZnBr <sub>2</sub> [Au(CN) <sub>2</sub> ] <sub>2</sub>	
Analyte	Response	Analyte	Response
Diethylamine	orange/yellow, dim	Diethylamine	orange/yellow, dim
Ethylenediamine	N	Ethylenediamine	N
Butylamine	N	Butylamine	N
Pyridine	blue, dim	Pyridine	blue, dim
Methylamine (40% aq)	blue, bright	Methylamine (40% aq)	blue, dim
Triethylamine	N	Triethylamine	blue, dim
Tributylamine	N	Tributylamine	blue, dim
Propylamine	N	Propylamine	N
Sec-butylamine	N		

The responses towards other amines, assessed visually, are much weaker and has a sufficiently different colour compared to ammonia. As such, it can be concluded that these materials are reasonably selective towards gaseous ammonia. Selectivity seen towards ammonia can be the result of steric considerations. Bulkier amines do not appear to invoke a response. However, if structural rearrangement is being invoked through bonding of the analyte to a five-coordinate metal center, the influence of sterics should be mitigated. Another consideration that can lead to the response towards ammonia can be the higher vapour pressure of this analyte compared to the other amines surveyed.

### Thermogravimetric Analysis

Thermogravimetric analysis (TGA) was performed at 2°C per minute using a TGA-50 Shimadzu thermogravimetric analyzer on [Ph<sub>4</sub>As]CdCl[Au(CN)<sub>2</sub>]<sub>2</sub> and [Ph<sub>4</sub>As]ZnBr<sub>2</sub>[Au(CN)<sub>2</sub>]<sub>2</sub> (Figure 3.10.-3.11.) to assess thermal stability and the prospect of using these materials as a reversible sensor for ammonia. At room temperature, stable ammonia adducts can be isolated post-exposure.

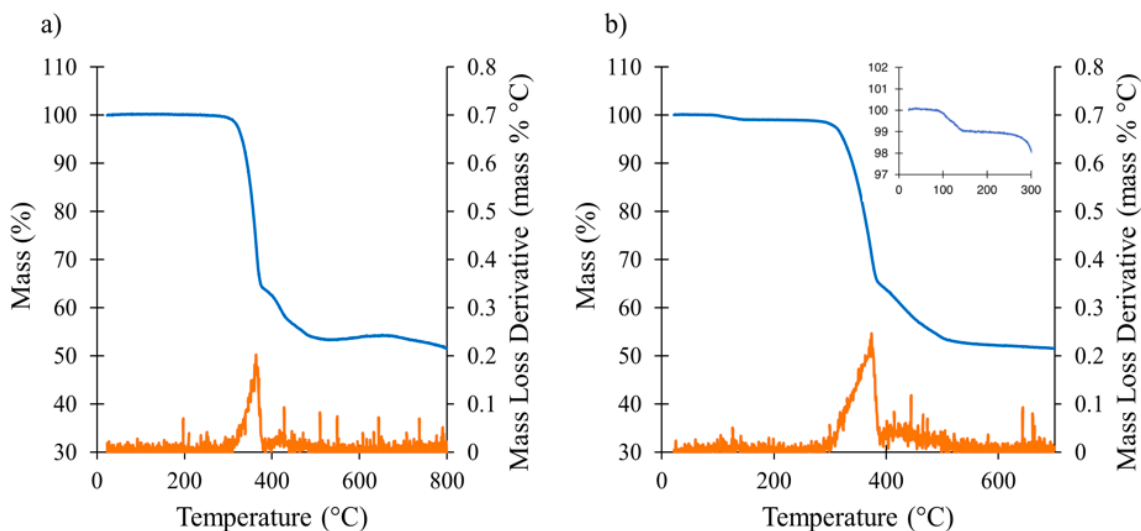


Figure 3.10. TGA thermograms of  $[\text{Ph}_4\text{As}]\text{CdCl}[\text{Au}(\text{CN})_2]_2$  a) before and b) after exposure to  $\text{NH}_3$  with temperature inset from 0 to  $300^\circ\text{C}$ .

Decomposition of  $[\text{Ph}_4\text{As}]\text{CdCl}[\text{Au}(\text{CN})_2]_2$  begins at  $\sim 300^\circ\text{C}$ . Exposing this material to concentrated  $\text{NH}_3$  vapours followed by the subsequent removal from this atmosphere led to an observable mass loss event from  $\sim 95^\circ\text{C}$  to  $\sim 150^\circ\text{C}$  which can be attributed to the loss of bound ammonia. This loss event results in a roughly 0.93% decrease in total mass, in comparison to the calculated value for one bound  $\text{NH}_3$  of 1.63%. This difference can arise from incomplete saturation that would result if the ammonia only interacts with the surface of the CP or because of lability in the ammoniated adduct upon removal from the concentrated ammonia atmosphere. The emission intensity of the ammoniated material was assessed at 513 nm. Subsequently, the material was placed in an oven at  $160^\circ\text{C}$  for 45 minutes after which the intensity was reassessed. It was found that the response can be reversed, back to the emission profile observed in the native state, allowing this material to function as a reversible sensor for high concentrations of ammonia.

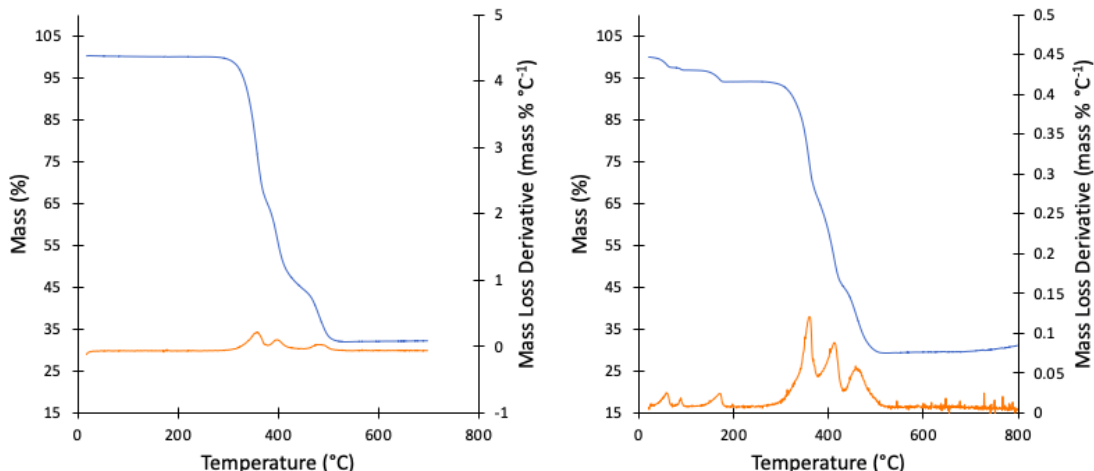


Figure 3.11. TGA thermograms of  $[\text{Ph}_4\text{As}]\text{ZnBr}_2[\text{Au}(\text{CN})_2]$  (left) before and (right) after exposure to  $\text{NH}_3$ .

Decomposition of  $[\text{Ph}_4\text{As}]\text{ZnBr}_2[\text{Au}(\text{CN})_2]$  begins at  $\sim 295^\circ\text{C}$ . Exposing this material to concentrated  $\text{NH}_3$  vapours followed by the subsequent removal from this atmosphere led to the observation of three mass loss events. The first one occurs from around  $22 - 70^\circ\text{C}$ , the second from  $84 - 95^\circ\text{C}$ , and the third from  $132 - 183^\circ\text{C}$ . The total % mass associated with these events is 5.61 % which is in agreement with the 5.65 % calculated mass loss for three equivalents of ammonia. This observation suggests that the 1-D chain motif is able to bind ammonia in different ways to obtain a variety of saturation states. This can perhaps be rationalized by the fact that  $\text{Zn}(\text{II})$ , in the structure, is 4-coordinate as opposed to the 5-coordinate  $\text{Cd}$  in  $[\text{Ph}_4\text{As}]\text{CdCl}[\text{Au}(\text{CN})_2]_2$  which allows the  $\text{Zn}$  to have a more promiscuous coordination sphere.

### Limit of Detection

The CPs were ground and drop-casted using ethanol onto a glass slide which was placed into a quartz cuvette. The cuvette was subsequently placed underneath the optical probe of an Ocean Optics Flame Spectrometer and excited using a DH-2000 light source equipped with a deuterium lamp passed through a Thorlabs 275-375 nm shortpass filter. Calibrated standards of ammonia gas were then fed into

the cuvette through a gas line and the emission monitored in real time for a half hour.

$\text{Ph}_4\text{AsCdCl}[\text{Au}(\text{CN})_2]_2$ ,  $\text{Ph}_4\text{AsZnCl}[\text{Au}(\text{CN})_2]_2$ ,  $\text{Ph}_4\text{AsZnBr}_2[\text{Au}(\text{CN})_2]$ ,  $\text{Ph}_4\text{PCdCl}[\text{Au}(\text{CN})_2]_2$ , and  $\text{Ph}_4\text{ZnBr}_2[\text{Au}(\text{CN})_2]$  were selected to probe the sensitivity of this family of CP toward gaseous ammonia. These were selected to account for the different combinations of metal nodes, cations, halides, and structural motifs (1-D vs 2-D) that are possible in this family of CPs. No emission or IR absorption changes suggestive of ammonia uptake were noted at either 50 nor 1000 ppm concentrations balanced in air and nitrogen respectively. This leads to the conclusion that although a very strong luminescent response is invoked in this class of CP upon ammonia binding, it is only sensitive to the very high concentrations of ammonia observed in the headspace of a 28-30% ammonia hydroxide bottle. Efforts should be taken to improve the sensitivity of these materials towards ammonia. One such way can be changing the temperature of the environment which may lead to slight morphological differences that make the material more sensitive.

### **Uptake Kinetics**

To address the possibility that the limit of detection experiments did not allow enough time for ammonia to be taken up, the CPs were contained in static and dynamic atmospheres of 1000 ppm  $\text{NH}_3$  for two weeks and 12 hrs respectively.  $\text{Ph}_4\text{AsCdCl}[\text{Au}(\text{CN})_2]_2$  and  $\text{Ph}_4\text{AsZnCl}[\text{Au}(\text{CN})_2]_2$  were contained in individual 1-dram vials. These vials were transferred to a 1-litre round bottom flask previously purged with 1000 ppm ammonia after which the flask was sealed to preserve the ammoniated atmosphere. The samples were periodically removed and checked over a period of two weeks through FT-IR, Raman, and fluorescence spectroscopy to assess for uptake of ammonia over prolonged exposure to a concentrated environment. The containment flask was re-purged with 1000 ppm ammonia prior to replacement of the sample vial. Additionally, samples of the native materials were exposed to a constant flow of 1000 ppm ammonia over a period of 12 hours

and its emission monitored using the same set up with the Ocean Optics Flame Spectrometer in the limit of detection studies.

No response suggestive of ammonia uptake was observed through any of the methods over the monitoring period.

### Screening other S- and O- Analytes

One candidate from each structural motif,  $[\text{Ph}_4\text{As}]\text{CdCl}[\text{Au}(\text{CN})_2]_2$  (2-D sheet) and  $[\text{Ph}_4\text{As}]\text{ZnBr}_2[\text{Au}(\text{CN})_2]$  (1-D chain) were qualitatively screened for sensing capabilities toward a variety of sulfur and oxygen donors in the gas phase. The results are summarized below.

Table 3.4. Qualitative Response of  $[\text{TPA}]\text{CdCl}[\text{Au}(\text{CN})_2]_2$  and  $[\text{TPA}]\text{ZnBr}_2[\text{Au}(\text{CN})_2]$  to Sulfur and Oxygen Donors

$[\text{TPA}]\text{CdCl}[\text{Au}(\text{CN})_2]_2$		$[\text{TPA}]\text{ZnBr}_2[\text{Au}(\text{CN})_2]$	
Analyte	Response	Analyte	Response
Diethylsulfide	N	Diethylsulfide	Orange, dim
1-butanethiol	N	1-butanethiol	Orange, dim
Thiophenol	N	Thiophenol	N
Tetrahydrothiophene	N	Tetrahydrothiophene	N
DMSO	N	DMSO	N
MeOH	N	MeOH	N
Acetone	N	Acetone	N
Ether	N	Ether	N

It was initially expected that  $[\text{Ph}_4\text{As}]\text{CdCl}[\text{Au}(\text{CN})_2]_2$  could show response towards sulfides and thiols in accordance with hard-soft acid-base (HSAB) theory which suggests that soft metal nodes like Cd(II) would preferentially bind soft donor (sulfur) analytes. However, no response (N in the table refers to no change in emission colour) is seen from  $[\text{Ph}_4\text{As}]\text{CdCl}[\text{Au}(\text{CN})_2]_2$  towards the screened analytes. Dim, orange emission was initially noted upon exposure of  $[\text{Ph}_4\text{As}]\text{ZnBr}_2[\text{Au}(\text{CN})_2]$  to diethylsulfide and 1-butanethiol. The results were not reproducible and may have been the result of contamination in the analytes but should be investigated further after confirming the purity of the materials through  $^1\text{H-NMR}$ .

### 3.2.8 Conclusions and Future Directions

Coordination polymers incorporating group 12 metal halides, cations;  $[\text{Ph}_4\text{As}]^+$  or  $[\text{Ph}_4\text{P}]^+$ , and dicyanoaurate of the form  $[\text{Ph}_4\text{As}]/[\text{Ph}_4\text{P}]\text{MX}[\text{Au}(\text{CN})_2]_2$  (2-D pleated sheet) and  $[\text{Ph}_4\text{As}]/[\text{Ph}_4\text{P}]\text{MX}_2[\text{Au}(\text{CN})_2]$  (1-D anionic chain) have been synthesized, structurally characterized, and their ammonia-sensing capabilities assessed. Both of these crystal forms experience an enhancement and shift in luminescent response after exposure to concentrated ammonia vapors. The response was particularly vivid for the 2-D sheets, which exhibited quantum yields for the ammoniated species in excess of 85%. The response of  $\text{Ph}_4\text{AsCdCl}[\text{Au}(\text{CN})_2]_2$  was cycled and deemed to be reversible. However, the cycling temperature should be increased in future studies of the 1-D family since mass loss events are seen to occur upwards of 185°C. TGA analysis can be coupled with mass spectrometry to affirm the identity of the species coming off. The materials are only sensitive towards high concentrations of ammonia. Future efforts can be dedicated towards investigating whether the limit of detection can be reduced.

## 3.3 Experimental

### 3.3.1 General Methods and Materials

All reactions were conducted in air. All reagents were obtained from commercial sources and used as received except for  $\text{Ph}_4\text{As}[\text{Au}(\text{CN})_2]$  and  $\text{Ph}_4\text{P}[\text{Au}(\text{CN})_2]$  which were produced through metathesis reactions of  $\text{K}[\text{Au}(\text{CN})_2]$  and  $\text{Ph}_4\text{AsCl}$  or  $\text{Ph}_4\text{PCl}$  in water and methanol respectively. IR spectra were recorded on a Thermo Nicolet Nexus 670 FTIR spectrometer equipped with a Pike MIRacle attenuated total reflection (ATR) sampling accessory with a Ge crystal. Raman spectra were recorded on a Renishaw inVia Raman Microscope equipped with a 200 mW 785 nm laser. Spectra were obtained from 100 to 3200  $\text{cm}^{-1}$  using a 1200 l/mm (633/780) grating for an exposure time of 10 seconds. Specific accumulations and % laser power are stated for each experiment. Raman was not collected for the

post-ammoniated species due to interference from the intense fluorescence. Microanalyses (C, H, N) were performed by Paul Mulyk and Wen Zhou at Simon Fraser University on a Carlo Erba EA 1100 CHN elemental analyzer. Thermogravimetric analysis (TGA) was performed using a TGA-50 Shimadzu thermogravimetric analyzer on  $[\text{Ph}_4\text{As}]\text{CdCl}[\text{Au}(\text{CN})_2]_2$  and  $[\text{Ph}_4\text{As}]\text{ZnBr}_2[\text{Au}(\text{CN})_2]$ . Emission spectra were collected on a Edinburgh FS5 Spectrofluorometer using a xenon arc lamp. Experimental specifications were 1 nm excitation and emission slit widths, 0.1 – 0.5 second dwell times, and 1 – 2 averaged scans per spectra. Limit of detection studies were carried through dynamic monitoring of emission. This technique is summarized in 1.3.2.

### 3.3.2 Single crystal X-ray diffraction structure determinations

Structure determinations were done identically to the materials described in Chapter 2. Additional crystallographic information can be found in Appendix A. Selected bond lengths and angles are displayed in Appendices B3 through B5.

### 3.3.3 Synthetic Procedures

The  $[\text{Ph}_4\text{P}]^+$  cation was also used in place of  $[\text{Ph}_4\text{As}]^+$  in each of the two structural forms to mitigate the toxicity concerns of using arsenic containing materials.  $[\text{Ph}_4\text{P}]\text{Au}(\text{CN})_2$  and  $[\text{Ph}_4\text{As}]\text{Au}(\text{CN})_2$  were synthesized in quantitative yields through the salt metathesis of stoichiometric amounts of tetraphenylphosphonium chloride and tetraphenylarsonium chloride with potassium dicyanoaurate in methanol and water respectively. Anal. Calcd for  $\text{C}_{24}\text{H}_{20}\text{As}[\text{Au}(\text{CN})_2]$ : C, 49.39 %; H, 3.19 %; N, 4.43 %. Found: C, 49.87 %; H, 3.28 %; N, 4.47 %. Anal. Calcd for  $\text{C}_{24}\text{H}_{20}\text{P}[\text{Au}(\text{CN})_2]$ : C, 53.07 %; H, 3.43 %; N, 4.76 %. Found: C, 52.77 %; H, 3.65 %; N, 4.79 %.

#### **$\text{Ph}_4\text{AsZnCl}[\text{Au}(\text{CN})_2]_2$**



ZnCl<sub>2</sub> (14 mg, 0.10 mmol) and Ph<sub>4</sub>As[Au(CN)<sub>2</sub>] (125 mg, 0.20 mmol) were dissolved in 5 and 3 mL of EtOH respectively. The ethanolic zinc solution was added dropwise to the gold solution creating a cloudy white mix. The resulting solution was allowed to slow evaporate overnight producing large colorless block crystals which were collected through vacuum filtration and rinsed with cold ethanol. Yield: 29 mg (29 %). FT-IR (ATR, cm<sup>-1</sup>): 3054 vw, 2191 ( $\nu_{CN}$ , s), 1579 w, 1482 m, 1439 s, 1337 w, 1310 w, 1261 w, 1187 w, 1159 w, 1082 s, 998 s, 848 w, 744 vs. Raman (514 nm, %Ip: 5, cm<sup>-1</sup>): 3057 s, 2198 ( $\nu_{CN}$ , s), 1577 m, 1179 w, 1161 w, 1082 w, 1021 w, 1000 m, 668 w, 614 w, 361 w, 231 w, 187 w, 107 s. Anal. Calcd for C<sub>24</sub>H<sub>20</sub>AsZnCl[Au(CN)<sub>2</sub>]<sub>2</sub>: C, 34.24 %; H, 2.05 %; N, 5.70 %. Found: C, 34.31 %; H, 2.07 %; N, 5.72 %.

#### **Ph<sub>4</sub>AsCdCl[Au(CN)<sub>2</sub>]<sub>2</sub>**

CdCl<sub>2</sub> (18 mg, 0.10 mmol) and Ph<sub>4</sub>As[Au(CN)<sub>2</sub>] (126 mg, 0.20 mmol) were dissolved in 5 and 3 mL of EtOH respectively. The ethanolic cadmium solution was added dropwise to the gold solution with immediate nucleation of crystals noticed. The resulting solution was allowed to slow evaporate overnight after which colorless needle crystals were collected through vacuum filtration and rinsed with cold ethanol. Yield: 36 mg (35 %). FT-IR (ATR, cm<sup>-1</sup>): 3079 vw, 3055 vw, 2179 ( $\nu_{CN}$ , vs), 1480 m, 1439 s, 1338 w, 1310 w, 1184 w, 1161 w, 1080 s, 1022 w, 997 m, 849 w, 746 vs. Raman (514 nm, %Ip: 10, cm<sup>-1</sup>): 3147 w, 3056 s, 2196 ( $\nu_{CN}$ , s), 1577 w, 1183 w, 1158 w, 1081 w, 1021 w, 1000 m, 668 w, 613 w, 330 w, 234 w, 185 w. Anal. Calcd for C<sub>24</sub>H<sub>20</sub>AsCdCl[Au(CN)<sub>2</sub>]<sub>2</sub>: C, 32.68 %; H, 1.96 %; N, 5.44 %. Found: C, 32.93 %; H, 1.70 %; N, 5.47 %.

#### **Ph<sub>4</sub>AsCdBr[Au(CN)<sub>2</sub>]<sub>2</sub>**

CdBr<sub>2</sub> (27 mg, 0.10 mmol) and Ph<sub>4</sub>As[Au(CN)<sub>2</sub>] (126 mg, 0.20 mmol) were dissolved in 5 and 3 mL of EtOH respectively. The ethanolic cadmium solution was added dropwise to the gold solution with immediate nucleation of crystals noticed. The resulting solution was allowed to slow evaporate overnight after which colorless needle crystals were collected through vacuum filtration and rinsed with

cold ethanol. Yield: 81 mg (81 %). FT-IR (ATR,  $\text{cm}^{-1}$ ): 3083 vw, 3055 vw, 2178 ( $\nu_{\text{CN}}$ , vs), 1573 w, 1480 m, 1439 s, 1338 w, 1310 w, 1261 w, 1184 w, 1160 w, 1080 m, 1023 w, 997 m, 746 vs. Raman (514 nm, %lp: 10,  $\text{cm}^{-1}$ ): 3158 w, 3057 s, 2195 ( $\nu_{\text{CN}}$ , s), 1578 w, 1184 w, 1163 w, 1082 w, 1021 w, 1000 s, 669 w, 614 w, 236 w, 186 w. Anal. Calcd for  $\text{C}_{24}\text{H}_{20}\text{AsCdBr}[\text{Au}(\text{CN})_2]_2$ : C, 31.32 %; H, 1.88 %; N, 5.22 %. Found: C, 31.64 %; H, 2.14 %; N, 5.06 %.

### **$\text{Ph}_4\text{PCdCl}[\text{Au}(\text{CN})_2]_2$**

$\text{CdCl}_2$  (18 mg, 0.10 mmol) and  $\text{Ph}_4\text{P}[\text{Au}(\text{CN})_2]$  (117 mg, 0.20 mmol) were dissolved in 5 and 3 mL of EtOH respectively. The ethanolic cadmium solution was added dropwise to the gold solution with immediate nucleation of crystals noticed. The resulting solution was allowed to slow evaporate overnight after which colorless needle crystals were collected through vacuum filtration and rinsed with cold ethanol. Yield: 57 mg (58 %). FT-IR (ATR,  $\text{cm}^{-1}$ ): 2177 ( $\nu_{\text{CN}}$ , s), 1584 w, 1480 w, 1435 m, 1339 w, 1313 w, 1161 w, 1105 vs, 1028 w, 996 m, 754 s, 722 vs. Raman (514 nm, %lp: 5,  $\text{cm}^{-1}$ ): 3060 s, 2196 ( $\nu_{\text{CN}}$ , s), 1585 m, 1184 w, 1163 w, 1097 w, 1023 w, 1000 s, 725 w, 678 w, 615 w, 329 w, 250 w, 197 w, 105 s. Anal. Calcd for  $\text{C}_{24}\text{H}_{20}\text{PCdCl}[\text{Au}(\text{CN})_2]_2$ : C, 34.13 %; H, 2.05 %; N, 5.69 %. Found: C, 34.11 %; H, 2.14 %; N, 5.41 %.

### **$\text{Ph}_4\text{AsZnBr}_2[\text{Au}(\text{CN})_2]$**

$\text{ZnBr}_2$  (22 mg, 0.10 mmol) and  $\text{Ph}_4\text{As}[\text{Au}(\text{CN})_2]$  (63 mg, 0.10 mmol) were dissolved in 5 and 3 mL of EtOH respectively. The ethanolic zinc solution was added dropwise to the gold solution, creating a cloudy white mix. The resulting solution was allowed to slow evaporate overnight, producing colorless granular crystals which were collected through vacuum filtration and rinsed with cold ethanol. Yield: 40 mg (47.0 %). FT-IR (ATR,  $\text{cm}^{-1}$ ): 2206 ( $\nu_{\text{CN}}$ , w), 2186 ( $\nu_{\text{CN}}$ , m), 1482 w, 1438 m, 1335 w, 1307 w, 1261 w, 1184 w, 1081 m, 1016 w, 997 m, 748 s, 740 vs. Raman (514 nm, %lp: 10,  $\text{cm}^{-1}$ ): 3056 m, 2212 ( $\nu_{\text{CN}}$ , m), 1580 w, 1018 w, 1001 s, 671 w, 613 w, 237 w, 103 s. Anal. Calcd for  $\text{C}_{24}\text{H}_{20}\text{AsZnBr}_2[\text{Au}(\text{CN})_2]$ : C, 36.42 %; H, 2.35 %; N, 3.27 %. Found: C, 36.48 %; H, 2.39 %; N, 3.34 %.

### **Ph<sub>4</sub>AsZnI<sub>2</sub>[Au(CN)<sub>2</sub>]**

ZnI<sub>2</sub> (32 mg, 0.10 mmol) and Ph<sub>4</sub>As[Au(CN)<sub>2</sub>] (63 mg, 0.10 mmol) were dissolved in 5 and 3 mL of EtOH respectively. The ethanolic zinc solution was added dropwise to the gold solution yielding a yellow mix which was allowed to slow evaporate overnight producing pale yellow granular crystals. These crystals were collected through vacuum filtration and rinsed with cold ethanol. Yield: 13 mg (13 %). FT-IR (ATR, cm<sup>-1</sup>): 3504 vw, 2188 ( $\nu_{CN}$ , vs), 1482 m, 1439 s, 1336 w, 1308 w, 1185 w, 1081 s, 1015 w, 997 s, 740 vs. Raman (514 nm, %lp: 5, cm<sup>-1</sup>): 3055 s, 2212 ( $\nu_{CN}$ , m), 1579 w, 1082 w, 1018 w, 1001 m, 670 w, 612 w, 235 w, 180 w. Anal. Calcd for C<sub>24</sub>H<sub>20</sub>PZnI<sub>2</sub>[Au(CN)<sub>2</sub>]: C, 32.82 %; H, 2.12 %; N, 2.94 %. Found: C, 32.92 %; H, 2.13 %; N, 2.91 %.

### **Ph<sub>4</sub>PZnBr<sub>2</sub>[Au(CN)<sub>2</sub>]**

ZnBr<sub>2</sub> (22 mg, 0.10 mmol) and Ph<sub>4</sub>P[Au(CN)<sub>2</sub>] (58 mg, 0.10 mmol) were dissolved in 5 and 3 mL of EtOH respectively. The ethanolic zinc solution was added dropwise to the gold solution, resulting in immediate nucleation of colorless granular crystals. The resulting solution was allowed to slow evaporate overnight, after which the crystals were collected through vacuum filtration and rinsed with cold ethanol. Yield: 31 mg (38 %). FT-IR (ATR, cm<sup>-1</sup>): 3054 vw, 2212 w, 2190 s ( $\nu_{CN}$ , s), 1586 w, 1483 w, 1435 w, 1384 w, 1339 w, 1313 w, 1261 w, 1189 w, 1162 w, 1162 w, 1110 vs, 1025 w, 997 m, 761 m, 751 m, 724 vs. Raman (514 nm, %lp: 1, cm<sup>-1</sup>): 3057 s, 2213 ( $\nu_{CN}$ , s), 1587 m, 1099 m, 1021 m, 1001 s, 680 w, 614 w, 327 w, 290 w, 252 w. Anal. Calcd for C<sub>24</sub>H<sub>20</sub>PZnBr<sub>2</sub>[Au(CN)<sub>2</sub>]: C, 38.38 %; H, 2.48 %; N, 3.44 %. Found: C, 38.39 %; H, 2.63 %; N, 3.43 %.

### **Ph<sub>4</sub>AsZnCl[Au(CN)<sub>2</sub>]<sub>2</sub>**

Post-exposure (conc. NH<sub>3</sub> vapors – ref. General procedures). FT-IR (ATR, cm<sup>-1</sup>): 3516 vw, 3367 vw, 3287 vw, 3052 vw, 2197 ( $\nu_{CN}$ , vw), 2156 ( $\nu_{CN}$ , m), 2136 ( $\nu_{CN}$ , w), 1605 w, 1484 m, 1439 m, 1409 w, 1338 w, 1313 w, 1261 w, 1202 m, 1160 w, 1085 m, 1023 w, 998 w, 922 w, 841 w, 740 vs. Raman (514 nm, %lp: 1, cm<sup>-1</sup>):

3153 vw, 3058 s, 2155 ( $\nu_{CN}$ , m) 1581 m, 1163 w, 1085 w, 1021 m, 1001 m, 673 w, 613 w, 300 w, 233 w, 183 w.

#### **Ph<sub>4</sub>AsZnBr<sub>2</sub>[Au(CN)<sub>2</sub>]**

Post-exposure (conc. NH<sub>3</sub> vapors – ref. General procedures). FT-IR (ATR, cm<sup>-1</sup>): 3662 vw, 3513 vw, 3417 vw, 3365 vw, 2199 ( $\nu_{CN}$ , vw), 2155 ( $\nu_{CN}$ , m), 2136 ( $\nu_{CN}$ , w), 1606 w, 1484 w, 1439 m, 1394 w, 1338 w, 1319 w, 1241 w, 1213 w, 1186 w, 1162 w, 1085 s, 1060 wbr, 1020 wbr, 923 w, 879 w, 740 vs. Raman (514 nm, %lp: 5, cm<sup>-1</sup>): 3058 vs, 2154 ( $\nu_{CN}$ , w), 1581 m, 1163 w, 1085 w, 1021 w, 1001 s, 671 w, 233 w, 184 w. Anal. Calcd for C<sub>24</sub>H<sub>20</sub>AsZnBr<sub>2</sub>[Au(CN)<sub>2</sub>]NH<sub>3</sub>: C, 35.71 %; H, 2.65 %; N, 4.80 %. Found: C, 35.73 %; H, 2.88 %; N, 5.01 %.

#### **Ph<sub>4</sub>AsZnI<sub>2</sub>[Au(CN)<sub>2</sub>]**

Post-exposure (conc. NH<sub>3</sub> vapors – ref. General procedures). FT-IR (ATR, cm<sup>-1</sup>): 3663 w, 3296 mbr, 3228 wbr, 3184 wbr, 3147 wbr, 2197 ( $\nu_{CN}$ , w), 2140 ( $\nu_{CN}$ , w), 1599 wbr, 1483 m, 1439 s, 1394 wbr, 1338 w, 1238 s, 1186 w, 1162 w, 1084 s, 1063 m, 1023 w, 998 m, 740 vs. Raman (514 nm, %lp: 10, cm<sup>-1</sup>): 3058 s, 2155 s, 1580 w, 1162 vw, 1084 vw, 1021 w, 1001 s, 671 w, 612 vw, 232 w, 184 vw, 112 vs.

#### **Ph<sub>4</sub>AsCdCl[Au(CN)<sub>2</sub>]<sub>2</sub>**

Post-exposure (conc. NH<sub>3</sub> vapors – ref. General procedures). FT-IR (ATR, cm<sup>-1</sup>): 3664 wbr, 3374 wbr, 3350 wbr, 3270 w, 2159 ( $\nu_{CN}$ , s), 2140 ( $\nu_{CN}$ , m), 1601 wbr, 1484 m, 1439 s, 1394 w, 1338 w, 1313 w, 1260 w, 1179 s, 1085 s, 1060 mbr, 1023 w, 998 m, 740 vs. Raman (785 nm, %lp: 50, cm<sup>-1</sup>): 1085 w, 1024 w, 1002 w, 672 w, 613 w, 234 w, 184 w. Note: Raman acquisition severely affected by strong luminescence of sample. Anal. Calcd for C<sub>24</sub>H<sub>20</sub>AsCdCl[Au(CN)<sub>2</sub>]<sub>2</sub>NH<sub>3</sub>: C, 32.14 %; H, 2.22 %; N, 6.69 %. Found: C, 32.43 %; H, 2.17 %; N, 6.55 %.

#### **Ph<sub>4</sub>AsCdBr[Au(CN)<sub>2</sub>]<sub>2</sub>**

Post-exposure (conc.  $\text{NH}_3$  vapors – ref. General procedures). FT-IR (ATR,  $\text{cm}^{-1}$ ): 3249 w, 2177 ( $\nu_{\text{CN}}$ , w), 2156 ( $\nu_{\text{CN}}$ , w), 2140 ( $\nu_{\text{CN}}$ , w), 1578 wbr, 1483 w, 1439 s, 1394 w, 1338 w, 1311 w, 1204 m, 1184 w, 1163 m, 1081 s, 1049 mbr, 1023 w, 997 s, 891 wbr, 745 vs. Raman (785 nm, %lp: 10,  $\text{cm}^{-1}$ ): 2154 w, 1085 vw, 1023 w, 1001 m, 672 w, 613 vw, 232 w, 183 vw. Note: Raman acquisition severely affected by strong luminescence of sample.

#### **$\text{Ph}_4\text{PZnBr}_2[\text{Au}(\text{CN})_2]$**

Post-exposure (conc.  $\text{NH}_3$  vapors – ref. General procedures). FT-IR (ATR,  $\text{cm}^{-1}$ ): 3324 mbr, 3246 wbr, 2140 ( $\nu_{\text{CN}}$ , m), 1588 wbr, 1485 m, 1442 m, 1435 m, 1384 w, 1339 w, 1311 w, 1243 s, 1188 w, 1163 w, 1111 vs, 1070 w, 1028 w, 997 w, 930 w, 843 w, 752 s, 722 vs. Raman (514 nm, %lp: 5,  $\text{cm}^{-1}$ ): 3061 s, 2214 ( $\nu_{\text{CN}}$ , w), 2155 ( $\nu_{\text{CN}}$ , s), 1589 s, 1437 w, 1186 w, 1164 w, 1108 w, 1100 w, 1026 m, 1000 s, 728 w, 681 w, 614 w, 293 w, 255 w, 199 w. Anal. Calcd for  $\text{C}_{24}\text{H}_{20}\text{PZnBr}_2[\text{Au}(\text{CN})_2]\text{NH}_3$ : C, 37.60 %; H, 2.79 %; N, 5.06 %. Found: C, 37.79 %; H, 2.92 %, N, 4.99 %.

#### **$\text{Ph}_4\text{PCdCl}[\text{Au}(\text{CN})_2]_2$**

Post-exposure (conc.  $\text{NH}_3$  vapors – ref. General procedures). FT-IR (ATR,  $\text{cm}^{-1}$ ): 3345 wbr, 3253 w, 2156 ( $\nu_{\text{CN}}$ , s), 2140 ( $\nu_{\text{CN}}$ , m), 1588 wbr, 1485 w, 1443 m, 1435 m, 1202 s, 1163 s, 1111 s, 1028 w, 997 m, 752 m, 723 vs. Raman (785 nm, %lp: 50,  $\text{cm}^{-1}$ ): 1027 w, 1000 w, 681 vw, 615 vw, 249 w, 199 vw. Note: Raman acquisition severely affected by strong luminescence of sample.

## Chapter 4

### Global Conclusions and Future Directions

This thesis focuses on two material properties of the refractive index and luminescence-based sensing of ammonia. The design criteria used to make high index materials such as intrinsic-HRIPs and nanocomposite-HRIPs were applied to coordination polymers and it was found that this synthetic approach can result in high-index materials competitive with the aforementioned routes. However, from a device fabrication standpoint, the refractive index is just one consideration. The high index materials produced in this thesis presumably cannot be used as is for any optical applications and would need to be rendered into a matrix that makes it more processable. This reintroduces the problem of diluting the refractive index of a multi-component system with low index materials. Investigations into producing refractive CPs that have processability characteristics amenable to direct use in optical applications should be undertaken.

The ammonia sensing capabilities of the materials described in chapter 3 are limited in the sense that they are only sensitive to concentrations far exceeding work place hazard or biological relevance. Their potential use in dosimeter applications is also complicated by the observation that the native material-ammoniated adducts are reversible. Nonetheless, they exhibit high quantum yields and some of the native, unexposed materials can perhaps be used in nonlinear optics. The 1-D anionic chains, with one equivalent of  $[\text{Au}(\text{CN})^-]$  per metal, crystallize into the non-centrosymmetric  $P2_12_12_1$  space group and a preliminary screening has shown that they can act as a second harmonic generator. Continued work into this can involve probing the efficiency of the process and assessing whether the effect is uniform throughout the crystal. Additionally, some of the materials may be responsive towards sulfides and thiols warranting further investigation in this regard.

## References

- (1) Bailar Jr., J. C. *Prep. Inorg. React.* **1964**, *1*, 1–25.
- (2) SciFinder search for "Coordination Polymer"
- (3) Janiak, C. *Dalt. Trans.* **2003**, 2781–2804.
- (4) Moulton, B.; Zaworotko, M. J. *Chem. Rev.* **2001**, *101* (6), 1629–1658.
- (5) Janiak, C. *Dalt. Trans.* **2003**, *14*, 2781–2804.
- (6) Ovens, J. S.; Leznoff, D. B. *Chempluschem* **2016**, *81* (8), 842–849.
- (7) Cook, T. R.; Zheng, Y.-R.; Stang, P. J. *Chem. Rev.* **2013**, *113* (1), 734–777.
- (8) Shorrock, C. J.; Jong, H.; Batchelor, R. J.; Leznoff, D. B. *Inorg. Chem.* **2003**, *42* (12), 3917–3924.
- (9) Bartual-Murgui, C.; Ortega-Villar, N. A.; Shepherd, H. J.; Muñoz, M. C.; Salmon, L.; Molnár, G.; Bousseksou, A.; Real, J. A. *J. Mater. Chem.* **2011**, *21* (20), 7217–7222.
- (10) Hill, J. A.; Thompson, A. L.; Goodwin, A. L. *J. Am. Chem. Soc.* **2016**, *138* (18), 5886–5896.
- (11) Pal, A.; Chand, S.; Senthilkumar, S.; Neogi, S.; Das, M. C. *CrystEngComm* **2016**, *18* (23), 4323–4335.
- (12) Thompson, J. R.; Roberts, R. J.; Williams, V. E.; Leznoff, D. B. *CrystEngComm* **2013**, *15* (45), 9387.
- (13) Lama, P.; Sañudo, E. C.; Bharadwaj, P. K. *Dalt. Trans.* **2012**, *41* (10), 2979–2985.
- (14) Mueller, U.; Schubert, M.; Teich, F.; Puetter, H.; Schierle-Arndt, K.; Pastre, J. J. *Mater. Chem.* **2006**, *16* (7), 626–636.
- (15) Corma, A.; Garcia, H.; Llabres i Xamena, F. X. *Chem. Rev.* **2010**, *110* (8), 4606–4655.

- (16) Bu, F.-X.; Hu, M.; Xu, L.; Meng, Q.; Mao, G.-Y.; Jiang, P.-M.; Jiang, J. S. *Chem. Commun.* **2014**, 50, 8543–8546.
- (17) Guoqi, Z.; Haisu, Z.; Sihan, L.; Jahuon, J.; Zixuan, M.; Michelle L, N.; Shengping, Z. *Dalt. Trans.* **2020**, 49 (8), 2610–2615.
- (18) Givaja, G.; Amo-Ochoa, P.; Gomez-Garcia, C. J.; Zamara, F. *Chem Soc Rev* **2012**, 41 (1), 115–147.
- (19) Ramaswamy, P.; Wong, N. E.; Shimizu, G. K. H. *Chem Soc Rev* **2014**, 43 (16), 5913–5932.
- (20) Que, Z.; Ye, Y.; Yang, Y.; Xiang, F.; Chen, S.; Huang, J.; Li, Y.; Liu, C.; Xiang, S.; Zhang, Z. *Inorg. Chem.* **2020**, 59 (6), 3518–3522.
- (21) Batten, S. R.; Murray, K. S. *Coord. Chem. Rev.* **2003**, 246 (1–2), 103–130.
- (22) Geisheimer, A. R.; W., H.; Pacradouni, V.; Sabok-Sayr, S. A.; Sonier, J. E.; Leznoff, D. B. *Dalt. Trans.* **2011**, 40 (29), 7505–7516.
- (23) Gao, W.; Huang, H.; Liu, F.; Zhang, X.; Liu, J. *ChemistrySelect* **2020**, 5 (7), 2185–2189.
- (24) Kitagawa, S.; Kitaura, R.; Noru, S. *Angew. Chemie Int. Ed.* **2004**, 43 (18), 2334–2375.
- (25) Horcajada, P.; Gref, R.; Baati, T.; Allan, P. K.; Maurin, G.; Couvreur, P.; Feney, G.; Morris, R. E.; Sevre, C. *Chem. Rev.* **2012**, 112 (2), 1232–1268.
- (26) Li, L.-P.; Zhou, H.; Chen, J.; Wang, J.-J.; Du, M.; Zhou, W. *ACS Appl. Mater. Interfaces* **2020**, 12 (13), 15246–15254.
- (27) Min, K. S.; Suh, M. P. *J. Am. Chem. Soc.* **2000**, 122, 6834–6840.
- (28) Wang, G.-Y.; Yang, L.-L.; Li, Y.; Song, H.; Ruan, W.-J.; Chang, Z.; Bu, X.-H. *Dalt. Trans.* **2013**, 42, 12865.
- (29) Weiser, H. B.; Milligan, W. O.; Bates, J. B. *J. Phys. Chem.* **1942**, 46 (1), 99–111.



- (30) Herren, F.; Fischer, P.; Ludi, A.; Haelg, W. *Inorg. Chem.* **1980**, *19* (4), 956–959.
- (31) Hecht, E. *Optics*, 4th ed.; Addison Wesley: San Francisco, CA, 2002.
- (32) Rout, C. S.; Hegde, M.; Govindaraj, A.; Rao, C. N. R. *Nanotechnology* **2007**, *18* (20).
- (33) Zakrzewska, K. *Thin Solid Films* **2001**, *391*, 229–238.
- (34) Moos, R. *J. Appl. Ceram. Technol.* **2005**, *2* (5), 401–413.
- (35) Zhou, J.-M.; Shi, W.; Xu, N.; Cheng, P. *Inorg. Chem.* **2013**, *52* (14), 8082–8090.
- (36) Xie, Z.; Ma, L.; de Krafft, K. E.; Jin, A.; Lin, W. *J. Am. Chem. Soc.* **2010**, *132* (3), 922–923.
- (37) Rendell, D. *Fluorescence and Phosphorescence*, 1st ed.; Mowthorpe, D., Ed.; Wiley, 1987.
- (38) Cui, Y.; Yue, Y.; Qian, G.; Chen, B. *Chem. Rev.* **2012**, *112*, 1126–1162.
- (39) Zhang, Y.; Yuan, S.; Day, G.; Wang, X.; Yang, X.; Zhou, H.-C. *Coord. Chem. Rev.* **2018**, *354*, 28–45.
- (40) Douvali, A.; Tsipis, A. C.; Eliseeva, S. V.; Petoud, S.; Papaefstathiou, G. S.; Malliakas, C. D.; Papadas, I.; Armatas, G. S.; Margiolaki, I.; Kanatzidis, M. G.; Lazarides, T.; Manos, M. J. *Angew. Chemie Int. Ed.* **2015**, *54* (5), 1651–1656.
- (41) Wang, J.; Jiang, M.; Yan, L.; Peng, R.; Huangfu, M.; Guo, X.; Li, Y.; Wu, P. *Inorg. Chem.* **2016**, *55* (24), 12660–12668.
- (42) Kubo, Y.; Yamamoto, M.; Ikeda, M.; Takeuchi, M.; Shinkai, S.; Yamaguchi, S.; Tamao, K. *Angew. Chemie Int. Ed.* **2003**, *42* (18), 2036–2040.
- (43) Wu, J.; Liu, W.; Ge, J.; Zhang, H.; Wang, P. *Chem. Soc. Rev.* **2011**, *40* (7), 3483–3495.
- (44) Kenny, T. Wilson, J. S. B. T.-S. T. H., Ed.; Newnes: Burlington, 2005; pp 181–191.

- (45) Lim, S. H.; Feng, L.; Kemling, J. W.; Musto, C. J.; Suslick, K. S. *Nat. Chem.* **2009**, *1* (7), 562–567.
- (46) Kitagawa, S.; Kitaura, R.; Noro, S. I. *Angew. Chemie - Int. Ed.* **2004**, *43* (18), 2334–2375.
- (47) Xie, Z.; Ma, L.; de Krafft, K. E.; Jin, A.; Lin, W. *J. Am. Chem. Soc.* **2010**, *132*, 922–923.
- (48) Gong, X.; Ostrowski, J. C.; Bazan, G. C.; Moses, D.; Heeger, A. J.; Liu, M. S.; Jen, A. K. Y. *Adv. Mater.* **2003**, *15*, 258.
- (49) Thompson, M. E. *MRS Bull* **2007**, *32*, 694–701.
- (50) Wang, G.-Y.; Yang, L.-L.; Li, Y.; Song, H.; Ruan, W.-J.; Chang, Z.; Bu, X.-H. *Dalt. Trans.* **2013**, *42*, 12865.
- (51) Jureschi, C. M.; Linares, J.; Rotaru, A.; Ritti, M. H.; Parlier, M.; Dirtu, M. .; Wolff, M.; Garcia, Y. *Sensors* **2015**, *15* (2), 2388–2398.
- (52) Ovens, J. S.; Leznoff, D. B. *Chem. Mater.* **2015**, *27* (5), 1465–1478.
- (53) Kim, I.; Rothschild, A.; Lee, B. H.; Kim, D. Y.; Ju, S. M.; Tueller, H. L. *Nano Lett.* **2006**, *6* (9), 2009–2013.
- (54) Campbell, M. G.; Liu, S. F.; Swager, T. M.; Dinca, M. *J. Am. Chem. Soc.* **2015**, *137* (43), 13780–13783.
- (55) Manikandan, V.; Petrila, I.; Vigneselvan, S.; Mane, R. S.; Vasile, B.; Dharmavarapu, R.; Lundgaard, S.; Juodkazis, S.; Chandrasekaran, J. *RSC Adv.* **2020**, *10* (7), 3796–3804.
- (56) Wang, S.; Liu, J.; Zhao, H.; Guo, Z.; Xing, H.; Gao, Y. *Inorg. Chem.* **2018**, *57*, 541–544.
- (57) Schmidbaur, H.; Schier, A. *Chem. Soc. Rev.* **2008**, *37* (1931–1951).
- (58) Schmidbaur, H.; Schier, A. *Chem. Soc. Rev.* **2012**, *41*, 370–412.

- (59) Leznoff, D. B.; Xue, B. Y.; Batchelor, R. J.; Einstein, F. W. B.; Patrick, B. O. *Inorg. Chem.* **2001**, *40*, 6026–6034.
- (60) Rundle, R. E. *J. Am. Chem. Soc.* **1954**, *76* (11).
- (61) Arai, G. J. *Recl. Trav. Chim. Pays-Bas* **1962**, *81* (4), 307–312.
- (62) Schmidbaur, H. *Gold Bull.* **1990**, *23* (1), 11–12.
- (63) Mehrotra, P. K.; Hoffmann, R. *Inorg. Chem.* **1978**, *17* (8), 2187–2189.
- (64) Dedieu, A.; Hoffmann, R. *J. Am. Chem. Soc.* **1978**, *100* (7), 2074–2079.
- (65) Koelmel, C.; Ahlrichs, R. *J. Phys. Chem.* **1990**, *94* (14), 5536–5542.
- (66) Pyykkö, P.; Zhao, Y. *Angew. Chemie Int. Ed. English* **1991**, *30* (5), 604–605.
- (67) Pyykko, P.; Mendizabal, F. *Chem. Eur. J.* **1997**, *3* (9), 1458–1465.
- (68) Schmidbaur, H. *Gold Bull.* **2000**, *33*, 3–10.
- (69) Katz, M. J.; Ramnial, T.; Yu, H.-Z.; Leznoff, D. B. *J. Am. Chem. Soc.* **2008**, *130*, 10662–10673.
- (70) Roberts, R. J.; Le, D.; Leznoff, D. B. *Chem. Commun.* **2015**, *51* (14299–14302).
- (71) Forward, J. .; Bohmann, D.; Fackler, J. P.; Staples, R. J. *Inorg. Chem.* **1995**, *34* (25), 6330–6336.
- (72) Wenger, O. S. *Chem. Rev.* **2013**, *113* (5), 3686–3733.
- (73) Yang, G.; Gong, Z.; Lin, Z.; Ye, N. *Chem. Mater.* **2016**, *28*, 9122–9131.
- (74) Ovens, J. S.; Christensen, P. R.; Leznoff, D. B. *Chem. – A Eur. J.* **2016**, *22* (24), 8234–8239.
- (75) Roberts, R. J.; Ahern, J. C.; Patterson, H. H.; Leznoff, D. B. *Eur. J. Inorg. Chem.* **2016**, *2016* (13-14), 2082–2087.
- (76) Sheldrick, G. M. *Acta Crystallogr., Sect. A Found. Adv* **2015**, *71*, 3.

- (77) Hubschle, C. B. .; Sheldrick, G. M. .; Dittrich, B. J. *J. Appl. Crystallogr.* **2011**, *44*, 1281.
- (78) Farrugia, L. J. *J. Appl. Crystallogr.* **2012**, *45*, 849.
- (79) Fenn, T. D. .; Ringe, D. .; Petsko, G. A. *J. Appl. Crystallogr.* **2003**, *36*, 944.
- (80) Tilley, R. J. D. In *Colour and the Optical Properties of Materials*; 2011; pp 60–62.
- (81) Molochnikov, B. I.; Karasik, B. Y.; Laikin, M. V. *Opt. Ind.* **1974**, *7*, 36.
- (82) Meeten, G. H. *Meas. Sci. Technol.* **1997**, *8*, 728.
- (83) Model 2010/M Overview <https://www.metricon.com/model-2010-m-overview> (accessed Mar 7, 2020).
- (84) Tilton, L. W.; Res, J. *NBS* **1935**, *14*, 393.
- (85) Tilton, L. W.; Plyler, E. K.; Stephens, R. E.; Res, J. *NBS* **1949**, *43*, 81.
- (86) Werner, A. J. *Appl. Opt.* **1968**, *7* (837).
- (87) Tentoriand, D.; Lerma, J. R. *Opt. Eng.* **1990**, *29*, 160.
- (88) Medenbach, O.; Shannon, R. D. *J. Opt. Soc. Am. B* **1997**, *14*, 3299.
- (89) Medenbach, O.; Dettmar, D.; Shannon, R. D. *J. Opt. A Pure Appl. Opt.* **2001**, *3*, 174.
- (90) Grehn, J.; Wiss, L.-M. *Technol.* **1959**, *1*, 35.
- (91) Moskalev, V. A.; Smirnova, L. A. *Sov. J. Opt. Technol.* **1987**, *54*, 461.
- (92) Jellison, G. E.; Modine, F. A. *Appl. Opt.* **1997**, *36*, 8184.
- (93) Saylor, C. P.; Res, J. *NBS* **1935**, *14*, 277.
- (94) Little, D. J.; Kane, D. M. *Opt. Express* **2011**, *19*, 19182.
- (95) Kinoshita, T. *Adv. Powder Technol.* **2001**, *12*, 589.

- (96) Meichner, C.; Schedl, A. E.; Neuber, C. *AIP Adv.* **2015**, *5*, 087135.
- (97) Batsanov, S. S.; Ruchkin, E. D.; Poroshina, I. A. *Refractive Indices of Solids*; Springer: Singapore, 2016.
- (98) McDermott, R. Kingfisher captured catching fish at bottom of river in new photographs <https://www.independent.co.uk/news/uk/home-news/kingfisher-photos-catch-fish-vince-burton-dereham-norfolk-a8375806.html> (accessed Sep 19, 2020).
- (99) Philo, N. Micrograph of photosensor array [https://en.wikipedia.org/wiki/Image\\_sensor#/media/File:A\\_micrograph\\_of\\_the\\_corner\\_of\\_the\\_photosensor\\_array\\_of\\_a\\_'webcam'.jpeg](https://en.wikipedia.org/wiki/Image_sensor#/media/File:A_micrograph_of_the_corner_of_the_photosensor_array_of_a_'webcam'.jpeg) (accessed Sep 19, 2020).
- (100) Tomar, R. Internal Reflection <https://www.jagranjosh.com/articles/ray-optics-iit-jee-important-questions-and-preparation-tips-1456922445-1> (accessed Sep 19, 2020).
- (101) Tilley, R. J. D. *Colour and the Optical Properties of Materials*, 2nd ed.; Wiley: Chichester, West Sussex, U.K., 2011.
- (102) Tilley, R. J. . In *Colour and the Optical Properties of Materials*; 2011; pp 58–60.
- (103) Yen, H.-J.; Liou, G.-S.; Hayashi, H.; Takata, T.; Gribkova, P. N.; Vinogradova, N. K.; Komarova, L. I.; Erz, B. V.; Khanarian, G.; Simon, E. S. *J. Mater. Chem.* **2010**, *20* (20), 4080.
- (104) Mont, F. W.; Kim, J. K.; Schubert, M. F.; Schubert, E. F.; Siegel, R. W. *J. Appl. Phys.* **2008**, *103* (8), 083120.
- (105) Matsuda, T.; Funae, Y.; Yoshida, M.; Yamamoto, T.; Takaya, T. *J. Appl. Polym. Sci.* **2000**, *76* (1), 50–54.
- (106) Wang, Y.; Flaim, T.; Mercado, R.; Fowler, S.; Holmes, D.; Planje, C. *Proc. SPIE* **2005**, *5724* (April 2005), 42.
- (107) Krogman, K. C.; Druffel, T.; Sunkara, M. K. *Nanotechnology* **2005**, *16* (7).

- (108) Ma, H.; Jen, A. K. Y.; Dalton, L. R. *Adv. Mater.* **2002**, *14* (19), 1339–1365.
- (109) Nakamura, T.; Fujii, H.; Juni, N.; Tsutsumi, N. *Opt. Rev.* **2006**, *13* (2), 104–110.
- (110) Liu, J.; Ueda, M. *J. Mater. Chem.* **2009**, *19* (47), 8907.
- (111) Macdonald, E. K.; Shaver, M. P. *Polym. Int.* **2015**, *64* (1), 6–14.
- (112) Flaim, T. D.; Wang, Y.; Mercado, R.; Flaim, T. D.; Wang, Y.; Mercado, R. *Proc. SPIE* **2004**, *5250* (February 2004), 423.
- (113) Gaudiana, R. A.; Minns, R. A.; Rogers, H. G. High refractive index polymers. 5132430A, 1992.
- (114) Liu, J.-G.; Nakamura, Y.; Shibasaki, Y.; Ando, S.; Ueda, M. *J Polym Sci A Polym Chem* **2007**, *45*, 5606–5617.
- (115) Liu, J. G.; Nakamura, Y.; Shibasaki, Y.; Ando, S.; Ueda, M. *Macromolecules* **2007**, *40* (13), 4614–4620.
- (116) Liu, J.-G.; Nakamura, Y.; Suzuki, Y.; Shibasaki, Y.; Ando, S.; Ueda, M. *Macromolecules* **2007**, *40*, 7902–7909.
- (117) Liu, J.-G.; Nakamura, Y.; Shibasaki, Y.; Ando, S.; Ueda, M. *Macromolecules* **2007**, *40*, 4614–4620.
- (118) You, N. Y. S.; Yorifuji, D. S. A.; Ueda, M. *Macromolecules* **2008**, *41*, 6361–6366.
- (119) You, N.-H.; Suzuki, Y.; Higashihara, T.; Ando, S.; Ueda, M. *Polymer (Guildf)*. **2009**, 789–795.
- (120) Terraza, C. A.; Liu, J.-G.; Nakamura, Y.; Shibasaki, Y.; Ando, S.; Ueda, M. *J Polym Sci A Polym Chem* **2008**, *46*, 1510–1520.
- (121) Shobha, H. K.; Sekharipuram, V.; McGrath, J. E.; Bhatnagar, A. High refractive index thermoplastic polyphosphonates. 6288210 B1, 2001.
- (122) Olshavsky, M.; Allcock, H. R. *Macromolecules* **1995**, *28*, 6188–6197.

- (123) Olshavsky, M.; Allcock, H. R. *Macromolecules* **1997**, *30*, 4179–4183.
- (124) Stiegman, A. High refractive index polymers. 0054136, 2011.
- (125) Bhagat, S. D.; Chatterjee, J.; Chen, B.; Stiegman, A. E. *Macromolecules* **2012**, *45*, 1174–1181.
- (126) Mosley, D. W.; Khanarian, G.; Conner, D. M.; Thorsen, D. L.; Zhang, T.; Wills, M. *J. Appl. Polym. Sci.* **2014**, *131*, 39824–39834.
- (127) Pacquet, C.; Cyr, P. W.; Kumacheva, E.; Manners, I. *Chem. Commun.* **2004**, *2*, 234–235.
- (128) Weibel, M.; Caseri, W.; Suter, U. W.; Kiess, H.; Wehrli, E. *Polym. Adv. Technol.* **1991**, *2*, 75.
- (129) Althues, H.; Henle, J.; Kaskel, S. *Chem. Soc. Rev.* **2007**, *9*, 1454.
- (130) Yuwono, A. H.; Liu, B. H.; Xue, J. M.; Wang, J.; Elim, H. I.; Ji, W.; Li, Y.; White, T. *J. J. Mater. Chem.* **2004**, *14*, 2978.
- (131) Suzuki, N.; Tomita, Y.; Ohmori, K.; Hidaka, M.; Chikama, K. *Opt. Express* **2006**, *14*, 12712.
- (132) Papadimitrakopoulos, F.; Wisniecki, P.; Bhagwagar, D. E. *Chem. Mater.* **1997**, *9*, 2928.
- (133) Lu, C. L.; Cui, Z. C.; Li, Z.; Guan, C.; Yang, B.; Shen, J. C. *J. Mater. Chem.* **2003**, *13*, 526.
- (134) Edmondson, S.; Osborne, V. L.; Huck, W. T. S. *Chem. Soc. Rev.* **2004**, *33*, 14–22.
- (135) Barbey, R.; Lavanant, L.; Paripovic, D.; Schuwer, N.; Sugnaux, C.; Tugulu, S.; Klok, H.-A. *Chem. Rev.* **2009**, *109*, 5437–5527.
- (136) Tao, P.; Yu, L.; Rungta, A.; Viswanath, A.; Gao, J.; Benicewicz, B. C.; Siegel, R. W.; Schadler, L. S. *J. Mater. Chem.* **2011**, *21*, 18623.

- (137) Liu, J. G.; Nakamura, Y.; Ogura, T.; Shibasaki, Y.; Ando, S.; Ueda, M. *Chem. Mater.* **2008**, No. 20, 273.
- (138) Chang, C. C.; Wei, K. H.; Chang, Y. L.; Chen, W. C. *J. Polym. Res.* **2003**, 10, 1.
- (139) Su, H. W.; Chen, W. C. *J. Mater. Chem.* **2008**, 18, 1139–1945.
- (140) Chau, J. L. H.; Tung, C.-T.; Lin, Y.-M.; Li, A.-K. *Mater. Lett.* **2008**, 62, 3416–3418.
- (141) Nicol, E.; Nicolai, T. *Macromolecules* **2001**, 34, 56–65.
- (142) Kuzmin, A.; Purans, J. *Radiat. Meas.* **2001**, 33 (5), 583–586.
- (143) Nazarov, M. V.; Jeon, D. Y.; Kang, J. H.; Popovici, E.-J.; Muresan, L.-E.; Zamoryanskaya, M. V.; Tsukerblat, B. S. *Solid State Commun.* **2004**, 131 (5), 307–311.
- (144) Grobelna, B.; Lipowska, B.; Klonkowski, A. M. *J. Alloys Compd.* **2006**, 419 (1), 191–196.
- (145) M Zawawi, S. M.; Yahya, R.; Hassan, A.; Mahmud, H. N. M. E.; Daud, M. N. *Chem. Cent. J.* **2013**, 7 (1), 80.
- (146) Bylichkina, T. I.; Soleva, L. I.; Pobedinskaya, E. A.; Porai Koshits, M. A.; Belov, N. V. *Kristallografiya* **1970**, 15, 165–167.
- (147) Katsoulis, D. E. *Chem. Rev.* **1998**, 98, 359–387.
- (148) Roberts, G. L.; Fessler, R. G. No Title. 3346604, 1967.
- (149) Lomakina, S. V.; Shatova, T. S.; Kazansky, L. P. *Corros. Sci* **1994**, 36, 1645.
- (150) Pikel'nyi, A. Y.; Reznikova, G. G.; Brynza, A. P.; Khmelovskaya, S. A.; Pikel'naya, O. A. *Russ. J. Electrochem.* **1995**, 31, 484.
- (151) Ohkita, H.; Mukoh, M.; Tagaya, A.; Koike, Y. *Mat. Res. Soc. Symp. Proc.* **2003**, 771, L7.5.1.
- (152) Shabtay, G.; Eiding, E.; Zalevsky, Z.; Mendlovic, D.; Marom, E. *Opt. Express*



**2002**, 10, 1534.

- (153) Kashkarov, P. K.; Golovan, L. A.; Fedotov, A. B.; Efimova, A. I.; Kuznetsova, L. P.; Timoshenko, V. Y.; Sidorov-Biryukov, D. A.; Zheltikov, A. M.; Haus, J. W. *J. Opt. Soc. Am. B* **2002**, 19, 2273.
- (154) Fiore, A.; Berger, V.; Rosencher, E.; Bravetti, P.; Nagle, J. **1998**, 391 (6666), 463–466.
- (155) Zhang, M.; Huo, G. *Opt. Eng.* **2014**, 53 (8), 086105.
- (156) Newnham, R. E. *Properties of Materials: Anisotropy, Symmetry, Structure*; Oxford University Press: New York, 2005.
- (157) Guan, D.; Thompson, J. R.; Leznoff, D. B. *Can. J. Chem.* **2018**, 96 (2), 226–234.
- (158) Bulgan, A. T. *Energy Convers. Manag.* **1997**, 38 (14), 1431–1438.
- (159) Colonna, P.; Gabrielli, S. *Appl. Therm. Eng.* **2003**, 23, 381–396.
- (160) Olthuis, W.; Berg, A. Van Den; Timmer, B. *Sens. Actuators B Chem.* **2005**, 107, 666–677.
- (161) Velders, G. J. M.; Andersen, S. O.; Daniel, J. S.; Fahey, D. W.; McFarland, M. *Proc. Natl. Acad. Sci. U. S. A.* **2007**, 104 (12).
- (162) Ravishankara, A. R.; Daniel, J. S.; Portmann, R. W. *Science*. **2009**, 123 (October), 2007–2010.
- (163) Cardin, M. Ammonia As a Refrigerant: Pros and Cons  
<https://www.goodway.com/hvac-blog/2009/08/ammonia-as-a-refrigerant-pros-and-cons/> (accessed Feb 14, 2020).
- (164) Hoz, R. E.; Schlueter, D. P.; Rom, W. N. *Am. J. Ind. Med.* **1996**, 29 (2).
- (165) Hoz, R. E. De; Schlueter, D. P. *Am. J. Ind. Med.* **1996**, 14 (1 996).
- (166) Properties of Ammonia  
[https://www.osha.gov/SLTC/etools/ammonia\\_refrigeration/ammonia/index.html](https://www.osha.gov/SLTC/etools/ammonia_refrigeration/ammonia/index.html)

(accessed Feb 15, 2020).

- (167) *National Research Council (US) Committee on Acute Exposure Guideline Levels. Acute Exposure Guideline Levels for Selected Airborne Chemicals: Volume 6.*; National Academic Press (US): Washington, DC, 2008.
- (168) Medical Management Ammonia  
<https://www.atsdr.cdc.gov/mmg/mmg.asp?id=7&tid=2> (accessed May 4, 2020).
- (169) Srivastava, R. K.; Lal, P.; Dwivedi, R.; Srivastava, S. K. *Sens. Actuators B.* **1994**, *21*, 213–218.
- (170) Palmqvist, E.; Kriz, C. B.; Svanberg, K.; Khayyami, M.; Kriz, D. *Biosens. Bioelectron.* **1995**, *10*, 283–287.
- (171) Lahdesmaki, I.; Kubiak, W. W.; Lewenstam, A.; Ivaska, A. *Talanta* **2000**, *52*, 269–275.
- (172) Moseley, P. T. *Meas. Sci. Technol.* **1997**, *8*, 223.
- (173) Spetz, A.; Armgarth, M.; Lundstrom, I. *J. Appl. Phys* **1988**, *1274* (64).
- (174) Chang, S. C.; Stetter, J. R.; Cha, C. S. *Talanta* **40** (4), 461–477.
- (175) Lahdesmaki, I.; Lewenstam, A.; Ivaska, A. *Talanta*. **1996**, *43*, 125–134.
- (176) Moseley, P. T.; Williams, D. E. *Sensors and Actuators* **1990**, *B1*, 113–115.
- (177) Some, S.; Xu, Y.; Kim, Y.; Yoon, Y.; Qin, H.; Kulkarni, A.; Kim, T.; Lee, H. *Sci Rep* **2013**, *3*, 1868.
- (178) Varju, B. R.; Ovens, J. S.; Leznoff, D. B. *Chem. Commun.* **2017**, *53*, 6500–6503.
- (179) Varju, B. R.; Wollschlaeger, S. A.; Leznoff, D. B. *Chem. Eur. J.* **2019**, 9017–9025.
- (180) Wang, H.; Cheng, F.; Zou, C.; Li, Q.; Hua, Y.; Duan, J.; Jin, W. *CrystEngComm* **2016**, 1–8.
- (181) Lefebvre, J.; Korcok, J. L.; Katz, M. J.; Leznoff, D. B. *Sensors* **2012**, 3669–3692.

- (182) Varju, B. R.; Ovens, J. S.; Leznoff, D. B. *Chem. Commun.* **2017**, 53 (48), 6500–6503.
- (183) Katz, M. J.; Ramnial, T.; Yu, H.-Z.; Leznoff, D. B. *J. Am. Chem. Soc.* **2008**, 130 (32), 10662–10673.
- (184) Lefebvre, J.; Batchelor, R. J.; Leznoff, D. B. *J. Am. Chem. Soc.* **2004**, 126 (16117–16125).
- (185) Yanna, L.; Zhang, X.; Chen, W.; Shi, W.; Chang, P. *Inorg. Chem.* **2017**, 56 (19), 11768–11778.
- (186) Gong, W.-J.; Ren, Z.-G.; Li, H.-X.; Zhang, J.-G.; Lang, J.-P. *Cryst. Growth Des.* **2017**, 17 (2), 870–881.
- (187) Thompson, J. R. *Designing Birefringent Materials: A Crystal Engineering Approach*, Simon Fraser University, 2017.
- (188) Zaim, A.; Nozary, H.; Guenee, L.; Besnard, C.; Lemonier, J.-F.; Petoud, S.; Piguet, C. *Chem. Eur. J.* **2012**, 18, 7155–7168.
- (189) Piguet, C.; Bunzli, P. J.-C.; Bernardinelli, G.; Bochet, C. G. *J. Chem. Soc., Dalton Trans.* **1995**, 83–97, 1995.
- (190) Nozary, H.; Piguet, C.; Tissot, P.; Bu, J.-C. G.; Deschenaux, R.; Guillon, D. *J. Am. Chem. Soc.* **1998**, 120, 12274–12288.

# Appendix A.

## Crystallographic Data

Table A1. Crystallographic Data (Refractive Materials)

Empirical formula	Cu <sub>3</sub> H <sub>10</sub> Na <sub>3</sub> O <sub>5</sub> S <sub>2</sub>	C <sub>10</sub> H <sub>10</sub> O <sub>4</sub> PbS <sub>2</sub>	CdH <sub>2</sub> KN <sub>2</sub> OS <sub>3</sub>	C <sub>6</sub> H <sub>2</sub> N <sub>2</sub> Pb <sub>3</sub> S <sub>3</sub>	C <sub>20</sub> (H <sub>10</sub> )N <sub>6</sub> Si <sub>1.05</sub> Zn <sub>0.18</sub>	C <sub>2</sub> K <sub>2</sub> N <sub>2</sub> S <sub>1</sub>	C <sub>2.07</sub> H <sub>1.33</sub> N <sub>2.08</sub> S <sub>2</sub> Zn <sub>0.07</sub>
Formula weight	364.25	547.51	282.44	432.51	93.82	226.42	241.37
Temperature/K	297(2)	149.99	296(2)	150(2)	150(2)	150(2)	149(2)
Crystal system	monoclinic	monoclinic	orthorhombic	orthorhombic	orthorhombic	orthorhombic	orthorhombic
Space group	P2 <sub>1</sub> /c	P2 <sub>1</sub> /n	Pna2 <sub>1</sub>	Aea2	P2 <sub>1</sub> 2 <sub>1</sub> 2 <sub>1</sub>	Pbcm	Pbcn
a/Å	11.6426(7)	7.9182(9)	16.5241(14)	12.1146(3)	13.7655(12)	6.4670(7)	12.8363(2)
b/Å	5.5489(3)	8.6069(10)	4.1186(3)	10.2685(3)	14.9280(12)	6.5396(7)	11.4520(2)
c/Å	10.7166(7)	21.367(3)	33.900(2)	16.9449(5)	19.0854(14)	17.2302(18)	7.56190(10)
a°	90	90	90	90	90	90	90
β°	96.2020(10)	97.074(2)	90	90	90	90	90
γ°	90	90	90	90	90	90	90
Volume/Å <sup>3</sup>	688.28(7)	1445.1(3)	2307.1(3)	2107.92(10)	3921.9(5)	728.69(13)	1111.61(3)
Z	2	4	8	8	44	6	6
ρ <sub>calc</sub> /cm <sup>3</sup>	1.758	2.516	1.626	2.726	1.748	2.064	2.163
μ/mm <sup>-1</sup>	0.487	12.007	0.976	16.559	7.802	2.063	13.372
F(000)	368	1032	1152	1576	2080	448	713
Radiation	MoKα (λ = 0.71073)	MoKα (λ = 0.71073)	MoKα (λ = 0.71073)	MoKα (λ = 0.71073)	CuKα (λ = 1.54178)	MoKα (λ = 0.71073)	CuKα (λ = 1.54178)
2θ range for data collection°	3.518 to 56.624	3.842 to 51.408	2.402 to 56.872	4.808 to 51.43	7.518 to 146.586	4.728 to 56.632	10.352 to 136.64
Index ranges	-11 ≤ h ≤ 15, -7 ≤ k ≤ 7, -14 ≤ l ≤ 13	-7 ≤ h ≤ 7, -7 ≤ k ≤ 7, -7 ≤ l ≤ 7	-22 ≤ h ≤ 22, -5 ≤ k ≤ 5, -45 ≤ l ≤ 45	-14 ≤ h ≤ 14, -12 ≤ k ≤ 12, -20 ≤ l ≤ 18	-16 ≤ h ≤ 17, -18 ≤ k ≤ 18, -19 ≤ l ≤ 23	-8 ≤ h ≤ 7, -8 ≤ k ≤ 8, -22 ≤ l ≤ 22	-11 ≤ h ≤ 15, -8 ≤ k ≤ 13, -9 ≤ l ≤ 9
Reflections collected	5059	2558	24611	9514	18325	5196	4535
Independent reflections	1681 [R <sub>int</sub> = 0.0175, R <sub>sigma</sub> = 0.0187]	2558 [R <sub>int</sub> = ?, R <sub>sigma</sub> = 0.0255]	5837 [R <sub>int</sub> = 0.0416, R <sub>sigma</sub> = 0.0393]	1765 [R <sub>int</sub> = 0.0358, R <sub>sigma</sub> = 0.0356]	7505 [R <sub>int</sub> = 0.1305, R <sub>sigma</sub> = 0.1685]	942 [R <sub>int</sub> = 0.0260, R <sub>sigma</sub> = 0.0186]	1022 [R <sub>int</sub> = 0.0358, R <sub>sigma</sub> = 0.0300]
Data/restraints/parameters	1681/0/108	2558/0/108	5837/7/287	1765/1/123	7505/0/487	942/0/20	1022/0/73
Goodness-of-fit on F <sup>2</sup>	0.777	1.166	1.13	1.068	0.987	1.035	0.948
Final R indexes [I ≥ 2σ(I)]	R <sub>1</sub> = 0.0291, wR <sub>2</sub> = 0.0818	R <sub>1</sub> = 0.0366, wR <sub>2</sub> = 0.0835	R <sub>1</sub> = 0.0474, wR <sub>2</sub> = 0.1151	R <sub>1</sub> = 0.0180, wR <sub>2</sub> = 0.0350	R <sub>1</sub> = 0.0776, wR <sub>2</sub> = 0.1723	R <sub>1</sub> = 0.0423, wR <sub>2</sub> = 0.0982	R <sub>1</sub> = 0.0241, wR <sub>2</sub> = 0.0610
Final R indexes [all data]	R <sub>1</sub> = 0.0349, wR <sub>2</sub> = 0.0879	R <sub>1</sub> = 0.0407, wR <sub>2</sub> = 0.0850	R <sub>1</sub> = 0.0592, wR <sub>2</sub> = 0.1282	R <sub>1</sub> = 0.0236, wR <sub>2</sub> = 0.0369	R <sub>1</sub> = 0.1156, wR <sub>2</sub> = 0.1990	R <sub>1</sub> = 0.0459, wR <sub>2</sub> = 0.1009	R <sub>1</sub> = 0.0262, wR <sub>2</sub> = 0.0622
Largest diff. peak/hole / e Å <sup>-3</sup>	0.33/-0.45	1.49/-1.83	1.17/-0.42	0.63/-0.47	0.85/-1.11	1.60/-1.09	0.58/-0.36
Flack parameter	-	-	0.37(4)	0.026(9)	0.01(5)	-	-

Table A2. Crystallographic Data (Ammonia Sensing)

Empirical formula	C <sub>20</sub> H <sub>10</sub> AsAu <sub>3</sub> ClN <sub>4</sub> Zn	C <sub>20</sub> H <sub>10</sub> AsAuBr <sub>2</sub> N <sub>2</sub> Zn	C <sub>20</sub> H <sub>10</sub> AsAuI <sub>2</sub> N <sub>2</sub> Zn	C <sub>20</sub> H <sub>10</sub> AsAu <sub>2</sub> BrCdN <sub>4</sub>	C <sub>20</sub> H <sub>10</sub> AsAu <sub>2</sub> CdClN <sub>4</sub>	C <sub>20</sub> H <sub>10</sub> AsBr <sub>2</sub> N <sub>2</sub> PZn	C <sub>20</sub> H <sub>10</sub> Au <sub>2</sub> CdClN <sub>4</sub> P
Formula weight	982.15	857.52	951.5	1073.64	1029.18	813.57	985.23
Temperature/K	151(2)	150(2)	150(2)	299.04	150(2)	298(2)	160(2)
Crystal system	tetragonal	orthorhombic	orthorhombic	tetragonal	tetragonal	orthorhombic	tetragonal
Space group	P4/n	P2 <sub>1</sub> 2 <sub>1</sub> 2 <sub>1</sub>	P2 <sub>1</sub> 2 <sub>1</sub> 2 <sub>1</sub>	P4/n	P4/n	P2 <sub>1</sub> 2 <sub>1</sub> 2 <sub>1</sub>	P4/n
a/Å	14.2280(2)	7.2612(4)	7.3346(3)	14.757(5)	14.6222(3)	7.4764(7)	14.4262(11)
b/Å	14.2280(2)	12.7278(6)	12.8675(5)	14.757	14.6222(3)	12.5513(11)	14.4262(11)
c/Å	6.79240(10)	29.3752(16)	29.8933(10)	6.755(2)	6.6324(2)	29.087(3)	6.9800(5)
a°	90	90	90	90	90	90	90
β°	90	90	90	90	90	90	90
γ°	90	90	90	90	90	90	90
Volume/Å <sup>3</sup>	1375.03(4)	2714.8(2)	2821.27(19)	1471.2(10)	1418.07(7)	2729.4(4)	1452.6(2)
Z	2	4	4	2	2	4	2
ρ <sub>calc</sub> /cm <sup>3</sup>	2.372	2.098	2.24	2.424	2.41	1.98	2.252
μ/mm <sup>-1</sup>	23.104	16.027	29.288	13.161	27.369	9.25	10.97
F(000)	908	1608	1752	980	944	1536	908
Radiation	CuKα (λ = 1.54178)	CuKα (λ = 1.54178)	CuKα (λ = 1.54178)	MoKα (λ = 0.71073)	CuKα (λ = 1.54178)	MoKα (λ = 0.71073)	MoKα (λ = 0.71073)
2θ range for data collection°	8.79 to 139.32	6.018 to 139.358	5.912 to 136.812	3.904 to 56.54	8.552 to 139.042	3.534 to 56.562	3.992 to 56.734
Index ranges	-16 ≤ h ≤ 14, -17 ≤ k ≤ 16, -6 ≤ l ≤ 8	-8 ≤ h ≤ 8, -15 ≤ k ≤ 15, -35 ≤ l ≤ 35	-8 ≤ h ≤ 7, -15 ≤ k ≤ 15, -36 ≤ l ≤ 35	-19 ≤ h ≤ 19, -13 ≤ k ≤ 19, -8 ≤ l ≤ 9	-16 ≤ h ≤ 14, -17 ≤ k ≤ 17, -7 ≤ l ≤ 7	-9 ≤ h ≤ 9, -14 ≤ k ≤ 16, -37 ≤ l ≤ 38	-9 ≤ h ≤ 19, -16 ≤ k ≤ 18, -9 ≤ l ≤ 9
Reflections collected	7206	17475	62700	7493	7748	20986	5493
Independent reflections	1291 [R <sub>int</sub> = 0.0432, R <sub>sigma</sub> = 0.0302]	4958 [R <sub>int</sub> = 0.0270, R <sub>sigma</sub> = 0.0417]	5103 [R <sub>int</sub> = 0.0663, R <sub>sigma</sub> = 0.0360]	1825 [R <sub>int</sub> = 0.0199, R <sub>sigma</sub> = 0.0239]	1324 [R <sub>int</sub> = 0.0333, R <sub>sigma</sub> = 0.0245]	6742 [R <sub>int</sub> = 0.0545, R <sub>sigma</sub> = 0.0798]	1821 [R <sub>int</sub> = 0.0218, R <sub>sigma</sub> = 0.0364]
Data/restraints/parameters	1291/0/87	4958/0/298	5103/0/140	1825/0/49	1324/0/87	6742/0/298	1821/0/52
Goodness-of-fit on F <sup>2</sup>	1.13	1.028	2.076	1.146	2.521	0.81	1.116
Final R indexes [I ≥ 2σ(I)]	R <sub>1</sub> = 0.0308, wR <sub>2</sub> = 0.0856	R <sub>1</sub> = 0.0310, wR <sub>2</sub> = 0.0755	R <sub>1</sub> = 0.0765, wR <sub>2</sub> = 0.2443	R <sub>1</sub> = 0.0612, wR <sub>2</sub> = 0.2055	R <sub>1</sub> = 0.0590, wR <sub>2</sub> = 0.2761	R <sub>1</sub> = 0.0466, wR <sub>2</sub> = 0.1165	R <sub>1</sub> = 0.0603, wR <sub>2</sub> = 0.1768
Final R indexes [all data]	R <sub>1</sub> = 0.0312, wR <sub>2</sub> = 0.0861	R <sub>1</sub> = 0.0322, wR <sub>2</sub> = 0.0763	R <sub>1</sub> = 0.0817, wR <sub>2</sub> = 0.2508	R <sub>1</sub> = 0.0687, wR <sub>2</sub> = 0.2127	R <sub>1</sub> = 0.0612, wR <sub>2</sub> = 0.2794	R <sub>1</sub> = 0.0957, wR <sub>2</sub> = 0.1434	R <sub>1</sub> = 0.0764, wR <sub>2</sub> = 0.1865
Largest diff. peak/hole / e Å <sup>-3</sup>	1.70/-2.63	1.62/-1.26	3.74/-3.00	3.94/-1.42	3.46/-2.19	1.12/-0.84	3.67/-1.08
Flack parameter	-	-0.013(4)	0.026(5)	-	1.55/-1.40	-0.021(6)	-



## Appendix B1.

### Selected Bond Lengths and Angles for Family $\text{Ph}_4\text{AsMX}[\text{Au}(\text{CN})_2]_2$ (MX: ZnCl, CdCl, CdBr)

**Table 1A.** Selected bond lengths and angles of  $\text{Ph}_4\text{AsZnCl}[\text{Au}(\text{CN})_2]_2$

Bond	Bond length Å (angle, °)
Zn1-N1	2.120
Zn1-Cl1	2.244
C1-Au1	1.991
As1-C2	1.915
Cl1-Zn1-N1	105.58
Au1-C1-N1	177.67
C2-As1-C3	119.26
N1-Zn1-	85.86 and 148.83

**Table 1B.** Selected bond lengths and angles of  $\text{Ph}_4\text{AsCdCl}[\text{Au}(\text{CN})_2]_2$

Bond	Bond length Å (angle, °)
Cd1-Cl1	2.442
Cd1-N1	2.296
N1-C1	1.145
C1-Au1	1.995
As-C	1.862
Cl1-Cd1-N1	105.84
C-Au-C	180
C-As-C	108.01
N1-Cd-N1	86.73 and 149.54

**Table 1C.** Selected bond lengths and angles of  $\text{Ph}_4\text{AsCdBr}[\text{Au}(\text{CN})_2]_2$

Bond	Bond length Å (angle, °)
Cd1-Br1	2.579
Cd1-N1	2.318
N1-C1	1.126
C1-Au1	1.993
As-C	1.874
Br1-Cd1-N1	105.46
C1-Au1-C1	180
C-As-C	111.56
N1-Cd1-N1	85.92 and 149.07

**Table 1D.** Selected bond lengths and angles of  $\text{Ph}_3\text{PCdBr}[\text{Au}(\text{CN})_2]_2$

Bond	Bond length Å (angle, °)
Cd1-Cl1	2.484
Cd1-N1	2.316
N1-C1	1.113
C1-Au1	1.991
P-C	1.766
Cl1-Cd1-N1	106.85
C-Au-C	180
C-P-C	106.74
N1-Cd1-N1	85.18 and 146.3

## Appendix B2.

### Selected Bond Lengths and Angles for Family $\text{Ph}_4\text{AsMX}_2[\text{Au}(\text{CN})_2]$ (MX: ZnBr, ZnI)

**Table 2A.** Selected bond lengths and angles of  $\text{Ph}_4\text{AsZnBr}_2[\text{Au}(\text{CN})_2]$

Bond	Bond length Å (angle, °)
Zn1-Br1	2.349(2)
Zn1-N1	2.03(1)
C1-N1	1.12 (2)
Au1-C1	1.98(1)
As1-C	1.910
Br1-Zn1-Br2	118.26
N2-Zn1-N1	95.78
Au1-C2-N2	178.33
C2-Au1-C1	177.63
C-As-C	112.1

**Table 2B.** Selected bond lengths and angles of  $\text{Ph}_4\text{AsZnI}_2[\text{Au}(\text{CN})_2]$

Bond	Bond length Å (angle, °)
Zn1-I1	2.5431
Zn1-I2	2.5151
Zn1-N1	2.026
As-C	1.916
I1-Zn1-I2	118.45
I1-Zn1-N1	111.89
C1-Au1-C2	178.41
C-As-C	111.62

**Table 2C.** Selected bond lengths and angles of  $\text{Ph}_4\text{PZnBr}_2[\text{Au}(\text{CN})_2]$

Bond	Bond length Å (angle, °)
Zn1-Br	2.34
Zn1-N1	2.045
Zn1-N2	1.071
N1-C1	1.117
C1-Au1	2.007
P-C	1.810
Br-Zn-Br	118.62
N-Zn-N	96.46
C-Au-C	176.49
C-P-C	112.76



## Appendix B3.

### Selected Bond Lengths and Angles for 1,5-nda based Refractive Materials

**Table 3A.** Selected bond lengths and angles of  $\text{Na}_2(1,5\text{-nda})\text{H}_2\text{O}$

Bond	Bond length Å (angle, °)
S1-O1	1.446
O1-Na1	2.324
Na1-O2	2.369
O1A-Na1-O1B	88.39
C1A-S1-O1B	106.68

**Table 3B.** Selected bond lengths and angles of  $\text{Pb}(1,5\text{-nda})(\text{H}_2\text{O})_3$

Bond	Bond length Å (angle, °)
Pb1-O2	2.789
S1-O2	1.457
O2-S1-O1	110.16
O2-Pb01-O3	94.76
C-S1-O2	105.92

## Appendix B4.

### Selected Bond Lengths and Angles for bismuthiol II based Refractive Materials

**Table 4A.** Selected bond lengths and angles of K(bismuthiol II)H<sub>2</sub>O

Bond	Bond length Å (angle, °)
K1-S4	3.203
K2-O2	2.733
K2-O1	2.778
S1-C	1.712
C1-S2	1.750
N1-N2	1.403
N2-C3	1.436
C1-S1-K2	96.99
C1-S1-K1	83.49
C1-S2-C2	91.64

**Table 4B.** Selected bond lengths and angles of Zn(bismuthiol II)<sub>2</sub>

Bond	Bond length Å (angle, °)
Zn-S	2.331
N-C(phenyl)	1.448
S-Zn-S	102.41
C-S-C	90.24

**Table 4C.** Selected bond lengths and angles of Pb(bismuthiol II)<sub>2</sub>

Bond	Bond length Å (angle, °)
Pb1-S3	2.965
Pb1-S1	2.695
N1-C3	1.448
S3-Pb1-S3	156.21
S1-Pb1-S3	80.91

## Appendix B5.

### Selected Bond Lengths and Angles for bismuthiol I-based Refractive Materials

**Table 5A.** Selected bond lengths and angles of  $K_2(\text{bismuthiol I})$

Bond	Bond length Å (angle, °)
S-K	3.260
K-S-K	103.84

**Table 5B.** Selected bond lengths and angles of  $Zn(\text{bismuthiol I}+H)_2$

Bond	Bond length Å (angle, °)
Zn1-S3	2.356
Zn1-S1	2.331
N2-H1	0.736
S3-Zn1-S3	105.75
S3-Zn1-S1	112.57

## Appendix C.

### High Birefringence Materials

#### Attempted Synthesis and Characterization of Halogenated 2,6-bis(bendimidazol-2-yl)pyridine Coordination Polymers

It was found that coordination polymers incorporating halogenated 2,6-bis(bendimidazol-2-yl)pyridine have very high birefringence values. This is due to the greater polarization anisotropy observed in haloBBP compared to terpy and bbp. These compounds were initially discovered and characterized during the Ph.D. work of Dr. John Robert Thompson. The haloBBP CPs are produced in low yields and separation from unreacted ligand is difficult making bulk purity a problem since their initial synthesis. Attempts to resynthesize and purify these compounds were carried out. However, more elaborate discussion into the structures and birefringence of these compounds were not undertaken but can be found in CH 6 of Dr. Thompson's dissertation.<sup>187</sup>

*Table A-C1. Birefringence of haloBBP Coordination Polymers*

CP	Birefringence
Eu(diCIBBP)(NO <sub>3</sub> ) <sub>2</sub> [Au(CN) <sub>2</sub> ](CH <sub>3</sub> CN)	~0.60
Eu(TCIBBP)(NO <sub>3</sub> ) <sub>2</sub> [Au(CN) <sub>2</sub> ](CH <sub>3</sub> CN)	~0.70
Pb(TCIBBP-H)[Au(CN) <sub>2</sub> ](CH <sub>3</sub> OH)	~0.90

#### Eu(diCIBBP)(NO<sub>3</sub>)<sub>2</sub>[Au(CN)<sub>2</sub>](CH<sub>3</sub>CN)

Eu(NO<sub>3</sub>)<sub>2</sub>·6H<sub>2</sub>O (90 mg, 0.2 mmol), diCIBBP (54 mg, 0.15 mmol), and KAu(CN)<sub>2</sub> (59 mg, 0.2 mmol) were loaded into a microwave reaction vial. 6 mL of MeCN was added to the vial before sealing under ambient conditions. The vial was subjected to heating to 125°C over 3 hours, twelve hours holding at this plateau temperature, and cooling over 60 hours to room temperature. The presence of unreacted

diCIBBP was visually noted and the aforementioned heating profile was repeated after sonication of the sealed sample for 2 hours. The resulting crystalline material was isolated with hot MeCN washes which selectively removed excess diCIBBP. MeCN was pumped off using a rotary evaporator and the sample was further dried through gentle heating on a hot plate. The crystalline material transitions from off-white coloration to yellow as it dries. Yield: 90 mg (63 %) off-white powder. *Anal.* Calc. for  $C_{23}H_{18}AuCl_2EuN_{10}O_8$  ( $Eu(diCIBBP)(NO_3)_2[Au(CN)_2](CH_3CN)(H_2O)_2$ ): C 28.12; H 1.85; N 14.26. Found: C 28.16; H 1.61; N 14.05%.

### **$Eu(TCIBBP)(NO_3)_2[Au(CN)_2](CH_3CN)$**

$Eu(NO_3)_2 \cdot 6H_2O$  (90 mg, 0.2 mmol), TCIBBP (68 mg, 0.15 mmol), and  $KAu(CN)_2$  (58 mg, 0.2 mmol) were loaded into a microwave reaction vial. 6 mL of MeCN was added to the vial before sealing under ambient conditions. The vial was subjected to heating to 125°C over 3 hours, twelve hours holding at this plateau temperature, and cooling over 60 hours to room temperature. The presence of unreacted TCIBBP was visually noted and the aforementioned heating profile was repeated after sonication of the sealed sample for 2 hours. The resulting crystalline material was isolated with hot MeCN washes which selectively removed excess TCIBBP. MeCN was pumped off using a rotary evaporator and the sample was further dried through gentle heating on a hot plate. Yield: 100 mg (66 %) yellow crystals. *Anal.* Calc. for  $C_{23}H_{16}AuCl_4EuN_{10}O_8$  ( $Eu(TCIBBP)(NO_3)_2[Au(CN)_2](CH_3CN)(H_2O)_2$ ): C 26.28; H 1.53; N 13.33. Found: C 25.97; H 1.20; N 13.61%.

These reactions and purification steps produced the europium haloBBP CPs in good yield and purity. Crystals were taken from the bulk sample and unit cell parameters matched those observed in the single-crystal structural determination.

### **$Pb(TCIBBP-H)(MeOH)[Au(CN)_2]$**

$Pb(ClO_4)_2$  (82 mg, 0.2 mmol), TCIBBP (68 mg, 0.15 mmol), and  $KAu(CN)_2$  (58 mg, 0.2 mmol) were loaded into a microwave reaction vial. 6 mL of MeOH was added to the vial before sealing under ambient conditions. The vial was subjected to

heating to 125°C over 3 hours, twelve hours holding at this plateau temperature, and cooling over 60 hours to room temperature. The resulting crystalline material was isolated and washed with hot MeOH. The solvent was pumped off using a rotary evaporator and the sample was further dried through gentle heating on a hot plate. Yield: 110 mg (78 %) yellow powder.

This product was identified as a perchlorate salt of the desired CP with the chlorinated-bbp fully protonated. A characteristic stretch of perchlorate at around 1075  $\text{cm}^{-1}$  on the IR was observed. *Anal.* Calc. for  $\text{C}_{22}\text{H}_{13}\text{AuCl}_5\text{N}_7\text{O}_5\text{Pb}$  ( $\text{Pb}(\text{TCIBBP})(\text{MeOH})[\text{Au}(\text{CN})_2](\text{ClO}_4)$ ): C 25.49; H 1.26; N 9.46. Found: C 25.54; H 1.36; N 9.10%.

This yellow powder was treated with excess triethylamine dissolved in MeOH in attempt to deprotonate the ligand. The resulting powder resulted in an elemental analysis comparable to the untreated. Attempts to modify the reaction conditions to get clean bulk product were undertaken. These included (1) using different lead salts, (2) attempting to deprotonate the ligand using bases such as triethylamine and sodium hydroxide followed by subsequent addition to a solution of stirring  $\text{Pb}^{2+}$  and dicyanoaurate, and (3) refluxing the reaction mixture. These led to the formation of different products most of which did not contain dicyanoaurate, as evidenced by a lack of a  $\nu_{\text{CN}}$  stretch in the IR or Raman. As such, they were not fully characterized. The bulk powders were isolated for the reactions that led to the incorporation of dicyanoaurate loaded into a Soxhlet extractor for purification. However, decomposition of the isolated products over prolonged periods was noted and evidenced by discoloration and loss of the  $\nu_{\text{CN}}$  stretches. Due to the great amount of difficulty encountered, this work was discontinued.

The haloBBP ligands used in this part of the thesis were synthesized using an adapted prep<sup>188–190</sup> from the literature involving the reaction of 2,6-pyridinedicarbonyl dichloride with the appropriately substituted nitroaniline with triethylamine in DCM reflux yielding the bisamide product. The nitro group on the bisamide was subsequently reduced *in situ* using iron powder, conc. HCl, and

ethanol:water 4:1 which leads to cyclisation forming the benzimidazole ring. The  $\text{Fe}^{3+}$  is then sequestered through reflux in EDTA yielding the haloBBP. An alternative nitro-amine reduction step involving iron powder in acetic acid which appears to proceed faster was also taken. However, this alternative pathway led to the formation of a large amount of ferric acetate which was difficult to separate from the ligand. Successful elemental analysis on haloBBP ligands were never achieved due to the difficulties in purification encountered. In the future, it would be worthwhile to affirm bulk purity of the haloBBP ligands prior to their use in the synthesis of CPs.

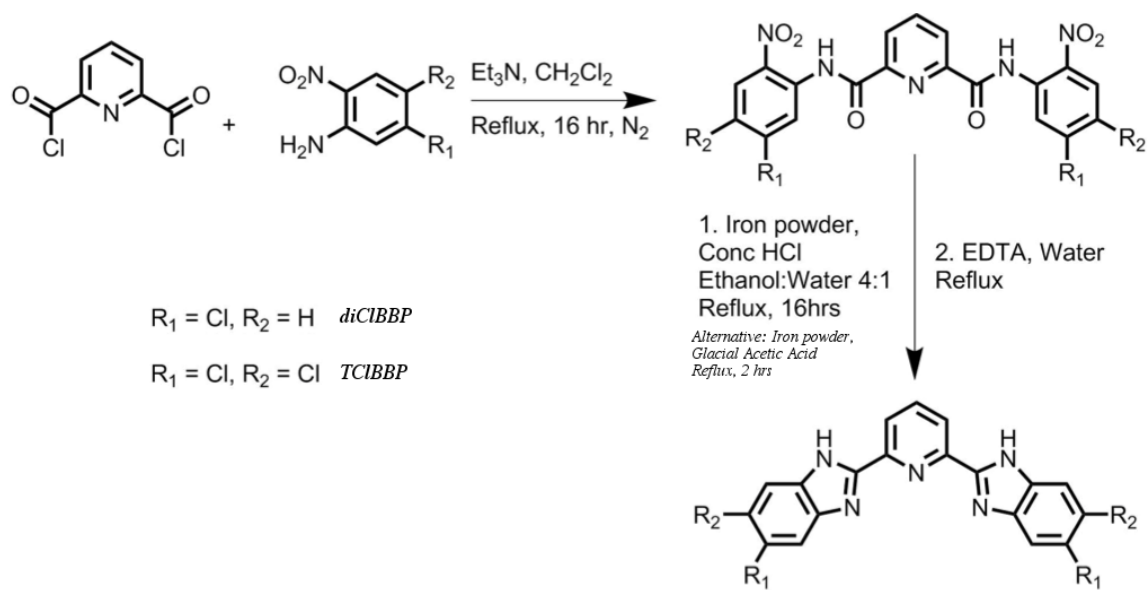


Figure A-C1. Synthesis of haloBBP ligands.